TÉCNICO LISBOA

Assessment of using atmospheric aerosol transport models for predicting the soiling rate in CSP plants

Paula Marie Möhring

Thesis to obtain the Master of Science Degree in

Energy Engineering and Management

Supervisors: Prof. Luís Filipe Moreira Mendes

Dr. Ing. Fabian Wolfertstetter

Examination Committee

Chairperson: Prof. Jorge de Saldanha Gonçalves Matos

Supervisor: Prof. Luís Filipe Moreira Mendes

Member of the Committee: João Carlos Carvalho de Sá Seixas

September 2019

Declaration of Academic Honesty

I declare that this document is an original work of my own authorship and that it fulfils all the requirements of the Code of Conduct and Good Practices of the *Universidade de Lisboa*.

Almería, 29.7.2019

Place, Date

Signature

Abstract

Particle deposition on solar mirrors deteriorates the performance of concentrating solar power (CSP) plants considerably. To save water used for cleaning activities and to increase the plant performance, the empirical soiling model was developed by the *German Aerospace Center* to calculate the daily decline in cleanliness (soiling rate) of CSP collectors based on meteorological and aerosol particle input parameters. Until now, the model can only be applied to site locations where measurements of the input parameters are available. In this work, a new approach is investigated to extend the soiling model application to various locations: Aerosol transport models simulate particle concentrations and many other parameters covering large areas, so they can provide the parameters that are needed as input for the soiling model. To implement this idea while following an integral stepwise process, the soiling model's sensitivity for input data in a different resolution of time and aerosol particle size bins is investigated by adapting ground measurement data. The meteorological and particulate matter parameters provided by two aerosol transport models are compared to the ground measurement data. Finally, the data is adapted to the soiling model format, its performance with the new input data is validated and the best available input data source and configuration is determined. The validation of the soiling model with photovoltaics (PV) soiling data shows that the soiling model is applicable to both technologies, CSP and PV.

Keywords

CSP Mirror Soiling, Soiling Rate Modelling, Aerosol Transport Models, PV Soiling

Resumo

A deposição de partículas em espelhos solares diminui consideravelmente a eficiência das centrais de energia solar com concentração (CSP). Com o intuito de poupar a água usada na limpeza dos espelhos e aumentar a eficiência das centrais, foi desenvolvido um modelo de sujidade para calcular a degradação diária do desempenho dos coletores (taxa de sujidade) pelo *German Aerospace Center*, baseado em parâmetros meteorológicos e de aerossóis de partículas. Até à data, o modelo só podia ser aplicado aos locais onde era efetuada a aquisição daqueles parâmetros. No presente trabalho foi investigada uma nova abordagem para estender a aplicação do modelo de sujidade a outras localizações a partir de modelos de transporte de aerossóis, providenciando os dados de entrada necessários à aplicação do modelo de sujidade. Para implementar esta ideia, investigou-se, a partir dos dados medidos no local, a sensibilidade do modelo de sujidade aos dados de entrada em diferentes resoluções temporais e diferentes dimensões das clases das dimensões das partículas. Num segundo momento os dados obtidos no local são comparados com os dados meteorológicas e dos aerossóis obtidos a partir de dois modelos de transporte. Por fim, os dados dos modelos são adaptados ao formato do modelo de sujidade e os resultados obtidos são validados, determinando-se o modelo de transporte e a configuração de dados mais adequados. A validação do modelo de sujidade com dados de sujidade de sistemas fotovoltaicos (PV) mostrou que o modelo é aplicável a ambos as tecnologias, CSP e PV.

Palavras-chave

Soiling de Espelhos Solares CSP, Previsão de Soiling, Modelos Transporte de Aerossóis, PV Soiling

Contents

List of Figures

List of Tables

Acronyms and symbols

a_{Brown}	soiling model parameter Brownian Motion contribution
AEROCOM	Aerosol Comparisons between Observations and Models
AERONET	Aerosol Robotic Network
a_{Im}	soiling model parameter impaction contribution
A_{mirr}	mirror surface
AOD	Aerosol optical depth
a_{turb}	soiling model parameter surface adhesion
Blacarb	black carbon
BSC	Barcelona Supercomputing Center
b_{turb}	soiling model parameter turbulent wind speed dependency
C	particle concentration
CAMS	Copernicus Atmosphere Monitoring Service
Ch	Channel
CIEMAT	Centro de Investigaciones Energéticas, Medioambientales y Tecnológicas
CNS	Centro Nacional de Supercomputación
CR	projected surface coverage
c_{Reb}	parameter transition between rebound – no rebound
CSP	Concentrated solar power
c_v	coefficient of variance
D_{ae}	aerodynamic diameter
$d_{eff,i}$	effective particle diameter of channel *i*
DLR	Deutsches Zentrum für Luft- und Raumfahrt – German Aerospace Center
DHI	Direct horizontal irradiance
D_{IM}	radius of curvature
DNI	Direct normal irradiance
DNI_{dir}	directly measured DNI
DNI_{refl}	reflected DNI
D_B	Brownian diffusion coefficient
d_{Im}	soiling model factor of proportionality
D_{op}	optical diameter
d_p	particle diameter
D_{ve}	volume equivalent diameter
ECMWF	European Centre for Medium-Range Weather Forecasts
EDM 164	optical particle counter (manufacturer: Grimm GmbH)
E_{Im}	deposition efficiency
EPA	Environmental Protection Agency
f_{Im}	parameter deposition efficiency function
F_{mirr}	particle flux to mirror
$f_{Rebound}$	rebound factor particle bounce-off

f_{turb}	soiling model parameter turbulent regime
GHI	Global horizontal irradiance
GIS	Geographic information system
GW	Gigawatt
h	hour
HTF	high-temperature fluid
hPa	hectopascal
i	channel number
IRI	International Research Institute for Climate and Society
$i_{SC,ref}$	short circuit current of reference PV module
$i_{SC,soiled}$	short current circuit of soiled PV module
ISE	Fraunhofer Institute for Solar Energy Systems
k	parameter for indication of k-fold cross validation round
k_B	Boltzman's constant
k_C	calibration factor cleanliness
LCOE	Levelized cost of electricity
m	mass
MAD	mean absolute deviation
MENA	Middle East – North Africa
MIS	Missour
mrad	milliradiant
MW	Megawatt
n	number of days
NASA	National Aeronautics and Space Administration
NCEP	National Centers for Environmental Prediction
NCPV	National Center for Photovoltaics
NMMB	Nonhydrostatic Multiscale Model on the B-grid
n_n	particle number concentration
NOAA	National Oceanic and Atmospheric Administration
n_V	particle volume concentration
$\overline{n_{v_i}}$	average particle volume concentration in channel *i*
OPC	optical particle counter
Org	organic
p	atmospheric pressure
PCC	Pearson correlation coefficient
PM	particulate matter
PlaSolA	Plataforma Solar de Almería
PSA	Plataforma Solar de Almería
PV	photovoltaic
rH	relative humidity
RMSE	Root-mean-square error

Sc	Schmidt number
St	Stokes number
STD	standard deviation
Sulph	sulphate
t	time
T_{air}	air temperature
T_{amb}	ambient temperature
TraCS	Tracking Cleanliness Sensor
u_{TraCS}	measurement uncertainty TraCS
u_{wind}	wind speed
v_B	deposition velocity due to Brownian motion
v_D	particle deposition velocity
$v_{D,turb}$	deposition velocity in turbulent condition
v_{Im}	deposition velocity due to impaction
$v_{P,i}$	single particle volume in channel *i*
v_S	deposition velocity due to sedimentation
$V_{totalP,i}$	total particle volume in channel *i*
w	weighting factor for the particle size bin extension
WMO	World Meteorological Organization
w_{rH}	soiling model parameter humidity influence on particle rebound
$\overline{x}$	average of *x*
α_{el}	mirror elevation angle
η	dynamic viscosity
θ_{az}	mirror azimuth
θ_{wind}	meteorological wind direction
ν	kinematic viscosity
ξ_{fit}	fitted mirror cleanliness
ξ_{PV}	cleanliness PV module
ξ_{raw}	directly measured raw mirror cleanliness
ξ_{Reb}	soiling model parameter rebound
ξ_{turb}	soiling model parameter turbulent regime
$\hat{\xi}$	soiling rate
$\hat{\xi}_{model}$	modelled soiling rate
$\hat{\xi}_{obs}$	observed soiling rate (TraCS measurement)
ρ	density
σ_{or}	parameter mirror orientation towards wind direction

If we suppress all discussion, all criticism, proclaiming
'This is the answer, my friends; man is saved!'
We will doom humanity for a long time to the chains of authority,
confined to the limits of our present imagination.

Richard Feynman, January 1988

1 Introduction

In this chapter the reader is introduced to the relevance and the motivation behind the chosen topic in section 1.1, followed by a clear outline of the objectives that are pursued in this master thesis in section 1.2. The methodology and the structure of the master thesis are demonstrated in section 1.3.

1.1 Motivation

Water-scarcity affects 1-2 billion people today. Under the climate change scenario, nearly half of the world's population in 2030 will be living in areas of high water stress, it will displace up to between 24 million and 700 million people in arid and semi-arid areas [1]. Simultaneously, the demand for electricity and also the utilization of renewable energy sources is increasing - already around one-fourth of the global electricity is generated by renewable energy sources such as hydro, solar, wind, geothermal, tidal power and by energy from biofuels and waste [2]. The share of renewable technologies in the newly installed electricity generating capacity is increasing each year, with an upward trend expected for the near future. Solar energy plays an important role in this development: the cumulative installed photovoltaics (PV) capacity is 300 GW; concentrating solar power (CSP) installed capacity is 4.8 GW worldwide. CSP capacity is expected to double by 2022 and reach 10 GW with almost all new plants incorporating thermal energy storage [3]. Deserts and arid or semi-arid regions provide the highest levels of direct normal irradiance. Therefore CSP plants are commonly installed in remote desert areas, where high aerosol particle concentrations are found and water resources are scarce. Large amounts of water are required by these plants to clean the firm soiling layer sticking to the collectors (Figure 1.1) which often cannot be removed by air pressure alone. The 100 MW *Shams 1* parabolic trough plant in Abu Dhabi, for example, consumes almost 190 000 m³ of water per year for cleaning purposes [4].

Figure 1.1. 'Dust' on a parabolic trough collector at Plataforma Solar de Almería, February 2016 (source: DLR)

In the design process of CSP power plants it is common to approximate the soiling losses with a constant factor, but soiling is a highly time-dependent process and errors in profit calculated with constant soiling and cleaning parameters can be as high as 9.4 % [5]. In the operation of a CSP plant, a trade-off between the revenue received from generating electricity and costs of cleaning operations (water, labour, investments for cleaning vehicles) must be found. Condition-based cleaning strategies that take into consideration changes in mirror reflectivity, electricity prices and solar irradiance can yield significant savings [6]. When modelling the daily evolution of the cleanliness of the collectors in the solar field and applying the best cleaning strategy considering soiling rate prediction, solar irradiance, cleaning costs, and electricity prices, the profit can be increased by 2.6 % [5].

The soiling model developed at the German Aerospace Center Institute of Solar Research (DLR) models the decline in cleanliness of CSP mirrors – the soiling rate – based on meteorological variables and design parameters as input data. Important input parameters are for example the atmospheric particle number concentration, wind characteristics and the tilt angle of the mirror. The soiling model was developed and its performance was validated at two stations with meteorological, particle concentration and soiling rate measurements, Plataforma Solar de Almería (PlaSolA/PSA) in Spain and Missour in Morocco (see locations in the map in Figure 1.2) [7].

Figure 1.2. Map with marked locations of the two investigated stations PlaSolA in Spain and Missour in Morocco (source: Google Maps)

In this master thesis, the soiling model's potential to be applied to large areas is investigated. To be used at different locations, soiling model input data has to be available at the desired sites. Numerical aerosol transport models can provide such data as they simulate and forecast particle concentrations and meteorological parameters for comprehensive areas. Once the use of transport model data as input for the soiling model is proven valid, it is possible to predict soiling losses for large areas, to create soiling maps and to forecast soiling rates. In the design and application process of CSP plants

a more reliable estimation of the soiling rate is available and during operation better cleaning decisions are reached, reducing the plant's cleaning water consumption up to 50 % [4].

1.2 Objectives

The first goal of this master thesis project is to analyse the sensitivity of the soiling model concerning its input parameter resolution. The intercomparison of the measured ground data with the data obtained by aerosol transport models to investigate the quality of the new input data for the soiling model is a further objective.

Another goal is to create and test a new method to adapt the transport model data compatibility to the soiling model and to improve the model integration.

The extension of the soiling model application to various locations by validating the use of aerosol transport model data in the soiling model is the final goal of this thesis (graphically shown in Figure 1.3). In addition to the spatial and temporal extended application of the soiling model, its ability to model soiling rates for photovoltaic technology is validated, which is especially interesting considering the large installed PV capacity.

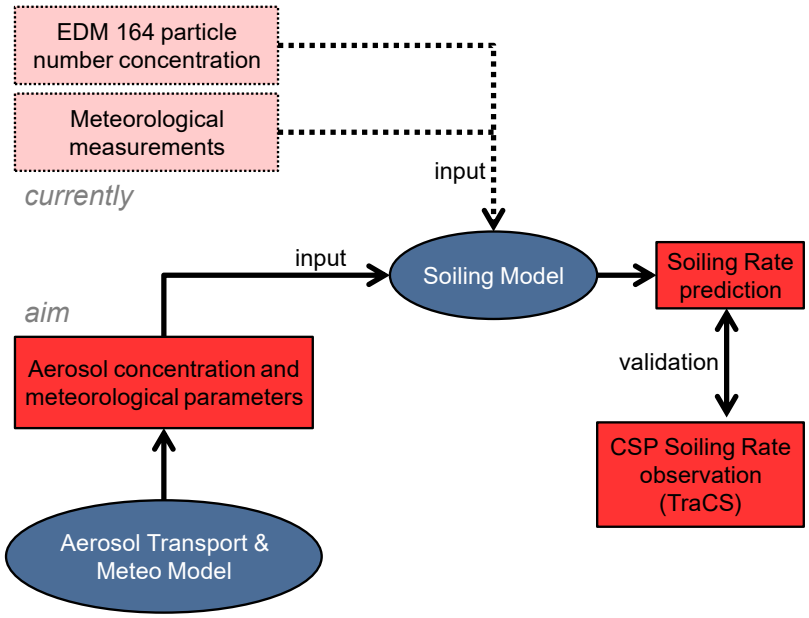

Figure 1.3. Schematic presentation of substituting input parameters for the soiling model

1.3 Methodology and structure

After the explanation of the urgency and motivation behind the chosen topic in the introduction, a summary of the most important background knowledge is provided in chapter 2. The interdisciplinary topic requires covering basic theories from the areas meteorology, particle physics, measurement principles, numerical transport models and the description of the soiling model which is implemented in Matlab. An overview of alternative and complementing research approaches with the objective to

model soiling losses and to create soiling maps is presented in section 2.6, to define the master thesis work in the scope of the state of the art.
In this project, a stepwise approach is pursued to integrate the meteorological and aerosol particle data of the transport models to the soiling model. Firstly, the sensitivity of the soiling model is tested, regarding varying input parameter resolutions because the aerosol transport model data resolutions are different from the ground measurement input data which is used until now. How does the soiling model operate once the input parameters are given as hourly or daily averages instead of data for each minute? Is the soiling model able to predict the soiling rate even when the particle number concentration is given in 3 instead of 30 size bins? This analysis in chapter 3 serves as a benchmark and helps to determine how well the model operates with temporally and spatially less detailed data.

The extension of the provided number of particle size bins by the transport models based on particle measurements of two years at PlaSolA as a novel adaptation method is presented in section 4.1.
As the next step, in section 4.2 the aerosol transport model data is compared to the observed data at the two measurement stations PlaSolA and Missour. The correlation of the numerically simulated parameters with ground observation data shows the quality of the input data and represents a second important benchmark.
Two different aerosol transport model data sets, one developed by the Barcelona Supercomputing Center (BSC), the other developed by the European Centre for Medium-Range Weather Forecasts (ECMWF), are used as input data for the soiling model. The provided data is formatted according to the soiling model requirements and then used to parametrize and to validate the model. The obtained results are compared to the soiling model performance with original measurement data and presented in section 4.3.
The extended application of the soiling model to soiling of PV modules is tested and discussed in chapter 5.
Conclusions from each of the implemented steps are presented in chapter 6, where the most important insights obtained from this work are summarized. Additionally, an outlook is provided, indicating the next steps and projecting possible future work.

2 Scientific background and state of the art

This chapter summarizes the scientific knowledge used as a basis for the following thesis work. A brief introduction into the technologies and the optics of CSP and PV and how soiling affects them, a description of aerosol particles and their transport and deposition processes are provided. The principles of atmospheric transport models are described. Particle deposition on solar mirrors and the measurement instrumentation for its detection and quantification are presented. A full understanding of the existing DLR soiling model design is essential to investigate its extended application and its adaptation to aerosol transport model input data. Finally, the state of the art in modelling soiling rates of CSP and PV technologies is presented in section 2.6.

2.1 CSP and PV optics under soiling influence

The sun is an important source of renewable energy and its rays can be directly used in solar thermal or photovoltaic systems. Solar thermal means that solar energy is used to generate thermal energy which can be utilized as process heat and for power generation. To reach high temperatures and keep efficiency high, the solar irradiance is concentrated. Concentrated solar power (CSP) uses a collector to focus light on a smaller receiver, heating a heat transfer fluid (HTF) to high temperatures of up to 550°C (line-focusing with molten salt) or more than 1000°C (point-focusing). Electricity is generated when the HTF drives a heat engine, usually by generating steam and driving a steam turbine. Collectors that focus sunlight on an absorber tube are classified as linear focus collector types; the most common among them are parabolic troughs or Fresnel collectors. Point focus concentrators are for example parabolic dishes and arrays of heliostats focusing irradiation on a central absorber in a solar tower. The thermal output energy of the collector depends on its optical efficiency which can be decreased by particles on the collector mirror surface, as in Figure 2.1 where strong dust deposition on a parabolic trough collector is shown [8].

Figure 2.1. Red dust event leading to strong soiling of a parabolic trough collector at PlaSolA, 2016 (source: DLR)

CSP uses only the direct component of solar irradiance within a small acceptance angle. The direct normal irradiance (DNI) is the amount of solar radiation received per unit area by a surface that is perpendicular to the direction of the sun beam originating at an opening angle of 2.5° around the center of the sun. The global horizontal irradiance (GHI) includes direct (DNI) and diffuse horizontal irradiance (DHI). The latter is mainly composed by light that has been scattered by molecules and particles in the atmosphere. The GHI is of particular interest to PV installations since the PV technology utilizes direct and diffuse irradiance contributions. [9]

Figure 2.2 shows the simplified sun ray path in a parabolic trough as a common CSP collector example. The rays enter the system from the sun which is a spherical source, appearing as a disc with a half angle of about 4.7 mrad seen from the earth's surface. Size and geometry of the trough and the absorber tube define the maximum acceptance angle which for the *EuroTrough* as a common example of a parabolic trough collector is around 12.5 mrad [10]. Thus the sunlight which is reflected with its half angle of arrival (4.7 mrad) normally lies within the absorber acceptance angle and reaches the tube [10].

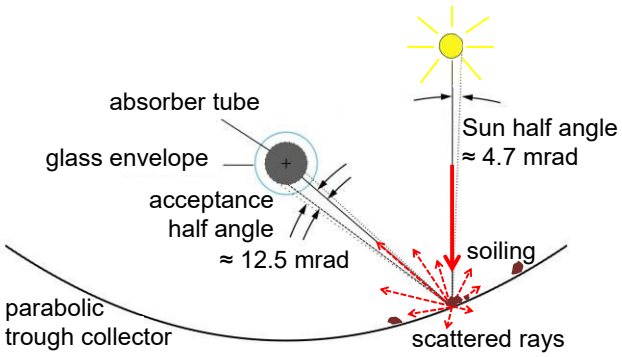

Figure 2.2. Simplified optical ray path in a parabolic trough concentrator with a practical acceptance angle of 12.5 mrad and a half angle of the sun of 4.7 mrad [10]

As mirror imperfections and soiling increase, the amount of diffusion or scattering of the reflected light increases as well, represented by red dashed arrows in Figure 2.2. If the scattering angle is greater than the absorber maximum acceptance angle, the reflected sunlight is lost and cannot be utilized for energy conversion in the tube [10].

PV cells convert sunlight directly by using the photovoltaic effect. In PV modules, the ray path is simpler as compared to its path in a CSP system. The light transmits through a glass layer, passes the interfaces between air, glass, lamination layer and solar cell and is then directly used there in the photovoltaic effect. Unlike in CSP technology, PV modules can utilize direct and diffuse components of solar irradiance and the sunlight does not need to be concentrated to reach high temperatures. The angle of acceptance of the incoming light is around 90° for PV cells, which exceeds the sun angle of CSP collectors by far [11]. Depending on the relation between soiling particle size and wavelength of incoming light, the interaction between light and particle and the scattering regime is defined. For aerosol particles which are deposited on solar mirror surfaces – typically in the size range of 0.1 µm to 20 µm – and for incoming sunlight with a wavelength of around 550 nm, most of the incoming light is forward scattered. Forward scattering, also called *Mie* scattering, is the predominant scattering regime

for sun rays influenced by mirror soiling, while diffuse scattering in all directions (*Rayleigh* scattering) occurs as the particles and molecules decrease in size [11]. To a great extent, the mostly forward scattered sun rays can still be utilized and converted into electricity by the solar PV cell, while in CSP applications the forward scattered light is mostly lost. As a result, soiling reduces the energy output of a PV system less than that of a CSP system. This is reflected in the soiling measured for both technologies: for CSP the soiling is approximately 8 to 14 times higher than the soiling of PV for the same soiling conditions [12].

2.2 Aerosol particles

The term *aerosol particle* refers to a suspension of liquid or solid small, discrete objects in a gaseous medium [13]. Atmospheric aerosol particles are quite heterogeneous in various aspects. Their size and mass ranges are wide, with diameters spanning over five orders of magnitude from just a few nanometres to around 100 µm. Aerosol particles also differ in origin and constituents: Some are generated by anthropogenic influence which are mostly ultrafine (< 0.1 µm in diameter) black carbon particles, a distinct type of carbonaceous material formed from the incomplete combustion of fossil and biomass-based fuels [14]. Inorganic aerosol particles are for example mineral species – mostly desert dust – and sea salt, organic aerosol particles can be pollens and plant fragments. The variety of chemical compositions results in different physical, optical and geometrical properties of aerosol particles [15].

To describe the aerosol particle concentration in the atmosphere while accounting for particle size, the size range is divided into discrete intervals and for each of these intervals the particle number, the particle surface, the particle volume or mass per volume of air is described. With the use of discrete size bins for describing aerosol particle size distribution, information about the distribution within each bin is lost.

The compositions of aerosol types depend on regional and temporal aspects. Urban regions' aerosol particles are characterized by a high influence of anthropogenic sources. In marine ambient sea salt species are predominant; there are rural continental types with mainly natural origin and moderate anthropogenic influence, remote continental, polar and desert aerosol particles. Aerosol particles with diameters from 0.01 to 0.25 µm are found in the mid and upper troposphere above cloud level. Seasonal behaviour of aerosol particles is due to organic cycles of living organisms, agriculture and due to additional fuel burning for heating in winter. Variations over shorter timescales (hours) are also significant because changes in wind direction and speed and rainfall have an impact on aerosol transport. Due to the long-range transport of aerosol particles and due to their lifetime of roughly one week, the particles do not remain in the regions of origin but tend to be carried to other regions. Thus averages for the concentrations of major aerosol types can be given as well as the average atmospheric aerosol particle size distribution which is found to be a log-normal distribution (Figure 2.3) [15].

Atmospheric particles are generally non-spherical with unknown mass densities. To better describe and compare particles of different shapes, several equivalent diameters are defined: the volume, the aerodynamic and the optical equivalent diameters are most important. The volume equivalent or geometric diameter D_{ve} is the diameter of a sphere having the same volume as the irregularly-shaped particle. For a spherical particle, the volume equivalent diameter is equal to the physical diameter D_p.

The aerodynamic diameter D_{ae} is defined as the diameter of a spherical particle with density ρ_0 = 1000 kg/m^3 that has the same aerodynamic resistance as the aerosol particle. This diameter is commonly used in setting air pollution standards because it determines where in the human body the aerosol is deposited upon inhalation [15]. The particle's optical scattering abilities define the optical diameter D_{op}, which is measured using optical measurement devices (see 2.4.1) [15, 16].

In this work, unless otherwise noted, references to particle size refer to the geometric diameter, as the optical particle counter (OPC) used in the following converts the impulse into volume equivalent diameter. The aerosol transport models assume spherical particles and in this work, all aerosol particles are considered to be spherical particles.

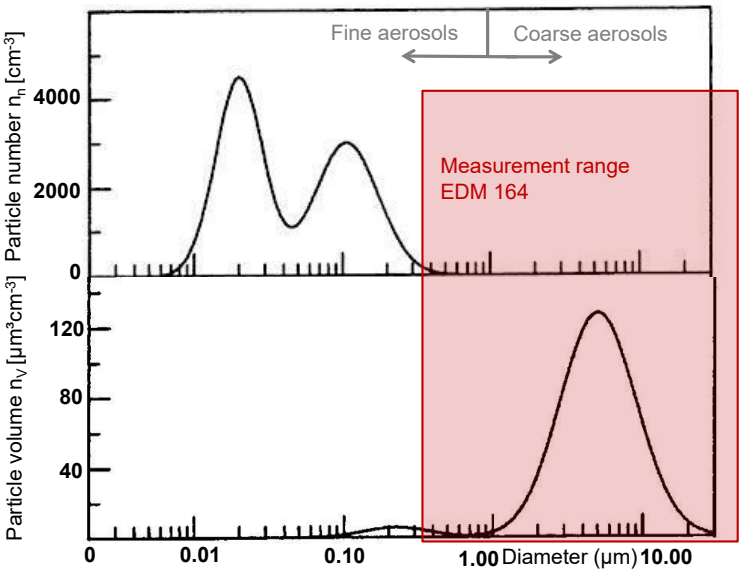

Figure 2.3. Typical aerosol particle number distribution and volume distribution expressed as function of logarithmic particle diameter D_P. The areas below the two curves correspond to the total aerosol particle number and volume respectively [15]

2.3 Particle transport and deposition mechanisms

Once emitted from their source into the atmosphere, all aerosol species are transported over short- or long-range distances before they deposit again onto ocean and land (Figure 2.4).

Mineral dust particles represent one of the most important aerosol species in mass and in extinction of the sunlight [16]. The dust fraction in the tropospheric aerosol particle load is more than 50 % and about 35 % of the primarily emitted aerosol mass consists of mineral dust, half of which originates from the Saharan desert and another third from other large desert areas [14]. Jet streams of air

transport dust over thousands of kilometres, for example from the North-western coast of Africa across the Atlantic to Northern America and from the deserts of Asia across the Pacific Ocean [15]. The Bodélé Depression area in Southwestern Chad is the main dust source of the Sahara in winter and supplies essential minerals to the Amazon rain forest through long-range transport [18].

Conditions favouring mineral dust emission are strong winds, dry soil and sparse vegetation leading to erosion and soil resuspension [16]. The wind is also a major factor enhancing the emission of sea salt aerosol particles, which results from the interaction of wind stress with the ocean surface and the breaking of air bubbles induced by wave breaking [14].

The dynamic behaviour of aerosol particles influencing the aerosol transport and deposition is characterized by different external forces acting on the particle.

The *drag force* is exerted by the fluid on the moving particle as soon as there is a difference between the velocity of the particle and that of the fluid. It depends on the particle velocity and size, on the fluid density and Reynold's number [15].

The second external force on the particle is *gravity*, resulting in gravitational settling of the aerosol particle. For small particle sizes, the settling velocity is extremely slow, submicrometer particles settle with only a few centimetres per hour [15].

Since the density of the fluid (air) is much lower than the particle density (density of dust particles: 2650 kg/m^3 [19]), *buoyancy forces* can be neglected [15]. Situations in which charged particles move in an electric field are important in gas-cleaning or aerosol measurement devices, but for the short- and long range transport of aerosol particles *electrical forces* can be neglected too [15].

The *Brownian Motion* is another force, acting on the particle due to random bombardments by microscopic gas particles, resulting in random acceleration and displacement of the particles. This force can also be described as macroscopic aerosol particle diffusion process characterized by a Brownian diffusivity D_B depending on the temperature, the fluid viscosity and the particle size (Stokes-Einstein relation). The smaller the particle, the further Brownian diffusion forces outweigh gravity. Nevertheless, due to the diffusion coefficients of gas (order of magnitude ~ 0.1 cm^2/s) particles diffuse very slowly and for atmospheric aerosol transport the Brownian diffusion is not an efficient transport mechanism in the scales of atmospheric transport models [15].

In the atmosphere, the air in which the aerosol particles are suspended is often in motion. For many applications, it is simply assumed that gravity is the only external force on the particle. The assumption that gravitational force and particle inertia can be neglected leads to the picture that the particles follow the streamlines of the airflow which is acceptable for most atmospheric aerosol transport models [15].

After being carried by air streams and travelling short or long distances, aerosol particles are removed from the atmosphere by wet and dry deposition (Figure 2.4). Dry deposition is the transport of particulate species from the atmosphere onto surfaces in the absence of precipitation. Factors governing particle dry deposition are the level of atmospheric turbulence (especially in the layer nearest to the ground), the chemical properties of the depositing species and the characteristics of the surface itself. Wet deposition refers to natural processes by which aerosol particles are washed out of the atmosphere and consequently are delivered to the earth's surface by cloud or fog drops, rain or snow. The relative importance of dry deposition as compared to wet deposition for the removal of a

particle depends on the solubility of the species in water, on meteorological conditions such as the amount of precipitation and wind speed as well as the type of climate, terrain and surface cover [15].

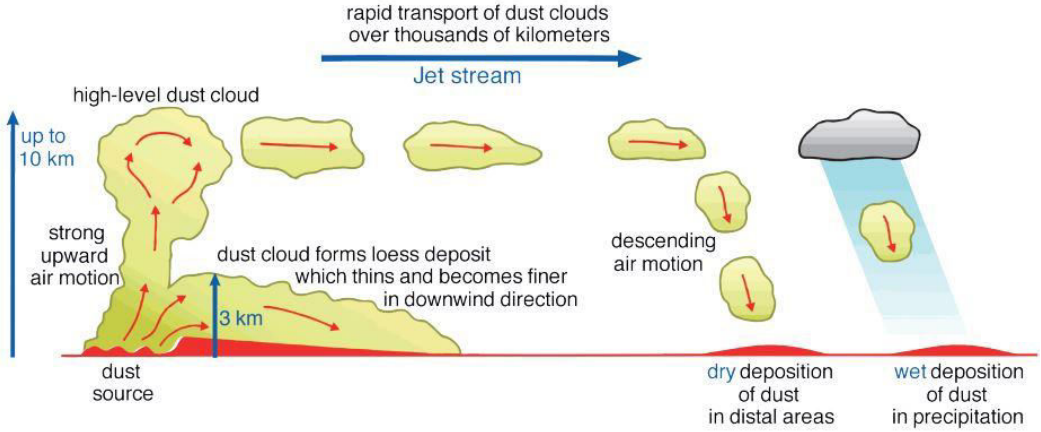

Figure 2.4. Schematic diagram showing different dust-transport mechanisms in the high- and low-level atmosphere [20]

2.4 Particle deposition on solar mirrors

In aerosol or dust transport models the atmospheric particle concentration is obtained by mass conservation equations. In these equations, the particle deposition is represented and calculated by appropriate sink terms. Atmospheric dust transport models consider wet and dry deposition and determine the average particle mass deposited in an area with a spatial resolution of several kilometres.

The development of the soiling model for CSP technology is based on existing model equations for dry deposition of dust over geographic regions. The equations have been adjusted on the specific problem of dust deposition on a CSP mirror surface and designed according to the available meteorological measurements. In this section, the measurement instruments are described (subsection 2.4.1); followed by a presentation of the physical model structure and the model equations (subsection 2.4.2).

2.4.1 Measurement instrumentation

For the development, training and testing of the soiling model two measurement sites are used, one in Missour, Morocco (32°51'37,116''N 4°6'26,1''W) and the other one at CIEMAT's Plataforma Solar de Almería (PlaSolA), Spain (37°5'42,55''N 2°21'17,02''W) (map in Figure 1.2). The station in Missour is operated by DLR in collaboration with IRESEN and is equipped with an optical particle counter and a Tracking Cleanliness Sensor (TraCS), likewise the station at PlaSolA. Both sites are arid according to common climate classification schemes [21].

Soiling measurement CSP The TraCS system is a stationary instrument which measures the cleanliness of mirror samples. From the measured cleanliness, a soiling rate is calculated in daily time resolution. The measurement principle is based on the comparison between two pyrheliometer

signals. It is equipped with one pyrheliometer measuring the direct normal irradiance (DNI) and with a second pyrheliometer oriented towards the mirror samples which are mounted on a support arm of the solar tracker (see Figure 2.5). At night they are parked in a vertical position, similar to the operation of a parabolic trough or a heliostat [10].

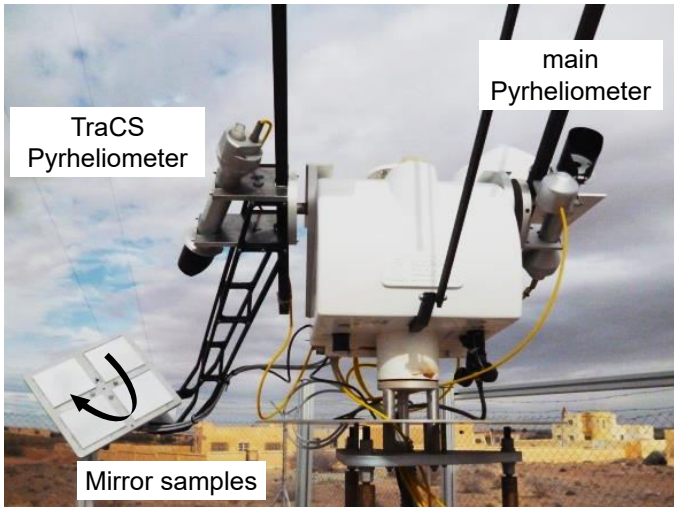

Figure 2.5. TraCS system installed in Missour, Morocco (Source: DLR)

The mirror plate rotates to obtain an increased measurement area on the mirrors and to enable the device to measure multiple mirrors in parallel.

The ratio of the two pyrheliometer irradiance measurements gives the cleanliness ξ_{raw} according to

$$\xi_{raw}(t) = \frac{DNI_{refl}(t)}{k_c \cdot DNI_{dir}(t)} \quad (1)$$

DNI refers to the pyrheliometer measurement signals; the index *refl* refers to the reflected irradiance and *dir* to the irradiance coming directly from the sun. The calibration factor k_c is introduced such that the cleanliness of a clean mirror becomes 1. Calibration and assigning a new value for k_c is performed each time the mirror samples are cleaned. The TraCS acceptance angle is 13.5 mrad and its reflection angle is 15°.

During exposure, the mirror samples soil continuously and their reflectance reduces (except for mirror cleaning and rain events), as demonstrated exemplarily in the time series for $\xi_{raw}(t)$ in Figure 2.6. Due to the rotation of the mirror, inhomogeneous soiling patterns and cyclical fluctuations during the course of the day, the measured raw cleanliness shows a variation. This is why in the data post-processing a curve $\xi_{fit}(t)$ is fitted manually to the cleanliness measurement curve, from which the soiling rate $\hat{\xi}$ as the loss of reflection per time interval is calculated as the derivative (according to 2) and displayed in daily time resolution [21].

$$\hat{\xi} = \frac{d\xi_{fit}}{dt} \quad (2)$$

The measurements are taken at a height of around 1.5 m above ground and located at open terrain with no objects to block the air streams from hitting the mirror's surfaces.

The uncertainty of measurement for the TraCS instrument u_{TraCS} results from various technical and operational aspects: the calibration, the mechanical handling of the device, the field of view of the pyrheliometers, the spectral reflectivity of the mirror and the weighted pyrheliometer measurement

uncertainty itself are considered. The combined standard uncertainty corresponding to the unit of cleanliness measurements (where 1 is the cleanest possible condition and 0 is the least clean condition) is u_{TraCS} = 0.018, thus the TraCS measurement accuracy is sufficient considering the possible range of cleanliness to be expected in operational power plants [10]. Considering the mean cleanliness of about 0.75 over the measurement period of two years (01/2017-03/2019) the resulting measurement accuracy is 2.4 %. In terms of soiling rate units, the TraCS measurement accuracy is 0.2 %/day [10].

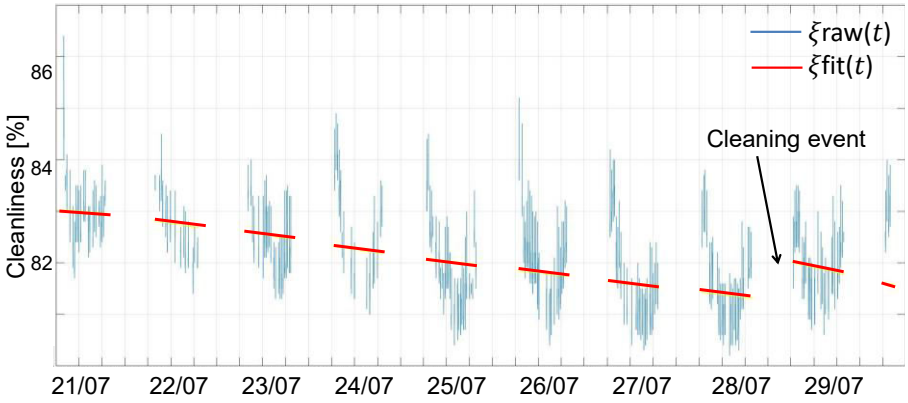

Figure 2.6. Curve of cleanliness measurement with TraCS and fitted cleanliness curve 2018 (PlaSolA)

Soiling measurement PV The cleanliness of the photovoltaic module is measured at PlaSolA by a set-up next to the TraCS device with two fixed solar cells with smooth glass surfaces. One of the two PV cells is cleaned daily while the other is left uncleaned. The short circuit current $i_{SC}(t)$ of a solar cell, which is the current through the cell when the voltage across the cell is zero, is a direct measure for the amount of light that is converted into electricity within the cell. The principle is to measure the short circuit current of the solar cell with a soiled cover $i_{SC,soiled}(t)$ and the short circuit current of the clean reference solar cell $i_{SC,ref}(t)$, their ratio results in the cleanliness $\xi_{PV}(t)$ of the soiled transparent cover according to

$$\xi_{PV}(t) = \frac{i_{SC,soiled}(t)}{i_{SC,ref}(t)} \quad (3)$$

Similarly to the TraCS, the PV cleanliness is then transformed into a daily soiling rate (equation 2) [12].

Particle concentration The measurement of the particle number concentration is implemented with the EDM 164 aerosol particle counter (EDM 164) of the manufacturer Grimm GmbH, an optical particle counter which measures the particle concentrations for particles with diameters between 0.25 µm and 32 µm (see measurement range Figure 2.3) in 31 size channels. The measurement output is the particle number per size channel and litre of air averaged over a one-minute time interval. A continuous air stream flows through a measurement chamber which is illuminated by a laser beam. The amplitude of the scattered light by each particle is proportional to the particle size, the number of pulses is equivalent to the number of particles. This signal of the optical diameter is then converted into an equivalent geometric diameter D_{ve} = D_p [22].

Measurement errors or uncertainty can result from sampling and transport losses of the device hardware such as the sampling tube, from the detector response, its sensitivity and from data

processing with the data logger [13]. According to the manufacturer, the measurement uncertainty of the EDM 164 is stated to be 5 % for all size channels [23]. Additional uncertainty results from the non-detectable size range of aerosol particles with the given measurement technique; the minimum detectable particle diameter of EDM 164 is 0.25 µm but aerosol particles can be as small as 0.001 µm.

Meteorological parameters The wind speed u_{wind} is measured by a Thies anemometer at 5 m, 7.5 m and 10 m above ground. For this work, the wind speed at 10 m height is used. The threshold velocity of the wind sensor is 0.3 m/s and its measurement accuracy is 1 %. The wind vane is provided by the same manufacturer and gives the meteorological wind direction θ_{wind} in degrees clockwise from North to the direction from which the wind is blowing with an accuracy of ± 3.6° [24].
The Campbell Scientific CS215 sensor for ambient temperature T_{amb} (in °C) and relative humidity *rH* (in %) has an uncertainty of 2 % [25]. The atmospheric pressure *p* is measured with a sensor from the same manufacturer in hPa with an accuracy of 0.5 % (at room temperature) [10].

2.4.2 Conceptual design of the soiling model

Based on atmospheric dust transport models, the soiling model equations are developed and adapted to the application of solar mirror soiling [7].
The particle flux towards the mirror surface $F_{mirr}\ (d_P)$ is calculated as the product of the particle concentration $C\ (d_P)$ and the deposition velocity $v_D\ (d_P)$, according to

$$F_{mirr}(d_P) = v_D(d_P) \cdot C(d_P). \tag{4}$$

C has the unit m^{-3} and can be taken directly from the EDM164 measurements. v_D has the unit m/s and is the parameter which is determined by model equations for physical processes. It represents the average velocity with which particles move out of the air volume towards on the mirror surface. The deposition velocity is highly dependent on the particle diameter and is influenced by various parameters such as wind, gravity, surface type and orientation, and particle properties [21].
In atmospheric dust transport models covering large areas, both wet and dry deposition mechanisms are important since in humid regions a great share of the particles is washed out of the atmosphere by wet deposition. CSP technology is usually implemented in arid regions where dry deposition is more important as compared to wet deposition. The soiling model is therefore solely developed for dry deposition. Still, extreme wet deposition events also occur in arid regions: red rain events, which are light rainfalls that coincide with a high atmospheric aerosol particle concentration, are detected around 3 to 6 times per year at PlaSolA and contribute significantly to CSP collector soiling [21]. These events are added to the model separately so that the associated soiling rate value is mapped to the special soiling event.
The particle deposition velocity (equation 5) is the sum of the deposition velocities of different deposition mechanisms resulting from the following processes: sedimentation (v_S), Brownian motion (v_B) and impaction (v_{Im}).

$$v_D = v_S + v_B + v_{Im} \tag{5}$$

Interception, the process of particles being swept out of the air stream by microscopic structures on the surfaces of plants or leaves (small, hairy fibres) does not apply to the case of smooth mirror surfaces and is neglected in the soiling model. The aerodynamic resistance, which is considered in atmospheric dust transport models, can be neglected too because the particle concentration is already being measured at the point of interest, close to the mirror surface.

Sedimentation or gravitational settling is the particle deposition on the mirror due to gravity. It is derived from the equilibrium of friction, buoyant and gravitational forces and valid for the laminar flow regime. For the soiling of solar mirrors, the orientation of the mirror surface has to be taken into consideration because they are typically not horizontally mounted and move throughout the day to track the sun. The inclined reflector surface is taken into account by including the elevation angle α_{el} of the mirror. The deposition velocity due to sedimentation v_S is calculated according to

$$v_S = \cos(\alpha_{el}) \cdot \frac{g \cdot {d_P}^2 \cdot (\rho_{aero} - \rho_{air})}{18 \cdot \eta_{air}}, \tag{6}$$

with the gravitational acceleration g, the aerosol particle diameter d_P, the particle density ρ_{aero} = 2650 kg/m² (according to [19]), the density and the dynamic viscosity of the air ρ_{air} and η_{air}. Properties of the air are assumed constant and taken for standard conditions because of their small variation for the temperature and pressure range of the considered application [21].

The Brownian motion is the diffusion process of aerosol particles which are put into motion by random impacts from surrounding air molecules and particles (see section 2.3). Unlike for atmospheric transport models, it has to be included for the mirror soiling process hence the extremely short distance particle transport from the mirror surrounding air onto the mirror surface. Brownian motion becomes more relevant for smaller particles and for higher wind speeds and temperatures (see equation 7). The deposition velocity due to Brownian motion v_B is calculated as

$$\begin{aligned} v_B = a_{Brown} \cdot u_{wind} \cdot Sc^{-0.667} &= a_{Brown} \cdot u_{wind} \cdot \left(\frac{\nu_{air}}{D_B}\right)^{-0.667} \\ &= a_{Brown} \cdot u_{wind} \cdot \left(\frac{\nu_{air} \cdot 3 \cdot \pi \cdot \eta_{air} \cdot d_P}{k_B \cdot T_{air}}\right)^{-0.667} \end{aligned} \tag{7}$$

$$Sc = \frac{\nu_{air}}{D_B} \tag{8}$$

$$D_B = \frac{\nu_{air} \cdot 3 \cdot \pi \cdot \eta_{air} \cdot d_P}{k_B \cdot T_{air}}. \tag{9}$$

It depends on the parameter a_{Brown} which quantifies the relative contribution of the Brownian motion to the total deposition velocity in comparison to the other deposition mechanisms (as weighting factor it is determined during the model parametrization process) and on the wind speed u_{wind}. The Schmidt number Sc is the ratio of motion caused by diffusion processes and motion caused by impaction and depends on the kinematic viscosity of the air ν_{air} and the Brownian diffusion coefficient D_B (equation 8). The diffusion coefficient D_B is described by the Stokes-Einstein relation (9) using the air viscosities, the particle diameter, the Boltzman's constant k_B and the air temperature T_{air}.

In outdoor atmospheric conditions not only random diffusion processes and gravitational settling move the aerosol particles but also the air streams characterized by wind speed and direction carry particles along. Deposition on the mirror due to impaction happens when an airflow hits the obstacle, the

streamlines deviate from their original path and some particles don't follow the curvature of the airstream but hit the obstacle's surface due to their momentum (see Figure 2.7).

The Stokes number *St* is a dimensionless parameter which characterizes the behaviour of particles in an air stream and is defined as the ratio between the time it takes for a particle to adapt to changes in an airflow by friction with the medium's molecules and the time it takes for the medium itself to change its flow speed and direction (Stokes number for laminar flow profiles: see equation 11).

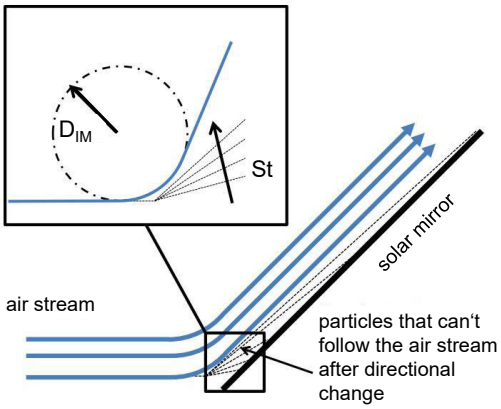

Figure 2.7. Mechanism of particle impaction on a mirror surface [9]

With the Stokes number, the deposition efficiency E_{Im} (in equation 11) is determined. The radius of curvature D_{IM} determines the curvature of the airflow.

The impaction related deposition velocity v_{Im} can be written as

$$v_{Im} = a_{Im} \cdot \sigma_{or} \cdot u_{wind} \cdot E_{Im} \cdot f_{Rebound} = a_{Im} \cdot \frac{\sigma_{or} \cdot u_{wind}}{1 + \exp(-f_{Im} \cdot (St - 1))} \cdot f_{Rebound} \tag{10}$$

$$St = \frac{\rho_{aero}}{18 \cdot \eta_{air}} \cdot {d_P}^2 \cdot \frac{u_{wind}}{D_{Im}} \tag{11}$$

$$D_{Im} = \frac{d_{Im}}{\sigma_{or}} \tag{12}$$

The weighting factor a_{Im}, the parameter f_{Im} and the proportionality factor d_{Im} are determined during later model parametrization with measurement data, similar to the previously mentioned factor in equation 6. The parameter σ_{or} accounts for the mirror orientation towards the wind direction and is calculated with θ_{wind}, the mirror azimuth θ_{az} and the elevation angle α_{el}. By this means only the component of the wind which points perpendicularly towards the optical mirror surface, not the wind flows in parallel or towards the back of the mirror, are taken into account. With larger particle sizes and with higher wind speeds the impaction deposition velocity increases.

The probability of particles bouncing off the mirror's surface is expressed by the parameter $f_{Rebound}$ (equation 13). Rebound happens if the kinetic energy of the particle is greater than the adhesion force between the particle and the mirror surface. The corresponding energy inequation leads to the formula

$$f_{Rebound} = 1 - \frac{1}{1 + \exp\left(-c_{Reb} \cdot \left(d_P - \left(\frac{\xi_{Reb}}{u_{wind}} + w_{rH} \cdot rH^2\right)\right)\right)}, \tag{13}$$

where c_{Reb}, ξ_{Reb} and w_{rH} are factors depending on the mirror surface, on the particle's properties and on the influence of relative humidity *rH*. They are determined in the parametrization.

In general, higher relative humidity and smaller particle sizes lead to reduced particle rebound, while larger particles at small relative humidity increasingly tend to bounce off the surface.
In Figure 2.8 the deposition velocity is plotted against the particle diameter for different wind speeds with T_{amb} = 20°C, θ_{wind} = 0°, α_{el} = 45°, θ_{az} = 0° and rH = 60 %. At wind speeds equal to zero, only sedimentation occurs. With increasing wind speed the processes of impaction, rebound and Brownian motion gain influence on the particle deposition velocity. While Brownian motion affects smaller particles more and increases their deposition velocity for higher wind speeds, medium, and coarse particles are affected more by impaction and rebound. The higher the wind speed, the greater is the influence of impaction and rebound becomes even for small particle sizes.

The deposition velocity according to equation 5 is valid only for laminar flow profiles. In the turbulent flow regime, sedimentation and Brownian motion are negligible; just impaction induced particle deposition is considered. The turbulent deposition velocity $v_{D,turb}$ according to equation 14 is valid for wind velocities above a critical threshold velocity which is determined during model parametrization, as are the model parameters a_{turb}, b_{turb}, f_{turb} and ξ_{turb}. Thus the turbulent deposition velocity is dependent on the model variables u_{wind} and d_P. The wind direction is not included since in turbulent conditions, it is not well defined anymore.

$$v_{D,turb} = a_{turb} \cdot (1 + u_{wind} \cdot b_{turb}) \cdot f_{Rebound,turb} \tag{14}$$

$$f_{Rebound,turb} = 1 - \frac{1}{1 + \exp\left(-f_{turb} \cdot \left(d_P - \frac{\xi_{turb}}{u_{wind}}\right)\right)} \tag{15}$$

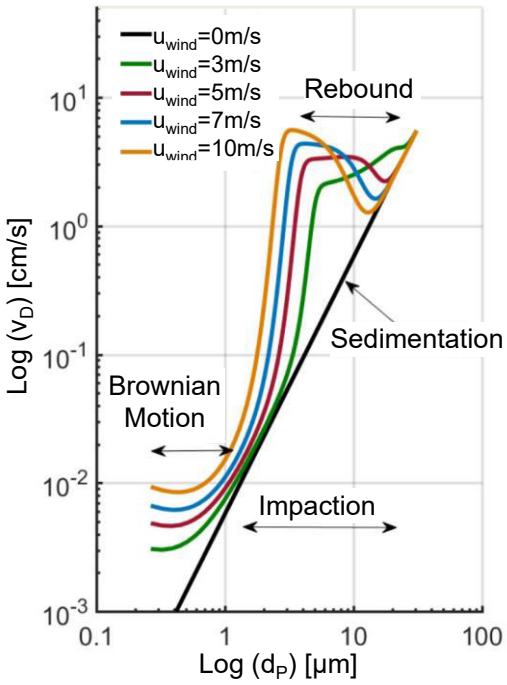

Figure 2.8. Deposition velocity (laminar) against particle diameter for different wind speeds [21]

For the application to soiling in CSP, the essential parameter is rather the optical loss caused by the particles adhered to the mirror than the number of the attached particles.

Particle number and size distribution result in the projected surface coverage CR according to

$$CR = A_{mirr} \cdot \sum_{d_P=0.25\mu m}^{32\mu m} F_{mirr}(d_P) \cdot {d_P}^2 \cdot \frac{\pi}{4} = A_{mirr} \cdot v_D(d_P) \cdot C(d_P) \cdot {d_P}^2 \cdot \frac{\pi}{4}. \quad (16)$$

With the variable CR the fraction of the mirror surface A_{mirr} covered by particles per time interval can be described. The remaining uncovered mirror fraction is proportional to the cleanliness. Therefore it is assumed that the CR is proportional to the soiling rate with a negative slope of the connecting linear equation. The coefficients to describe the relation between CR and modelled soiling rate (slope and the intercept) are determined with a linear regression calculation analysis during the optimization of the soiling model. An example of the linear fit with a negative slope is presented in Figure 2.9 [21].

The model parametrization and its validation are implemented with k-fold cross-validation. The complete PlaSolA data set of meteorological parameters, aerosol particle number concentration, and measured soiling rate is divided chronologically into five parts. Four fifths of the data set is used as a train set to fit the calculated model output to the measured soiling rate and to determine the model parameters (model parametrization). The remaining fifth part of the data set is used as a test set to quantify the goodness of the model (validation). This process is repeated five times in total so that each part of the data set is the test set once, to use the full capacity of the recorded measurements. The data set recorded in Missour is used as validation set too and the soiling model is validated for the fitted parameters from the PlaSolA train data set. For the goodness of the fit, the root-mean-square error (RMSE) of the PSA test set and the Missour set are used. Due to the five-fold validation process, five parameter sets and five RMSEs are obtained (k = 1…5), so for the discussion, the average RMSE and the variation of the RMSEs are presented. Besides, the mean absolute deviation (MAD) and the bias are used to assess the model quality.

The soiling model parametrization and validation for PV soiling is operated according to the same methods as the TraCS based soiling model operation. As the PV cleanliness measurements are available only at PlaSolA, it is trained and tested based on the soiling rate values with five-fold cross-validation and validation results are presented for the PSA test set in chapter 5.

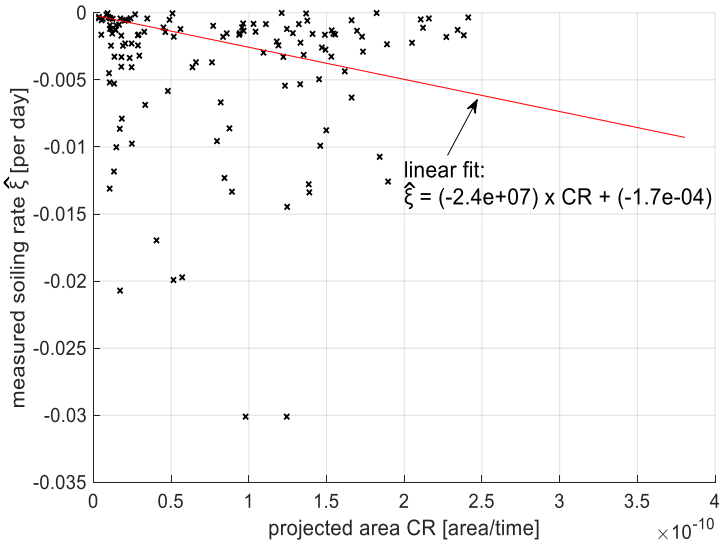

Figure 2.9. Linear fit as qualitative relation between measured soiling rate and projected area, shown for PlaSolA (2017-2019), Test Set, k = 1

2.5 Atmospheric aerosol transport models

Aerosol particles in the atmosphere have a large impact on pollution and climate as they affect clouds, radiation, and atmospheric chemistry. In addition to aerosol particle measurements at locations all over the globe, many numerical models are developed to simulate their spatial and temporal distributions for more comprehensive areas and to forecast aerosol particle concentrations. Despite many common aspects of atmospheric aerosol models as providing information about aerosol particle concentrations (mass, volumetric or number concentrations) and considering the aerosol life cycle with its sources, sinks, transport mechanisms (see section 2.3) and microphysical processes, the detailed characteristics of each model can be very different. Atmospheric aerosol models are available for diverse spatial scales, for several aerosol types and size distributions and for different time scales. Simulations of comprehensive global atmospheric aerosol models often require the use of supercomputing facilities depending on their spatial resolution, especially if they account for special emission factors, for anthropogenic perturbations and effects on clouds, radiation, and climate [26].

In this section, two aerosol models are described, firstly the NMMB model in subsection 2.5.1 and secondly the CAMS model in subsection 2.5.2. As the model output from these models is used in this work, the specifications of the simulations which generate the new input for the soiling model are described here.

2.5.1 NMMB model specifications

The NMMB Monarch model is a multi-scale atmospheric dust model with an online interface (see Figure 2.10, [27]) designed and developed at Barcelona Supercomputing Center (BSC-CNS) in collaboration with the National Oceanic and Atmospheric Administration (NOAA), the National Centers for Environmental Prediction (NCEP), the NASA Goddard Institute for Space Studies and the International Research Institute for Climate and Society (IRI). The model which only accounts for dust aerosol particles is embedded into the Non-hydrostatic Multiscale Model (NMMB) by NCEP. The NMMB Monarch model provides short to medium-range dust forecasts for both global and regional domains, currently over North Africa - Middle East - Europe. It is referred to as the NMMB model in the further proceeding of this work [28].

The transport model's mass balance equation for dust accounts for processes as dust generation and uplift by surface wind and turbulence, different soil textures and soil wetness effects on dust production, horizontal and vertical advection, horizontal diffusion and vertical transport by turbulence and convection. Dust removal processes considered by the model are dry deposition, gravitational settling and wet deposition [28, 29].

The model configurations for the regional North Africa - Middle East - Europe version are a spatial resolution of 0.3° x 0.3° which for the chosen locations equals a grid of approximately 30 km x 30 km. To obtain weather parameters for the exact locations at PlaSolA and in Missour bilinear spatial interpolation is applied.

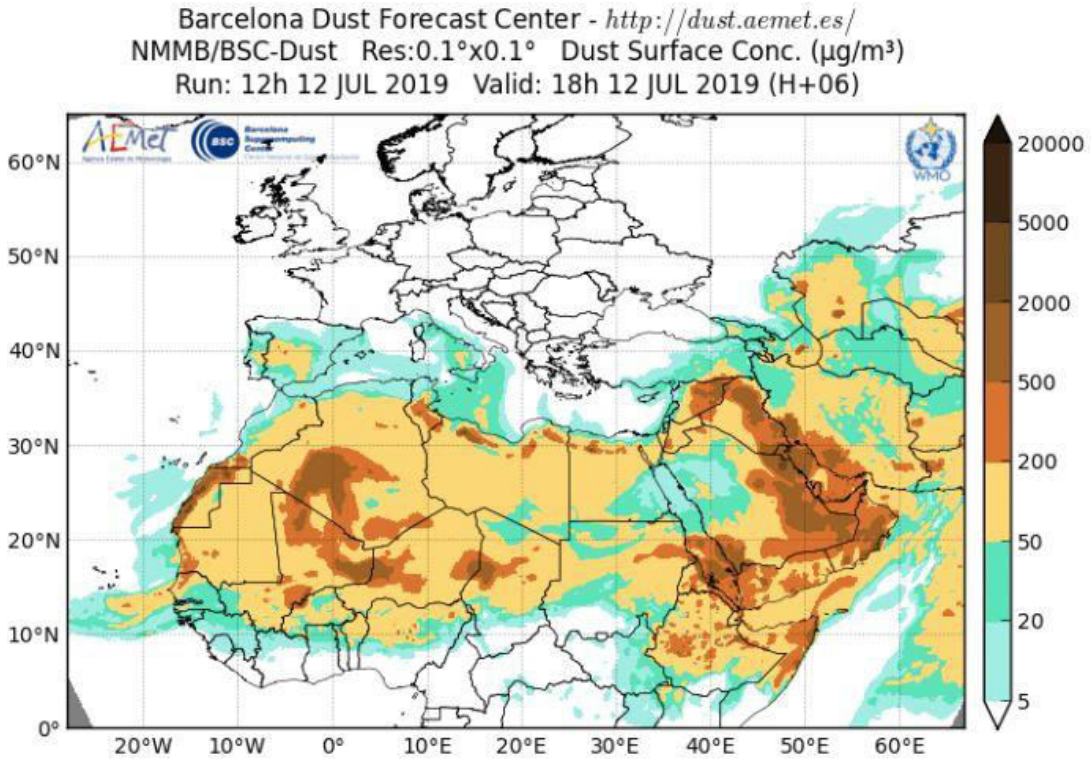

Figure 2.10. NMMB model online interface - dust surface concentration forecast (source: BSC [27])

The temporal resolution of the model is characterized by a forecast time from 0 to 72 hours with data provided every three hours and meteorological fields are initialized every 24 hours. The model output parameters used in this work are instantaneous values of the past two years (2017-2019) given every three hours with an internal calculation time of 15 minutes [29].

The dust particle mass concentration provided by NMMB is in particulate matter (PM) metrics, which are defined by the Environmental Protection Agency (EPA). $PM_{2.5}$, for example, indicates a concentration of particles with diameters of around 2.5 µm and smaller. The limit is not sharp, but weighting curves are applied (see Appendix A.6) [30]. The NMMB model provides particle mass concentrations in three size bins, starting from particle diameters of 0.2 µm up to $PM_{2.5}$, PM_{10}, and PM_{20}. A more recent version of the model features eight particle size bins from 0.2 µm to 20 µm (particle size bins see Table 3.1). Data of this version has not yet been available for the evaluation presented in this work due to ongoing validation processes, but it will be soon and thus this configuration is also included in this work too to allow a prognosis. Other parameters that are calculated by the model and used in this work are dust dry deposition and dust wet deposition, temperature, wind speed in x- and y-direction (at 10 m), absolute humidity and atmospheric pressure.

The NMMB model performance can be evaluated with sun-photometric measurements and satellite retrievals or with routine observations for dust monitoring. The scarcity of available measurements can be a problem for the evaluation of a model with an extremely large spatial coverage [31]. The model performance evaluated with the available measurements lays in the upper range of the AEROCOM model evaluation scores [29]. The NMMB/BSC-Dust latest annual evaluation scores of the year 2018

for the Dust Optical Depth show correlations of 47 % (Sahel/Sahara), 35 % (Middle East) and 38 % (Mediterranean). The evaluation is implemented for the aerosol optical depth (AOD) which describes the attenuation of incoming solar radiation through the atmosphere by particles [32]. The AOD evaluation at the station PlaSolA shows correlations of by the NMMB model predicted and with a sun-photometer measured AOD of 74 % in 2017 and 34 % in 2018. The closest measurement station to Missour used for the model evaluation is located in Ouarzazate (around 350 km towards south-west from Missour) and shows correlations of 39 % (2017) and 55 % (2018) [32, 33].

2.5.2 CAMS model specifications

The second aerosol model which is used in this work is the model developed within the system of the Copernicus Atmosphere Monitoring Service (CAMS), implemented by the European Center for Medium-Range Weather Forecasts (ECMWF) on behalf of the European Union [32]. It is based on a model developed at the French Laboratoire d'Optique Atmospherique and Laboratoire de Meteorologie Dynamique with modifications implemented by ECMWF. In this work, it is referred to as the CAMS model [34].

The CAMS model mass balance equation includes sources for sea salt and desert dust and considers sedimentation, wet and dry deposition. Aerosol particle transport is implemented with diffusion and convection, chemical transport is also considered [35].

Contrary to the NMMB model which only includes dust aerosol particle species, five species are included in the CAMS model: sea salt, desert dust, organic matter, black carbon and sulphate aerosol particles (see Table 2.1).

Table 2.1. Aerosol particle species with their corresponding size bins in the CAMS Model [36]

aerosol species	**diameter range [µm]**
sea salt	0.06 - 1.0
sea salt	1.0 - 10.0
sea salt	10.0 - 40.0
dust	0.06 - 1.1
dust	1.1 - 1.8
dust	1.8 - 40.0
hydrophilic organic matter	–
hydrophobic organic matter	–
hydrophilic black carbon	–
hydrophobic black carbon	–
sulphate	–

Salt and dust aerosol particles are represented in three bins with each different bin limits while for the other aerosol particles no size limits are specified. Organic Matter and black carbon are divided into a hydrophilic and a hydrophobic fraction [36].

The data used in this work is obtained from the CAMS reanalysis with a spatial resolution of 80 km x 80 km. The temporal resolution of the data is for three hours. Parameters which are provided

for the 11 aerosol particle bins (Table 2.1) are the mass mixing ratios (particle mass concentration per weight of air) and dry and wet deposition fluxes. Temperature, dew point temperature, atmospheric pressure, wind speed, and wind direction are other parameters provided by the CAMS Reanalysis.

2.6 Alternative research approaches

Several research approaches focus on estimating soiling losses for both concentrated solar power and photovoltaics are pursued since the interest is high given the negative impact that soiling has on the performance on solar energy systems. Most of the approaches focus on PV soiling and more PV soiling measurement stations are available due to the large industry interest [37, 38]. The cost of electricity production with PV is very competitive with Levelized costs of electricity (LCOE) of around 4 €-cent/kWh as compared to the electricity cost of CSP, which currently has an LCOE around 10 €-cent/kWh, both for utility-scale plants and for the same annual solar irradiance (March 2018). [39]

Many studies investigate the relation between soiling losses and environmental and meteorological parameters like weather profile (rain pattern, humidity, and temperature), pollution and land surface characteristics. Based on observations at 20 installed PV soiling stations in the USA, a study by the National Renewable Energy Laboratory finds that metrics of PM and precipitation patterns correlate with observed soiling metrics [40].
Another study with a similar approach determines PV soiling losses with satellite solar irradiation and AOD data combined with outdoor measurements of temperature, wind speed, humidity, and precipitation. The study shows that AOD, wind speed, and rainfall have a direct influence on soiling losses [41]. The mentioned studies find a correlation between historical parameters and soiling losses, without applying an empirical deposition model and often quantify the losses in categories of low, medium or high soiling. The classification is implemented annually, so it might help to determine whether a site is generally suited for the erection of a solar power plant. Providing detailed information and soiling loss forecasts based on the historical weather and pollution data to derive maintenance recommendations for operators is rather difficult using this approach.

An interactive soiling map for some regions in the United States is implemented by the National Center for Photovoltaics (NCPV) and shows data from 83 sites, classifying these locations according to the severity of soiling [42]. To estimate losses at sites without soiling measurements, based on data from close available soiling stations, different spatial interpolation techniques are tested. For locations located within 50 km of soiling measurement stations, the correlation is as high as 74 % [37]. Nevertheless, errors with spatial interpolation can occur for locations with different features like those of the investigated sites. Soiling is a process which is highly dependent on local factors like nearby particle sources as industry or roads with heavy traffic which affect the particle concentration and soiling at exposed sites. These local characteristics are rarely captured by spatial interpolation.

An approach for global soiling data exchange is the ‘World PV Soiling Map’ as a platform for the global PV community to understand soiling loss rates in different geographical locations. The soiling map

developed in a dissertation at the Indian Institute of Technology compiles the soiling research data obtained by various organizations and companies on a world map. Even if the data in this specific map is not completely consistent because the analysed studies calculate soiling with different approaches, the general concept of combining the already achieved measurement results and insights on a comprehensive map is an innovative approach which uses already available resources [43]. Recently, the global soiling map was updated with 52 additional sites [38].

A study by the Fraunhofer Institute for Solar Energy Systems ISE models the soiling of glazing materials in arid regions with geographic information systems (GIS) [44]. GISs are application tools to capture, analyse and present spatial or geographic data in maps. The use of a GIS is suitable in this case because of its ability to integrate environmental data of different spatial and temporal resolution and various sources. Thus, measured data by ground stations and remote sensing in combination with simulation results can be used to determine soiling losses. A soiling potential model is developed covering mineral dust generation, emission, transport and deposition on ground and surfaces. Due to the statistical approach with long-time mean data and the low spatial resolution of the utilized input data, the model's accuracy is reduced. As a result of the study, a preliminary dust risk map of the Middle East – North Africa (MENA) region based on parameters as land cover, vegetation, elevation, soil type, precipitation, wind speed and direction, and humidity is obtained, shown in Figure 2.11.

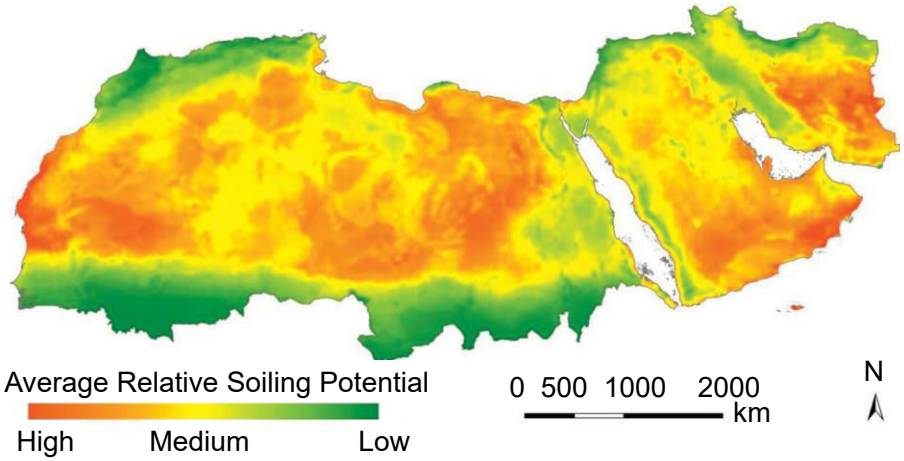

Figure 2.11. Dust risk map created with a GIS and with a soiling potential model, representing PV relative soiling potential in the MENA region (source: Fraunhofer ISE [44])

The difference between desert and non-desert areas is revealed, as well as a variation within the deserts. For the southwest Sahara, the region west of the Nile, the south of the Arabian Peninsula and parts of Iran a high soiling potential is displayed, while regions east of the Nile and the high altitude areas of Iran and on the western Arabian Peninsula show lower soiling potentials. The map is based on preliminary results which could still change with ongoing research, but in future, it can be used for the identification of the most favourable locations or the selection of materials in solar energy systems [44].

3 Soiling model sensitivity analysis

The meteorological parameters calculated by dust transport models usually are less precise than on-site measurements [31]. Meteorological models and dust transport models calculate many different parameters for various locations covering large areas (see section 2.5). Usually, the time resolution of these models is different from the minutely time resolution of the measurements which were used for the conceptual design of the soiling model and its parametrization and validation at DLR. Additionally, the models used in this work do not divide the particle concentration into 30 size channels but instead use three or eight channels to describe the aerosol or dust particle concentration. When data generated from a meteorological dust model is used in the soiling model, not only the inaccuracy of the dust model data itself due to spatial interpolation or other factors impacts the results. Also, the ability of the soiling model to digest the input data of lower temporal and spatial resolution may affect the final results. To estimate how the soiling model operates with input data that is averaged every few hours or every day and with data that summarizes various particle size channels into only a few bins, this section analyses the soiling model quality in dependence of the input parameter resolution.
In this chapter the analysed data set and the data processing is described in 3.1. On-site measurement data is averaged to downscale the temporal resolution in section 3.2. Then, it is used as input data in the adapted soiling model and the change of model quality in comparison to before is discussed in section 3.3. The analysis of the influence of time and particle size channel resolution is implemented separately to discuss the final results of using model data as soiling model input based on the results of chapter 3. The here discussed results are considered as a benchmark for using model data as input in the soiling model (section 4.3). Furthermore, the sensitivity analysis helps to assess whether a specific aerosol transport model with a certain resolution is eligible for using its data in the soiling model even before tests with actual data, which is not always immediately available.

3.1 Post-processing of raw on-site measurement data

The data sets used to analyse the soiling model robustness are meteorological and aerosol particle on-site measurements at PlaSolA and in Missour which were recorded from 2017 to 2019. Due to non-availability of some devices at both locations or due to problems with data loggers, not all parameter measurements for the entire time were recorded continuously.
The TraCS at PlaSolA (PSA) recorded cleanliness measurements rather sporadically in 2017, information is available only for May 2017 and for some days in June, July and November 2017. From the start of May 2018 to the end of March 2019 PSA TraCS data is available, with data gaps of one week in August 2018, one week in September 2018 and two weeks in February 2019. In total, the soiling rate for 290 days is recorded at PSA in the selected period of two years.
Meteorological data at PSA from 1.1.2017 to 1.3.2019 has several short data gaps from 10.4.2017 to 17.4.2017, from 22.9.2017 to 2.10.2017 and from 1.11.2017 to 11.11.2017. In the period from April to May 2018, the data availability is irregular with around 45 days missing. In total, data gaps add up to around 72 of 789 days without recorded data (9 %). The particle measurements (EDM 164) have

missing data from 2.9.2017 to 1.12.2017 and during the first week of May 2018, resulting in 96 of 789 unrecorded days (12 %).
The TraCS in Missour during the years 2017 and 2018 was online from 02.02.2017 to 18.03.2018 (12.5 months) with periods of unavailability from 16.07.2017 to 15.09.2017, from 20.09.2017 to 20.10.2017 and for 5 days in November 2017, resulting in a total data gap of three months. Since March 2018 the sun tracker doesn't work, so the TraCS device in Missour is offline since then. Meteorological measurement data ranges from 5.1.2017 to 19.9.2018 and holds data gaps from 22.2.2017 to 6.3.2017, from 7.10.2017 to 22.10.2017, from 26.3.2018 to 3.4.2018 and from 18.4.2018 to 27.4.2018, so in total data from 45 days of 622 measurement days is not available (7 %). Particle measurements data gaps are from 23.8.2017 to 17.9.2017 and from 13.10.2017 to 22.10.2017. Since 17.11.2017 the EDM 164 is not installed in Missour. In total, this results in 283 days with recorded particle count measurements.
The analysis of input data is carried out for each parameter independently (see section 3.2) since the focus is on the comparison of the adapted resolution data to the normal data, while the soiling model robustness is analysed only for days when data availability for all devices (meteorological, aerosol particles and TraCS recorded cleanliness) coincide (see section 3.3).
The post-processing of raw measurement data also includes checking for outliers. These might result from the inaccurate calibration of the devices or problems with the data logger. Values which do not make sense physically such as air pressure lower than 850 hPa or higher than 1050 hPa and other detected outliers are removed from the data set. Days with natural cleaning (strong rainfalls) are removed too since the soiling model does not describe these cleaning events.

3.2 Input data adaptation

Recorded DLR measurement data sets are transformed into data sets with a lower resolution in two aspects: the particle size channel information is condensed (subsection 3.2.1) and the time resolution is reduced (subsection 3.2.2). The artificially generated new data sets are analysed regarding their changes as compared to the original data sets, for example in variation, in average values and the distribution of occurrences.

3.2.1 Particle size channels

Dust transportation and forecast models divide the aerosol particles into several transport size bins, for different models ranging for example from two to nine size bins with particle diameters from 0.02 µm to 60 µm [31]. The obtained data of the two dust models NMMB and CAMS divides the aerosol particles into three size bins, each model defining the boundaries of the lower and upper bin limits differently (see section 2.5). The future version of the NMMB Model will feature eight particle size bins. The data of this version is not yet available at the time of this work due to the ongoing validation process but it can be expected that in future particle concentration data with eight particle size bins will be available.

In this subsection, the measured particle number concentrations at the DLR sites are adapted to simulate aerosol transport model output data of lower resolution. The 31 available particle size channels are reduced to three size channels according to the boundaries as defined in the NMMB Model and with the definitions by ECMWF for the CAMS Model. Besides, a reduction to eight size channels is implemented to estimate the soiling model quality with this layout. The boundaries of each aerosol particle size bin for the different transport models, the effective diameters (according to [45]) and the corresponding channels for the EDM 164 measured aerosol particle concentration at PSA and in Missour are presented in Table 3.1.

Table 3.1. EDM 164 particle size channels and associated NMMB and CAMS Model aerosol particle bins

		Model			EDM 164	
		Bin	diameter [µm]	effective diameter [µm]	Channel	diameter [µm]
NMMB	future available model output bins	1	0.2 - 0.36	0.3	1 - 4	0.25 - 0.375
		2	0.36 - 0.6	0.5	5 - 8	0.375 - 0.615
		3	0.6 - 1.2	0.9	9 - 12	0.615 - 1.15
		4	1.2 - 2.0	1.56	13 - 15	1.15 - 2.25
		5	2.0 - 3.6	2.6	16 - 18	2.25 - 3.75
		6	3.6 - 6.0	4.4	19 - 20	3.75 - 5.75
		7	6.0 - 12.0	7.4	21 - 24	5.75 - 11.75
		8	12.0 - 20.0	15.2	25 - 28	11.75 - 22.5
	current available model output bins	1	0.2 - 2.5	1.35	1 - 16	0.25 - 2.75
		2	2.5 - 10.0	6.25	17 - 24	2.75 - 11.75
		3	10.0 - 20.0	15	25 - 28	11.75 - 22.5
CAMS		1	0.06 - 1.1	0.58	1 - 12	0.25 - 1.15
		2	1.1 - 1.8	1.45	13 - 14	1.15 - 1.8
		3	1.8 - 40	21	15 - 30	1.8 - 31.0

In Figure 3.1 the combination of four channels of the EDM 164 at PSA (9, 10, 11, 12) to the third of the eight NMMB size bins (line 3 in Table 3.1) is presented as stacked bar plot, the upper boundary of channel 12 indicates the particle number concentration of the third NMMB bin in particles per litre air in 1-minute resolution. The particle mass concentration n_m in µg per litre is shown as a black curve on the second y-axis. In Figure 3.2 the first 12 EDM 164 channels with measurements in Missour are combined into the first of three CAMS Model bins (line 1 of the CAMS part in Table 3.1). When high particle concentrations occur, often they do for several particle size bins. It is noticeable that peaks in particle concentration are less extreme for every single one of the 12 size channels compared to when all particle channels are summed up. The variation for the summed particle size channels seems to be larger than the particle number variation of a single channel.

The standard deviation (STD) is the statistical evaluation parameter which captures the amount of variation of a data set according to equation 17:

$$STD = \sqrt{\frac{1}{n-1} \cdot \sum_{i=1}^{n} (x_i - \bar{x})^2} \tag{17}$$

The relative standard deviation is expressed by the dimensionless coefficient of variation c_v: the ratio of STD and the mean (see equation 18). It is consulted because it helps to interpret the STD in the context of the mean of the data which varies considerably for the single-channel particle number concentrations and the summed concentrations.

$$c_v = \frac{STD}{\overline{x}} \tag{18}$$

The average STD for particles measured in EDM 164 channels 9-12 is 210.3, while the variation of the sum of these particle channels (NMMB bin 3 of 8) is characterized by an STD almost four times higher (STD = 809.6). The relative variation for the NMMB bin 3 (of 8) is expressed by a variation coefficient c_v = 109.2 % which is lower than the average c_v for the single-particle channels 9 to 12 which is c_v = 113.3 %. Missour data in the CAMS Model configuration with three size bins exhibits a similar behaviour: while the STD for the first of three bins is STD = 28057, the average STD for particles measured in EDM 164 channels 1-12 is STD = 2755. This shows that variation of the sum over particle size channels can be more than ten times higher than for the single channels. The relative variation for CAMS bin 1 is c_v = 101.4 %, the average c_v for the single-particle channels 1 to 12 is c_v = 123.9 %. These values imply that the absolute variation (STD) is increasing for the summing up particle number concentrations, while the relative variation (c_v) is decreasing.

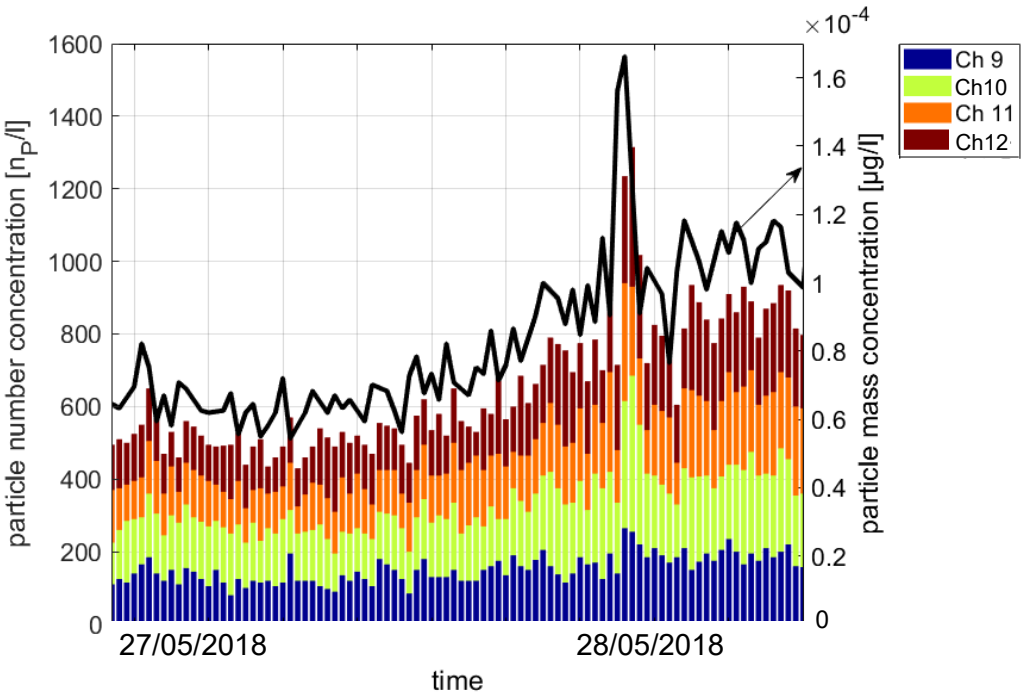

Figure 3.1. Stacked particle number concentrations of EDM 164 channels 9-12 into NMMB bin 3/8 (left axis) and particle mass concentration of NMMB bin 3/8 (right axis), PSA

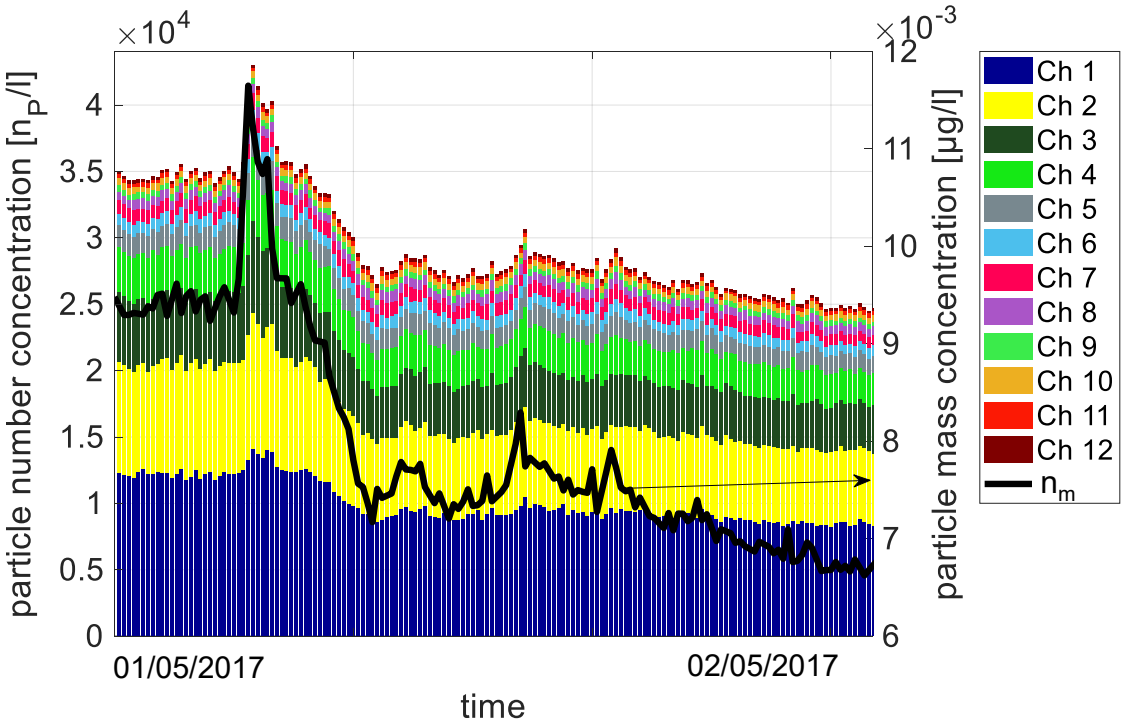

Figure 3.2. Stacked particle number concentration merge of EDM 164 channels 1-12 into CAMS bin 1/3 (left axis) and particle mass concentration (right axis), Missour

Averaged volumetric particle size distribution curves are shown in Figure 3.3 (PSA) and in Figure 3.4 (Missour). The curves are obtained by calculating the particle volume concentration with the measured minutely particle number concentration and with the effective diameter of each size bin. Then, the volume concentration is summed up for obtaining the reduced particle bins (three or eight). For each particle size, the values recorded during two years are averaged and plotted on double logarithmic scales. Building the sum of EDM 164 particle measurement channels to fewer bins affects the volumetric particle distribution. Small particles seem to weigh more in the overall distribution of the configurations NMMB 8, NMMB 3 and CAMS 3. In the original EDM 164 volumetric particle size distribution, particles with effective diameters of up to 30 µm are measured. The presentation of coarse particles for the CAMS model size bins is up to an effective diameter of 21 µm, the NMMB model size bins go only up to an effective diameter of 15 µm. While the original size distribution is dominated by large particles and the transition between small to large particles is a steeply inclined curve8ik at around d_P = 15 - 20 µm (PSA), the new size distribution is evener.

The deposition velocity of fine particles is dominated by Brownian motion and is for fix conditions slower than the deposition velocity for medium and coarse particles which are mainly affected by impaction (see Figure 2.8). This leads to the assumption that the change in particle size bins might lead to a lower calculated deposition velocity, a lower modelled projected surface coverage CR and thus a lower modelled soiling rate as compared to the calculated soiling rate using the original particle input data resolution because particles larger than 15 µm and 21 µm are underrepresented.

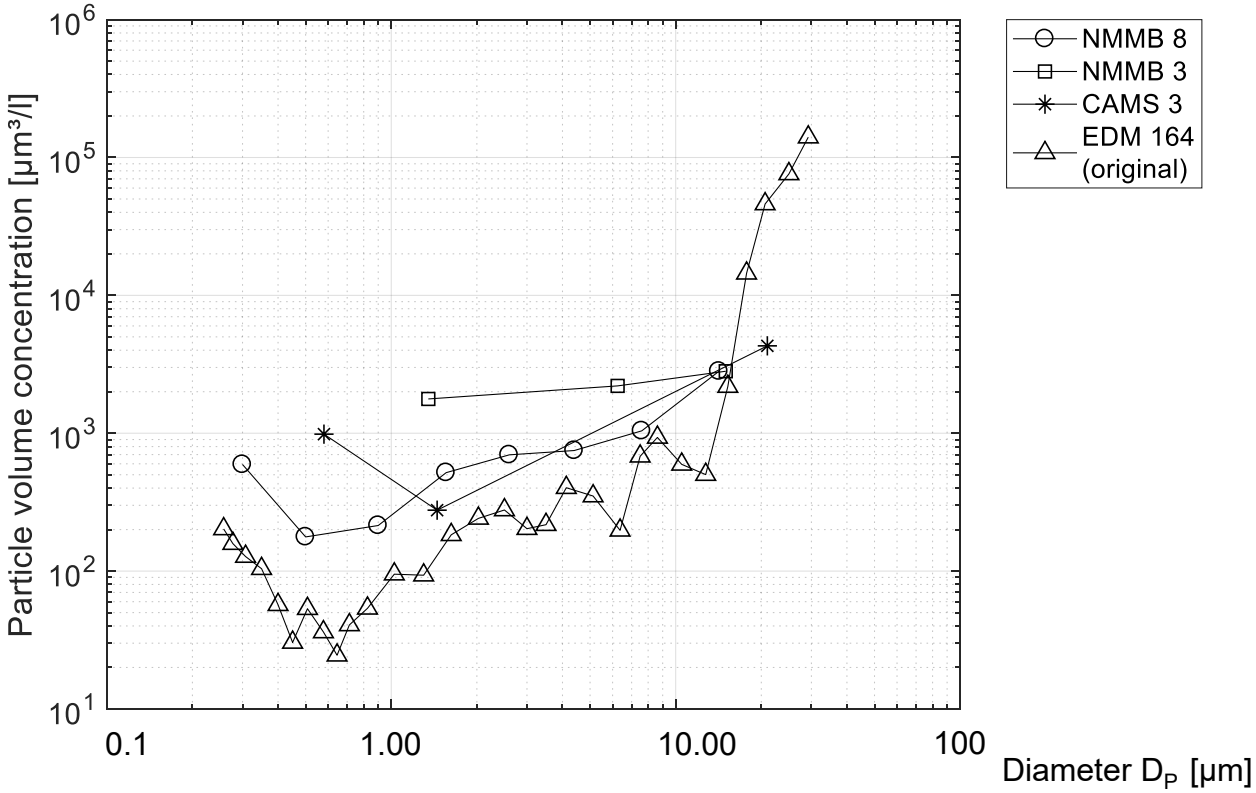

Figure 3.3. Averaged volumetric particle size distribution at PSA from January 2017 to March 2019 in different transport model configurations

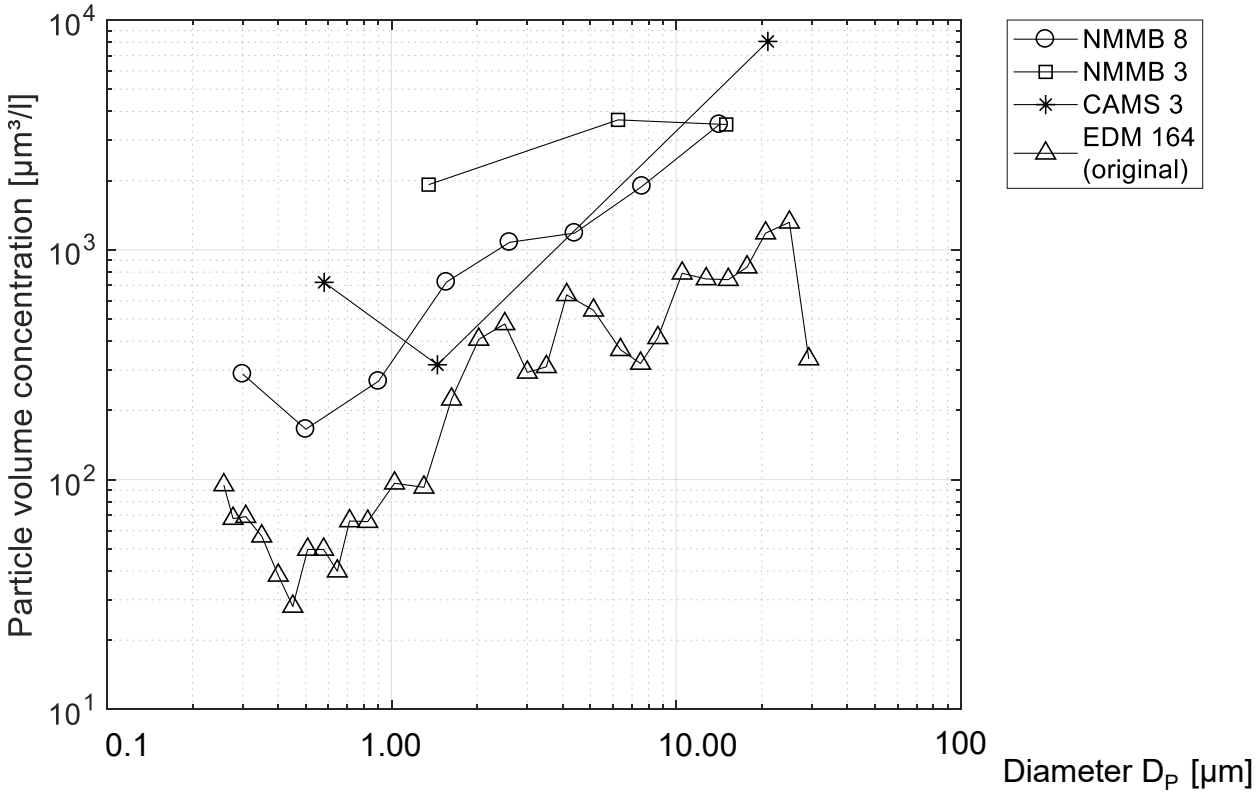

Figure 3.4. Averaged volumetric particle size distribution in Missour from January 2017 to October 2018 in different transport model configurations

3.2.2 Time resolution

The time resolution of the model data is three hours for both the NMMB Model and the CAMS Model. Most models exhibit 3-hourly averaged outputs, some other dust transportation models have different time resolutions ranging between one hour and one day [31]. Therefore in this subsection, time resolutions that are typically used in meteorological dust and aerosol models, namely averages of one hour, three hours and one day, are analysed to provide an overview about the possible range. The measurement values of PlaSolA and Missour are averaged over these periods and are compared to the data in the original time resolution to analyse the effects.

The original data (instantaneous measurements each minute) and the averages over one hour, three hours and one day of the wind speed (Figure 3.5), the relative humidity (Figure 3.6) and the particle number concentration (Figure 3.7, Figure 3.8) are shown as examples for the adaptation of input data. For each parameter, the effect of building averages over time periods is different and depends on parameter characteristics as on its variation. The hourly and 3-hourly averages describe the relative humidity and the particle concentration of channel 1 (Figure 3.7) well, whereas they do not capture well the more extreme variations of the wind speed and even less so the particle concentration of channel 20 (Figure 3.8). The reduction of the time resolution from minutely averages to hourly, 3-hourly and daily averages smooths the curves and information about extreme fluctuations of the different parameters is lost. This is more obvious for parameters which vary strongly even in short time intervals such as the wind speed and some particle concentrations. With the daily averages even more information is lost, merely a tendency over several days can be estimated and the typical fluctuations within a day, that many parameters have, are neglected.

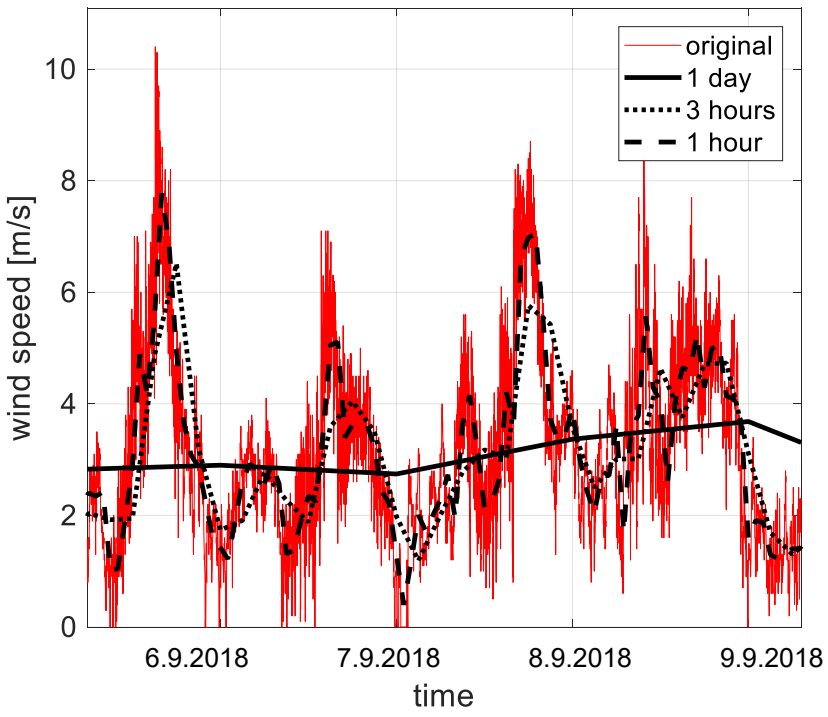

Figure 3.5. Wind speed data in original resolution and daily, 3 hourly and hourly averages at PSA

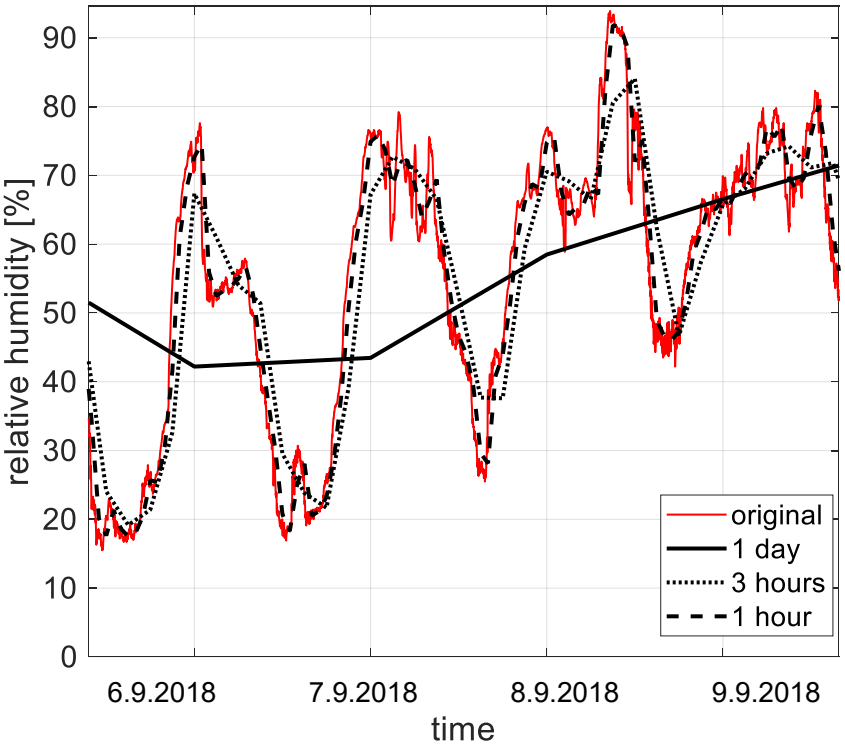

Figure 3.6. Relative humidity data in original resolution and daily, 3 hourly and hourly averages at PSA

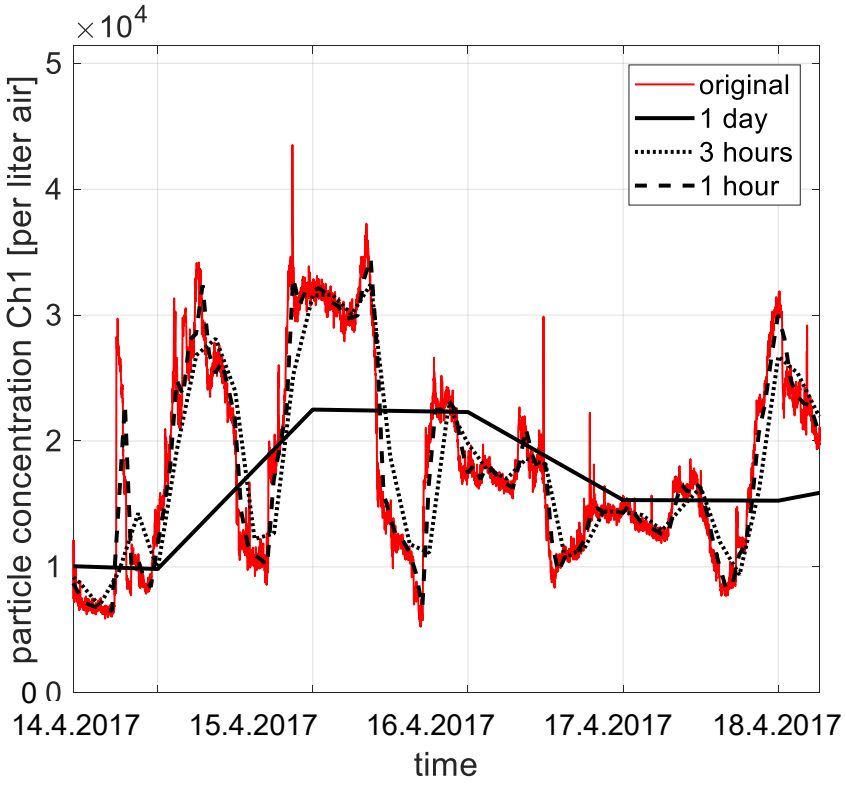

Figure 3.7. Particle number concentration channel 1 (EDM 164) data in original resolution and daily, 3 hourly and hourly averages at Missour

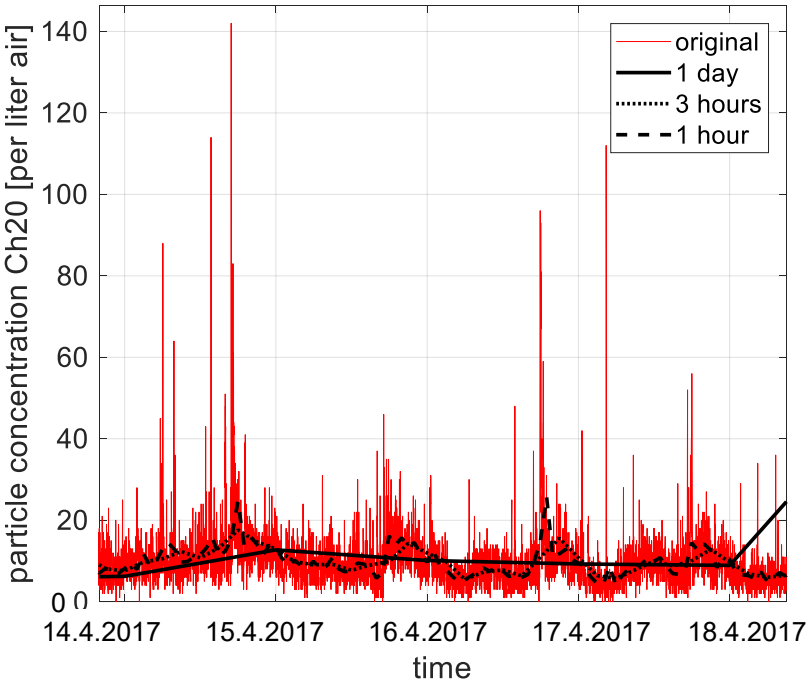

Figure 3.8. Particle number concentration channel 20 (EDM 164) data in original resolution and daily, 3 hourly and hourly averages at Missour

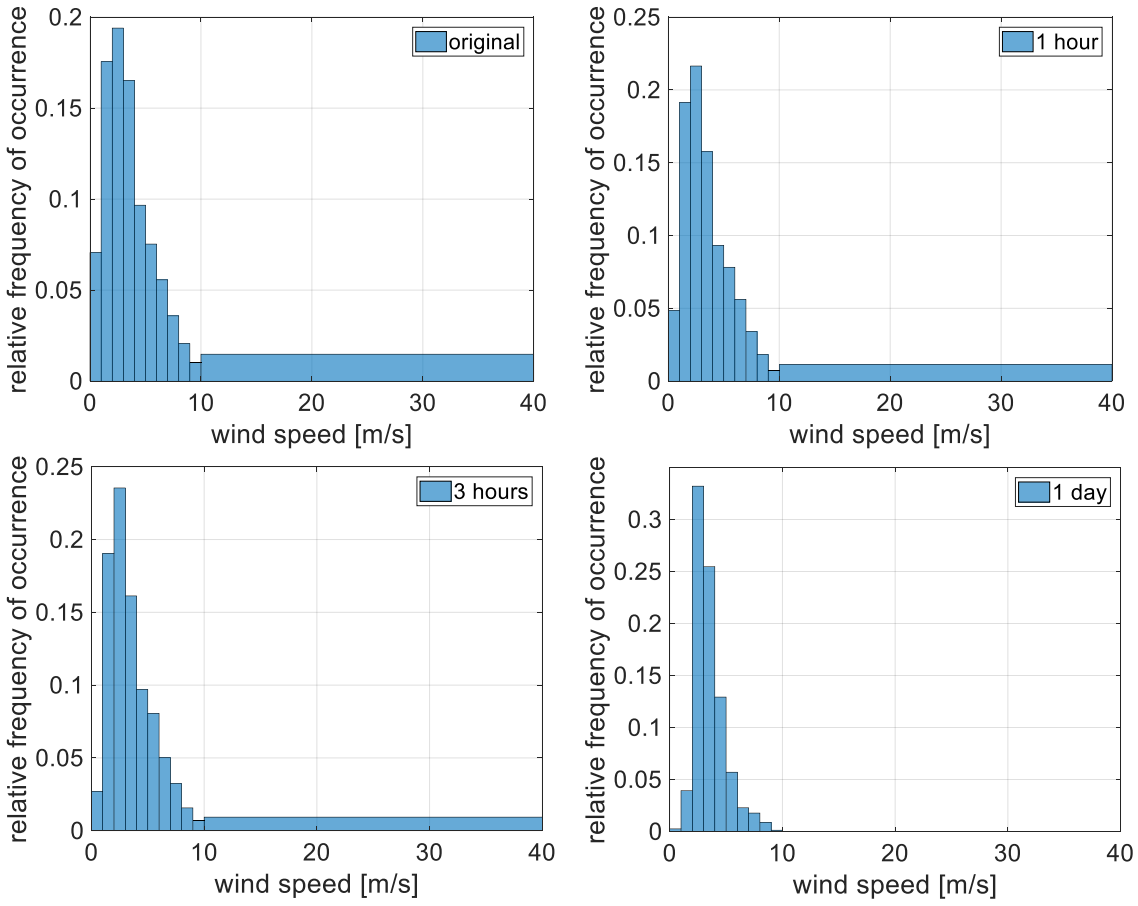

Figure 3.9. Wind speed histograms (PSA) for original resolution and 1-h, 3-h, daily averages from 01/2017 to 03/2019 in bins of 1 m/s up to 10 m/s and binned from 10 m/s to 40 m/s

Histograms for the wind speed at PlaSolA in different time resolution are shown in Figure 3.9. In comparison to the original minutely data, it is noticeable that the greater the time of averaging, the lower the number of extreme incidences. The share of high wind speeds from 10 m/s to 40 m/s, for example, reduces from around 2 % (original) to a non-detectable share (daily). Very low wind speeds from 0 m/s to 1 m/s and from 1 m/s to 2 m/s reduce from 7 % to 0.5 % and from 18 % to 4 % respectively. Wind speed occurrences centre more around a central value of 2 m/s to 4 m/s and the greater the averaging time, the more narrow the peak at these wind speeds.

This behaviour is confirmed by the standard deviation that is reduced with increasing time intervals. To compare the STD of the various parameters, c_v as the relative standard deviation is convenient (see equation 18). In Table 3.2 c_v is presented in the grey shaded fields.

Table 3.2. STD (white fields) and c_v (grey fields) for different time resolution of data

	PSA					Missour				
	Mean value	**original**	**1 hour**	**3 hours**	**1 day**	**Mean value**	**original**	**1 hour**	**3 hours**	**1 day**
wind speed [m/s]	3.53	STD=2.33	2.17	2.05	1.35	3.55	2.84	2.66	2.52	1.78
		c_v=0.66	0.61	0.58	0.38		0.80	0.75	0.71	0.50
wind direction [°]	139.34	99.55	84.70	79.45	58.36	154.37	108.92	89.49	82.45	62.95
		0.71	0.61	0.57	0.42		0.71	0.58	0.53	0.41
temperature [°C]	16.97	7.91	7.88	7.81	6.90	18.34	9.54	9.55	9.50	8.27
		0.47	0.46	0.46	0.41		0.52	0.52	0.52	0.45
relative humidity [%]	55.06	20.43	20.28	19.85	14.50	45.06	22.81	22.70	22.34	16.39
		0.37	0.37	0.36	0.26		0.51	0.50	0.50	0.36
pressure [hPa]	959.84	6.08	6.06	6.06	5.90	901.21	4.49	4.47	4.44	4.18
		0.01	0.01	0.01	0.01		0.00	0.00	0.00	0.00
particle number 1 [l^{-1}]	22545	19287	19002	18636	16094	10597	10678	9286	8212	6020
		0.86	0.84	0.83	0.71		1.01	0.88	0.77	0.57
particle number 2 [l^{-1}]	14102	14145	13910	13600	11369	6049	8653	6741	5533	3922
		1.00	0.99	0.96	0.81		1.43	1.11	0.91	0.65
particle number 3 [l^{-1}]	8367	9386	9216	8991	7339	4531	6490	4726	3977	3042
		1.12	1.10	1.07	0.88		1.43	1.04	0.88	0.67

For the wind speed and the wind direction, the variation changes considerably, with an STD decreasing from minutely to daily data to only 60 % of the original STD. The temperature and the relative humidity show a similar but less extreme reduction of variation, as they are parameters which do not fluctuate as strongly as the wind speed and direction. The pressure generally shows little variation itself and thus the reduction in variation with increasing interval averaging time is insignificant. Most of the particle number concentration values - in Table 3.2 the first three channels as examples – are highly fluctuating parameters (high c_v) but their decrease in variation for increasing time averages is not that significant as for the wind parameters.

The loss of information about extreme values of fluctuating parameters leads to the assumption that when using this data as soiling model input, the sensitivity of the model for extreme soiling events is reduced too.

3.3 Soiling model performance with reduced data resolution

After examining the changes in the adapted input data sets as compared to the original data set, the influence of using the adapted measurement data as input for the soiling model is tested and discussed in this section. This is implemented separately for both adaptations to map the eventual performance failures to their exact cause: for reduced particle size channels in subsection 3.3.1 and for reduced time resolution in 3.3.2. Since the soiling model does not consider cleaning events, days with rain events and positive soiling rates are excluded from the model parametrization and validation.

To assess the model quality, several statistical parameters are used. For an observed soiling rate $\hat{\xi}_{obs}$, a modelled soiling rate $\hat{\xi}_{model}$ and a number of evaluated days *n* the RMSE is calculated according to equation 19.

$$RMSE = \sqrt{\frac{1}{n} \cdot \sum_{i=1}^{n} \left(\hat{\xi}_{obs,i} - \hat{\xi}_{model,i}\right)^2} \tag{19}$$

The mean absolute deviation (MAD), also referred to as the positive difference of two given datasets, can be used to describe the statistical dispersion or variability and is calculated according to

$$MAD = \frac{1}{n} \cdot \sum_{i=1}^{n} \left|\hat{\xi}_{obs,i} - \hat{\xi}_{model,i}\right| . \tag{20}$$

The bias (equation 21) presents the overall deviation of the observed and the modelled soiling rate. For this parameter, positive and negative deviation values cancel out so it indicates whether the model generally tends to overestimate or underestimate the observation.

$$Bias = \frac{1}{n} \cdot \sum_{i=1}^{n} \left(\hat{\xi}_{obs,i} - \hat{\xi}_{model,i}\right) \tag{21}$$

The five-fold cross-validation method generates five parameter sets, each resulting from the training on the five different train sets. It also generates five different values of the stated evaluation criteria for each PSA train, PSA test and Missour set. To compare these values, the average values for RMSE, MAD, and bias of the five folds are calculated and the variation within the five folds is given in terms of their standard deviation STD_{RMSE}, STD_{MAD}, and STD_{bias}.

3.3.1 Influence of particle size channel resolution

The influence on the soiling model performance of using measured particle concentrations in lower size resolution is analysed and discussed in this section. The DLR particle concentration measurements at the locations PlaSolA and Missour are summarized to three and eight particle size bin measurements. In the soiling model code, the corresponding adaptations are implemented and the particle bins are included each with their effective bin diameter in the model equations (see Table 3.1). The average soiling rate in the considered period at PSA is -0.33 %/day. In Missour, the average observed soiling rate is -0.47 %/day. The statistical parameters quantifying the model performance are presented in Table 3.3. For the original input data, the RMSE of the PSA test set is 0.527 ± 0.298 %/day, the absolute deviation is 0.348 %/day and the bias is -0.142 %/day. Compared to the TraCS reference instrument accuracy of 0.2 %/day the bias is in an acceptable range [21]. Due to the large variation within the five-fold validation for the PSA test set (see Figure 3.10 on the left) no general tendency of a decreased model performance with adapted particle size distribution at PSA can be concluded. Instead, the loss in detailed information on the particle size distribution seems to have little impact on the model performance for the PSA validation set. For the Missour data set, the model performance with original input data is worse in comparison to PSA, with an RMSE of 0.667 ± 0.011 %/day, an MAD of 0.421 %/day and a bias of -0.319 %/day. The soiling rate predicted by the soiling model underestimates the observed soiling rate slightly. The variation within the five-fold validation process is smaller for Missour than for PSA, identifiable as the small STDs in the boxplot diagrams presented in Figure 3.10, where the RMSEs obtained in the five-fold cross-validation are shown (see Appendix B.1 for MAD and bias ranges). The red horizontal line in the box is the median value and the red central mark represents the mean value of each RMSE set. For Missour it can be concluded that using the particle bin distribution according to NMMB 3 results in an increasing RMSE of about 11 % (including the STD to reduce the value, regarding the given variation). The MAD is 16 % larger than the original and the absolute value of bias increases by 46 %.

Table 3.3. Soiling model performance with ground measurement data in different particle size bin resolutions; mean values of criteria and STDs of the five-fold validation process

	particle resolution:	RMSE [%/day]	STD_{RMSE} [%/day]	MAD [%/day]	STD_{MAD} [%/day]	bias [%/day]	STD_{bias} [%/day]
PSA Train	**original**	0.547	0.074	0.329	0.051	-0.106	0.058
	NMMB 3	0.530	0.079	0.295	0.046	-0.146	0.062
	CAMS 3	0.533	0.080	0.308	0.059	-0.104	0.039
	NMMB 8	0.553	0.073	0.314	0.050	-0.129	0.049
PSA Test	**original**	0.527	0.298	0.348	0.188	-0.142	0.292
	NMMB3 3	0.651	0.313	0.386	0.189	-0.246	0.264
	CAMS 3	0.528	0.306	0.354	0.184	-0.111	0.354
	NMMB 8	0.537	0.296	0.348	0.180	-0.136	0.309
Missour	**original**	0.667	0.011	0.421	0.013	-0.319	0.022
	NMMB 3	0.759	0.008	0.510	0.008	-0.500	0.011
	CAMS 3	0.649	0.008	0.406	0.008	-0.272	0.048
	NMMB 8	0.679	0.005	0.431	0.006	-0.327	0.024

The modelled against the measured spoiling rate is plotted for different particle bin distributions in Figure 3.11 for the PSA validation set. The soiling rates are binned in steps of 0.05 %/day (x-axis) to reduce the number of displayed markers.

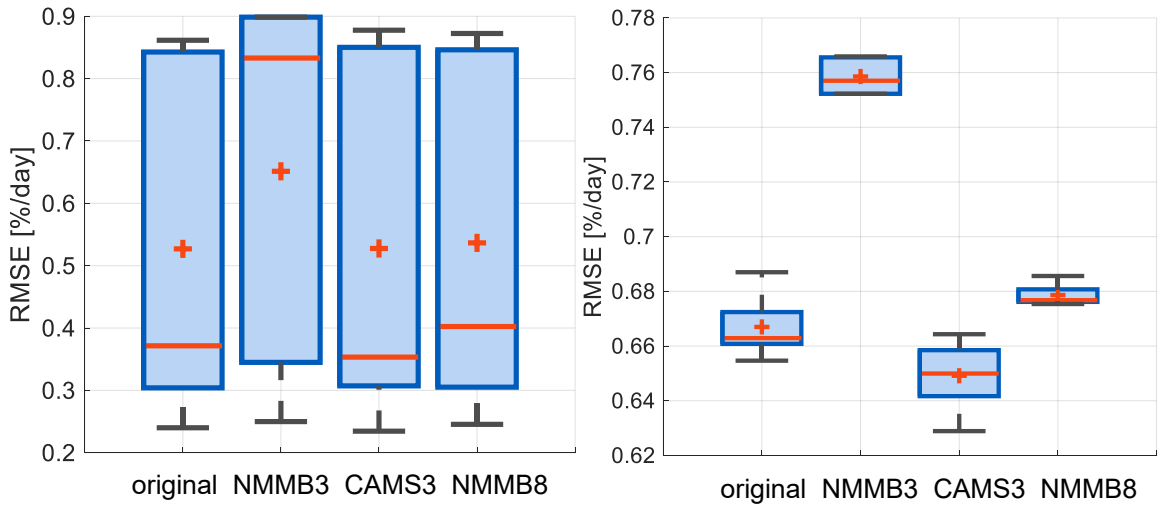

Figure 3.10. RMSE values for 5-fold validation on PSA test set (left) and Missour set (right); red central mark: mean, red line: median and blue box: variation of the five-fold validation process

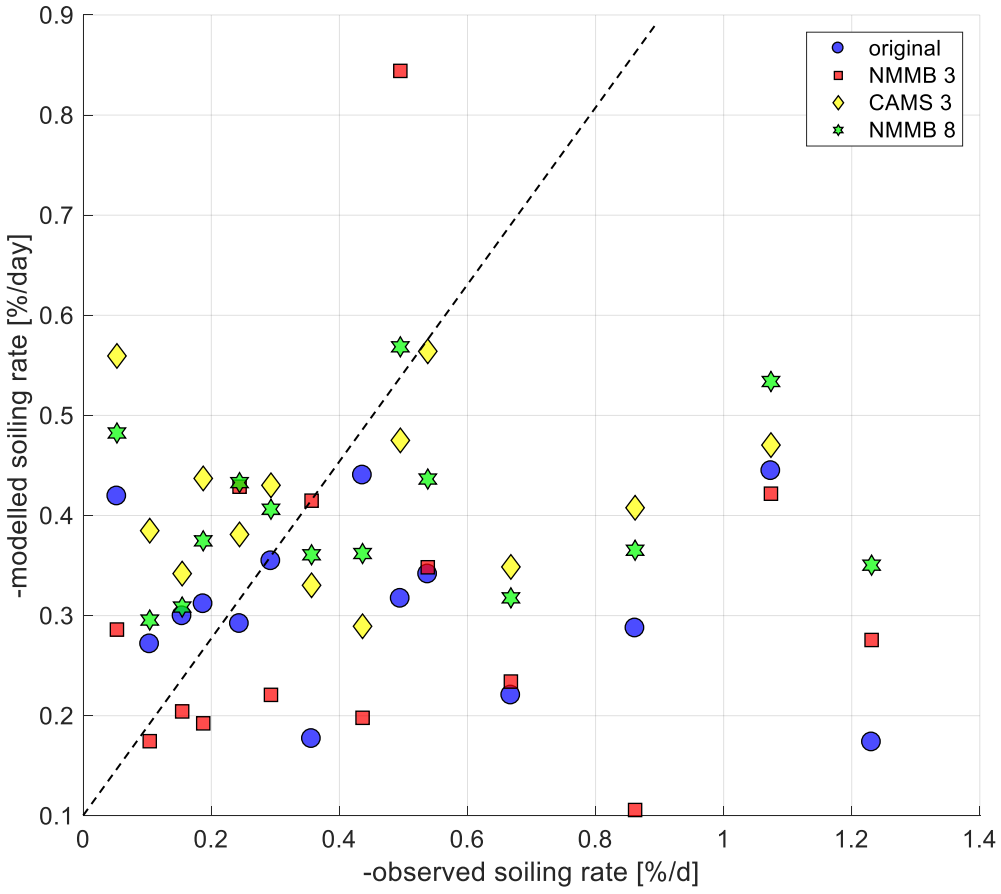

Figure 3.11. Modelled vs. observed soiling rate for different particle size bins PSA Test set from 25/07/2018 to 09/10/2018 with 57 soiling rate measurements, k = 3

Figure 3.12 shows the modelled and measured soiling rates for different particle bin classifications for the Missour set. Here, the soiling rate information is summarized in bins of 0.1 %/day. The underestimation of the modelled soiling rate using the NMMB 3 modification is recognizable while the other modifications result in a similar range of modelled soiling rates as the original particle size distribution. It seems to partly confirm the expectation that the increased weight on smaller and medium particle sizes (see Figure 3.4) results in a lower modelled soiling rate. To generate the first of three NMMB 3 particle bins, the first 16 EDM 164 particle channels (0.25 µm - 2.75 µm) are summed up and processed in the soiling model with an effective diameter of 1.35 µm. The sum of the next seven EDM 164 channels (2.75 µm - 11.75 µm) represents the second NMMB 3 bin with an effective diameter of 6.25 µm. This is a loss of information, as compared to the process of using each of the 30 bins with their corresponding effective particle diameter (see Appendix Table A.1). The three particle bins as defined in the CAMS model have boundaries that summarize the first 12 channels to a fine particle class, the next two channels to a medium class and the last 16 channels to the third coarse bin.

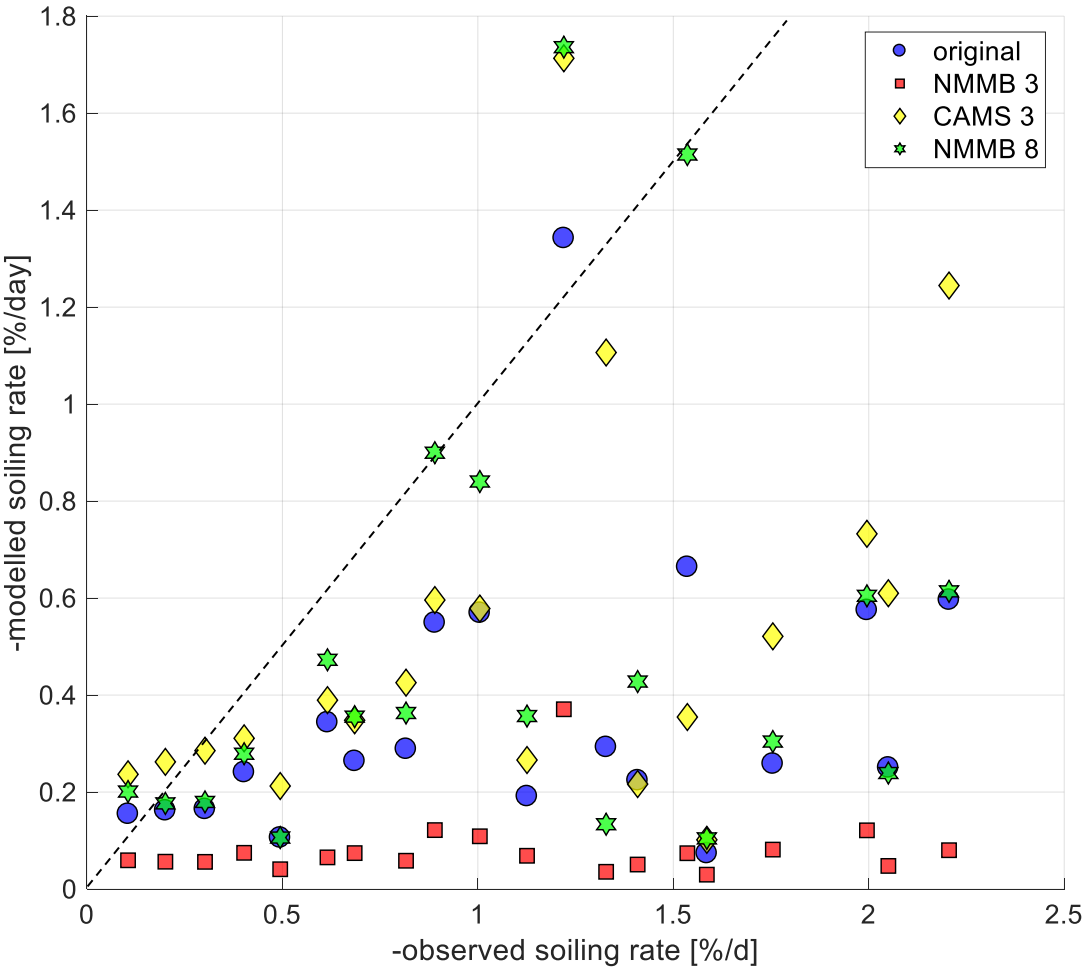

Figure 3.12. Modelled vs. observed soiling rate for different particle size bins Missour set from 03/02/2017 to 21/03/2018, 310 days with measured soiling rates, k = 1

3.3.2 Influence of temporal resolution

The soiling model performance with input data consisting of recorded measurements at the DLR sites in reduced time resolutions of one hour, three hours and one day is tested, analysed and compared to the original input data use (minutely resolution) in this subsection.

In Table 3.4 the soiling model quality analysis is shown in terms of statistical parameters. The variation of the five-fold validation results of the RMSE, the MAD and the bias of the PSA test set is large as their standard deviations are more than half of the average values (for RMSE and MAD) and almost double of the absolute bias values. In Figure 3.13 the variation of the RMSE is visualized as boxplot diagram, the according plots for the MAD and the bias follow the same characteristics (see Appendix B.2). Degradation in soiling model performance for lower timer resolutions is not noticeable for the PSA test set. For the Missour set, the variation is less thus it can be concluded that the switch from minutely to hourly resolution does not have a great impact on the soiling model performance. The switch to three hourly averages as input data even seems to decrease the model error slightly: the RMSE reduces about 4 %, the MAD decreases about 12 % and the absolute bias reduces about 16 %. The use of daily averages impacts the soiling model performance negatively for the Missour data set, as the RMSE increases by 5 % and the MAD by 1 %. The absolute bias value increases by 5 % when using daily averaged input data as compared to using minutely measurement data.

Table 3.4. Statistical evaluation of the soiling model performance with ground measurement data for different time resolutions; mean values of criteria and STDs of the five-fold validation process

	time averaging:	RMSE [%/day]	STD_{RMSE} [%/day]	MAD [%/day]	STD_{MAD} [%/day]	bias [%/day]	STD_{bias} [%/day]
PSA Train	original	0.547	0.074	0.329	0.051	-0.106	0.058
	1h resolution	0.547	0.071	0.325	0.054	-0.110	0.037
	3h resolution	0.564	0.076	0.343	0.057	-0.113	0.045
	1d resolution	0.557	0.061	0.302	0.038	-0.155	0.033
PSA Test	original	0.527	0.298	0.348	0.188	-0.142	0.292
	1h resolution	0.555	0.292	0.370	0.186	-0.146	0.310
	3h resolution	0.553	0.315	0.380	0.215	-0.141	0.331
	1d resolution	0.493	0.267	0.309	0.152	-0.134	0.221
Missour	original	0.667	0.011	0.421	0.013	-0.319	0.022
	1h resolution	0.668	0.010	0.406	0.008	-0.306	0.037
	3h resolution	0.626	0.005	0.353	0.003	-0.203	0.044
	1d resolution	0.726	0.012	0.448	0.008	-0.335	0.047

In Figure 3.14 the modelled soiling rates are plotted against the measured soiling rates for different time resolutions for the PSA validation set (bins of 0.05 %/day on the x-axis). The switch from minutely to hourly or daily data does not have a noticeable impact on the soiling model performance in this case. In Figure 3.15 the according soiling rates are plotted for the Missour set, in bins of 0.1 %/day of the observed soiling rate. Often the modelled soiling rates for different time resolutions coincide or lie within a small range.

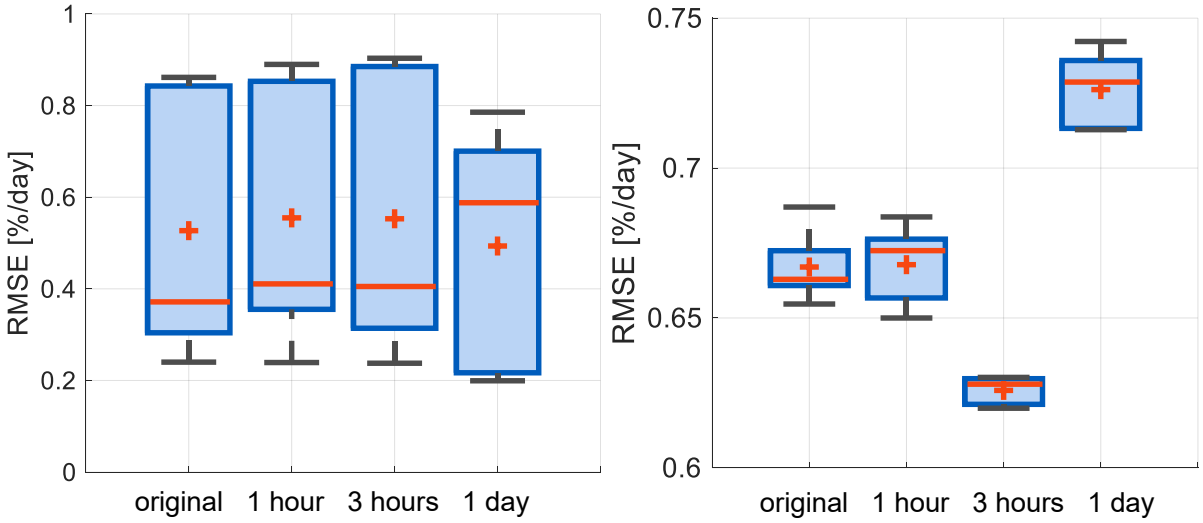

Figure 3.13. RMSE values for 5-fold validation on PSA test set (left) and Missour set (right); red central mark: mean, red line: median and blue box: variation of the five-fold validation process

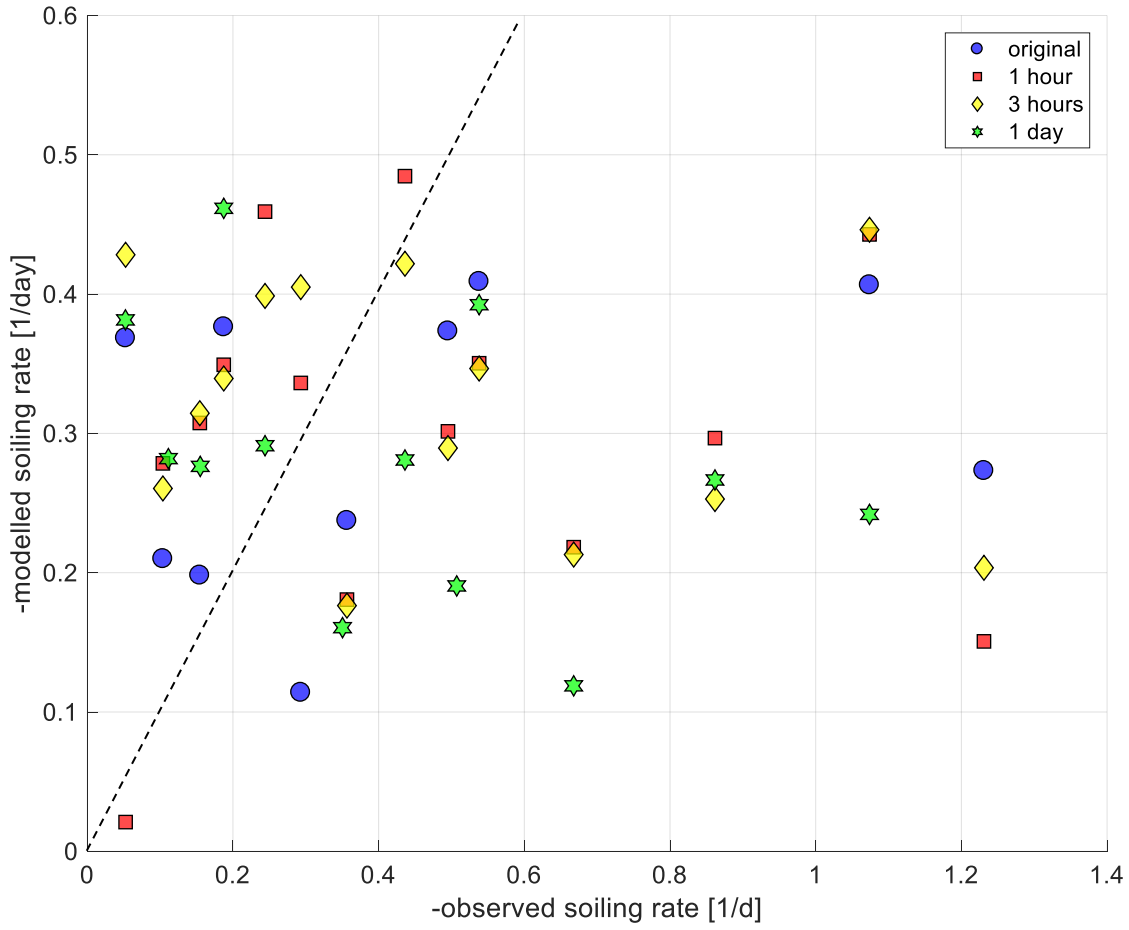

Figure 3.14. Modelled vs. observed soiling rate for different time resolutions PSA Test set from 25/07/2018 to 09/10/2018 with 57 soiling rate measurements, k = 3

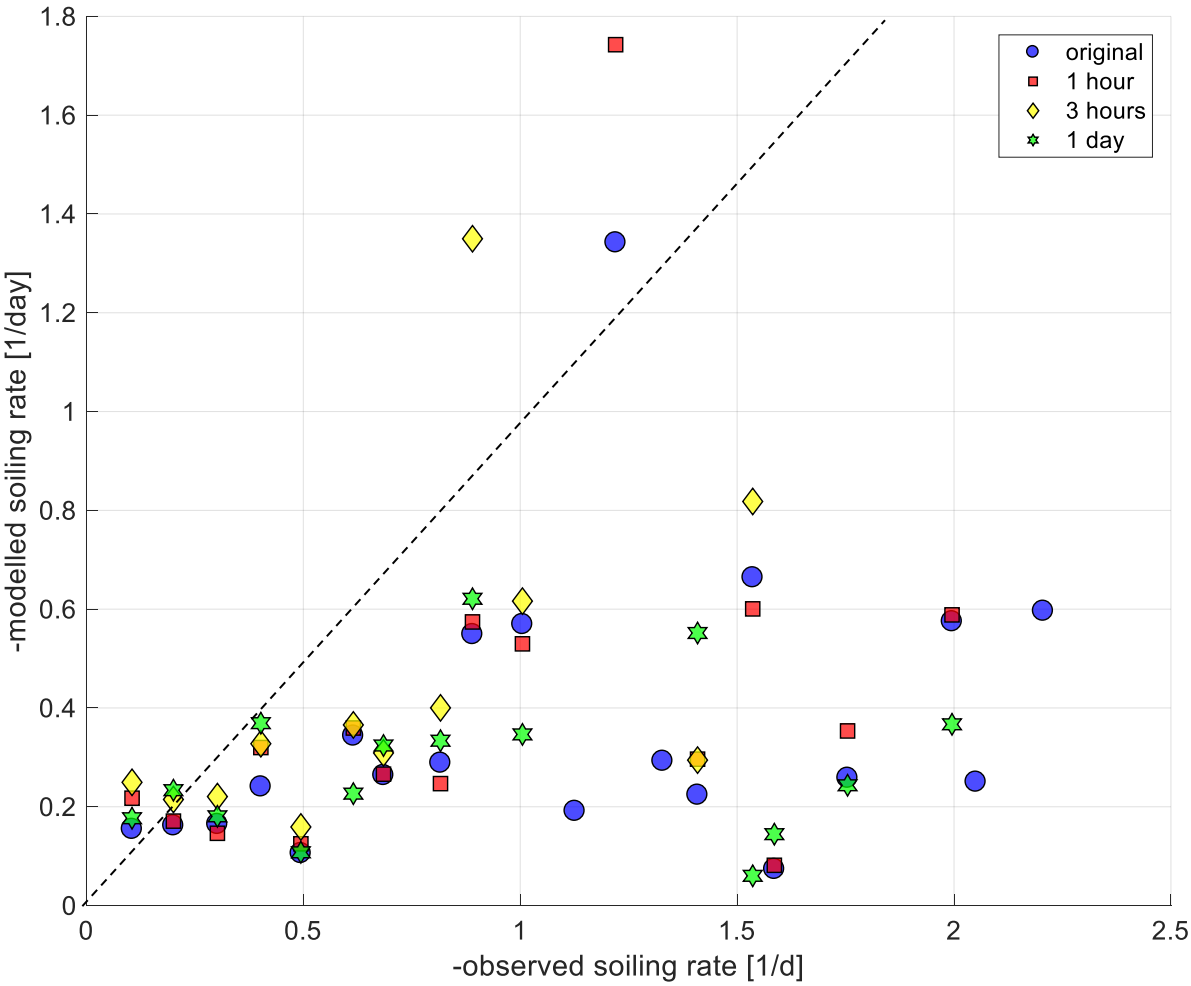

Figure 3.15. Modelled vs. observed soiling rate for different time resolutions Missour set from 03/02/2017 to 21/03/2018, 310 days with measured soiling rates, k = 1

The assumption that with input data of lower time resolution the model's sensitivity for extreme events is reduced is tested analysing the relative number of occurrences of modelled soiling rates, shown in the histograms for the PSA test set (Figure 3.16) and the Missour set (Figure 3.17). Regarding the PSA test set, the modelled soiling rate originally lies within a range of 0 - 0.8 %/day, the most common modelled soiling rates (38 %) are between 0.2 and 0.3 %/day. For hourly and three-hourly averages this does not change much, but for using daily averages, the modelled soiling rate window is only up to 0.4 %/day, half as large as the original possible range of soiling rate predictions. Additionally, over half of the modelled soiling rates are centred on the value of 0.2 %.

The change of distribution in the Missour soiling rate predictions is similar: while for original input data time resolution the modelled soiling rate is up to 2.4 %/day, the hourly resolved data predicts rates up to 1.8 %/day, the three-hourly up to 1.2 %/day and the daily resolution results in predictions of up to 1.1 %/day.

With averaged input data over increasing time intervals, the model's sensitivity for modelling high soiling rates is reduced.

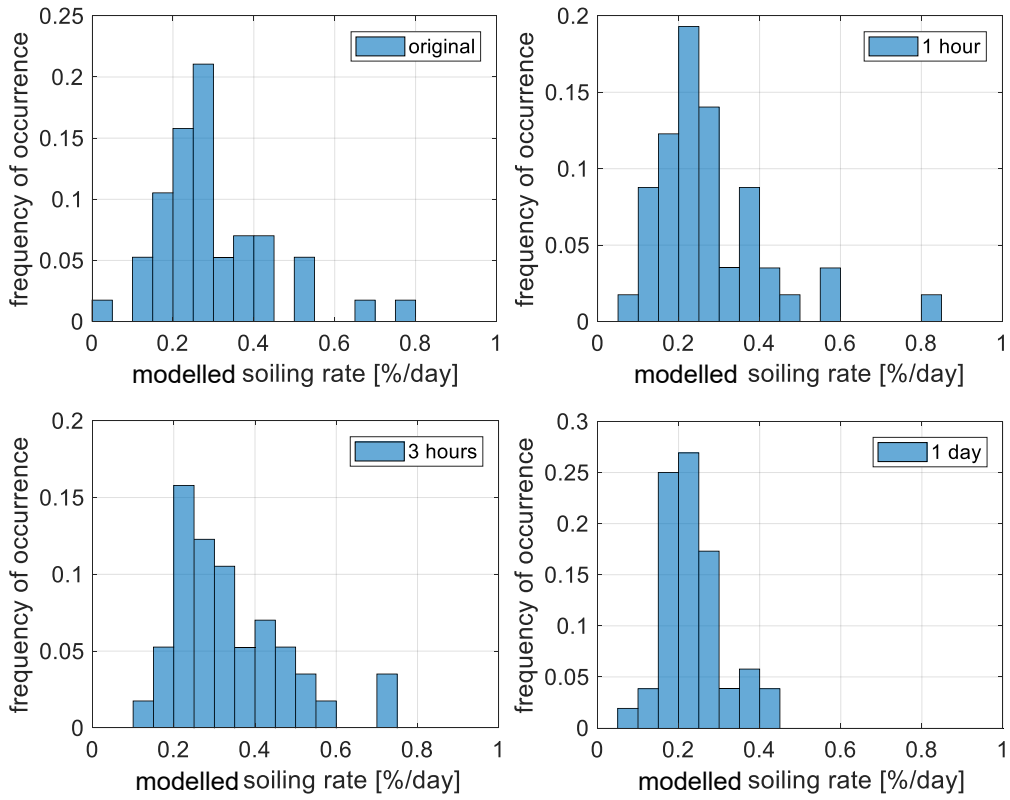

Figure 3.16. Modelled soiling rate distribution for different input data time resolution (PSA test, k = 2)

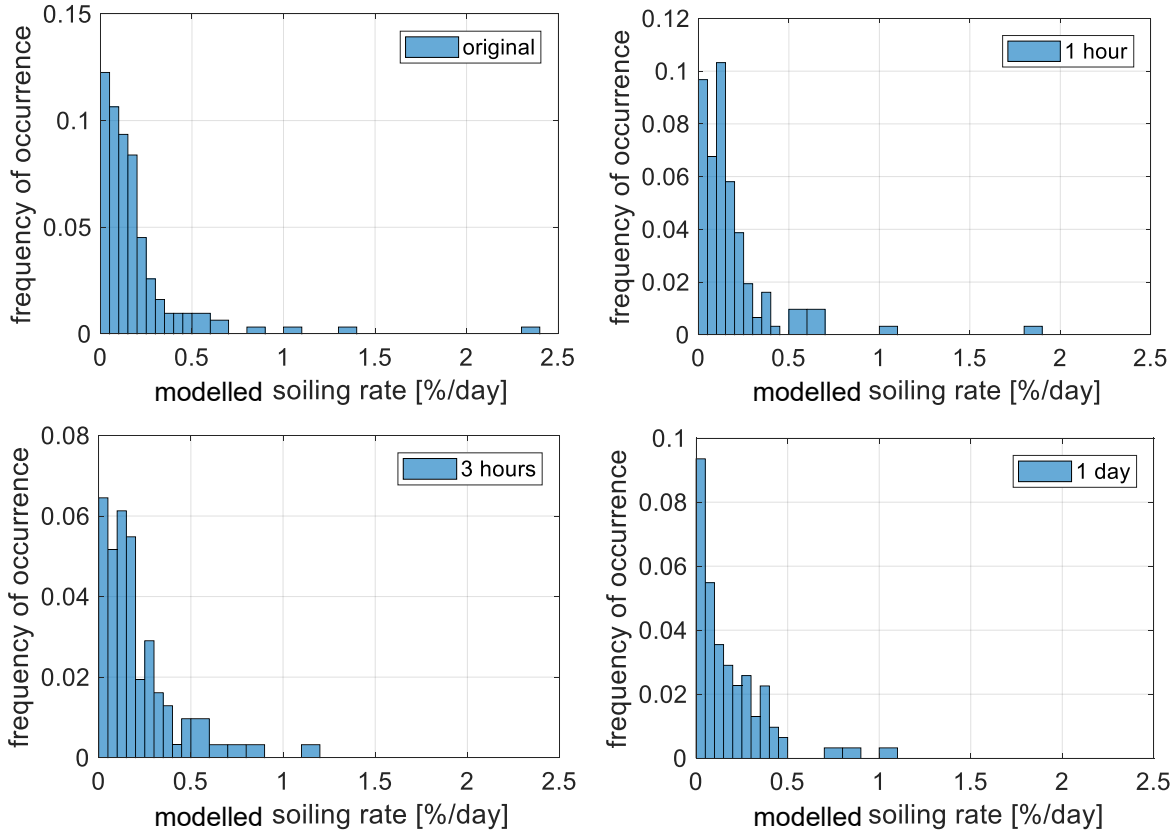

Figure 3.17. Modelled soiling rate distribution for different input data time resolution (Missour, k = 2)

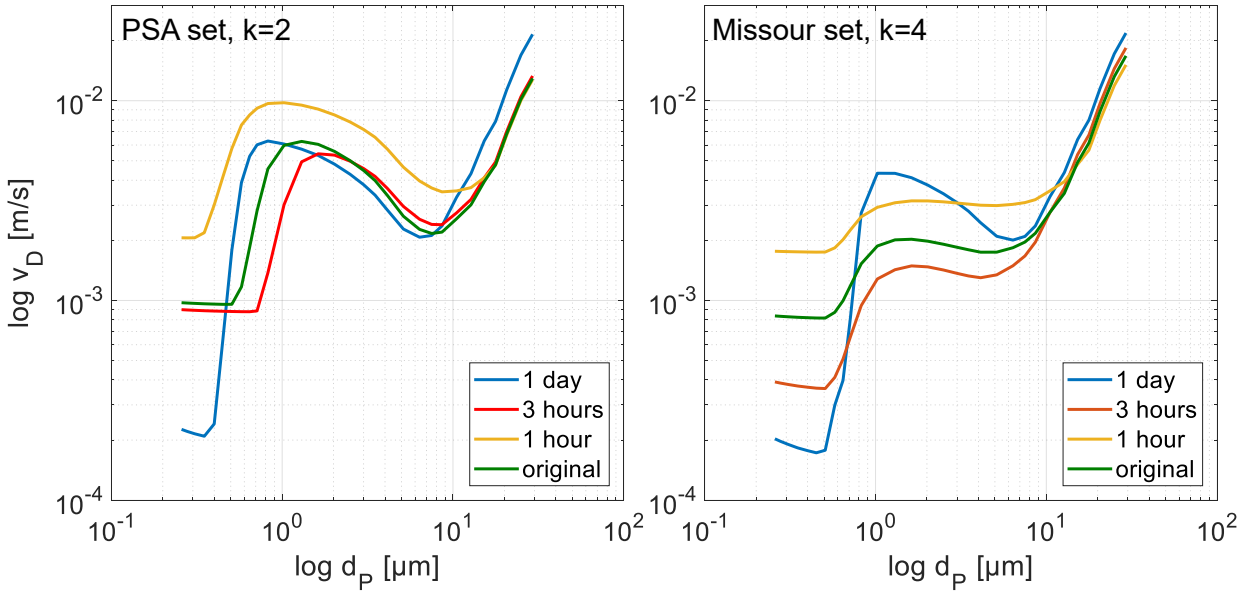

Figure 3.18. Mean deposition velocity against particle diameter for different time resolutions of input parameters

The mean deposition velocities of particles adhering on the mirror surface are shown in Figure 3.18 for different particle sizes on logarithmic scales. For particles larger than d_P = 10 µm the deposition velocity is almost not influenced by the change in time resolution. For fine particles (d_P < 0.5 µm) the daily resolution leads to a smaller deposition velocity as compared to the original time resolution in minutes. This may be the result of the underrepresentation of high wind speeds for daily averaging as it is discussed in 3.2.2. High wind speeds generally favour the deposition of small particles. The deposition velocities for medium-sized particles in the range of 0.5 µm to 10 µm do not show a clear tendency between the time resolutions.

In this chapter, it is shown that the original size distribution is dominated by large particles and the transition between small to large particles is sharp. For the new size distribution, small particles weigh more in the overall distribution. The reduction of the time resolution from minutely averages to hourly, 3-hourly and daily averages smooths the curves and information about extreme values of the different parameters is lost. The loss of information about extreme values is more severe for strongly fluctuating parameters such as the wind speed and particle concentrations.

The underestimation of the soiling rate for using ground measurement data in the NMMB 3 particle bin modification is recognizable while the other modifications result in a similar range of modelled soiling rate as the original particle size distribution.

For soiling model input data with lower time resolution, little significant impact is noticed on the PSA test set while for the Missour set the model error increases for averaging input parameters over one day. Averaging input data over increasing time intervals generally decreases the model's ability to predict high soiling rates correctly.

4 Integrating aerosol transport models into soiling model

In this chapter, the use of the data obtained from aerosol transport models as input for the soiling model is implemented. To track the process and to justify the soiling model performance with transport model input data as the final result, a stepwise adaptation and integration are realized.
Initially, a method is described which enables the extension of the aerosol particle concentration data from three provided transport model particle size bins to 30 particle size bins (section 4.1). The approach is based on the particle size distribution curve obtained from measurements at PlaSolA.
Next, in section 4.2 the transport model data is compared to the measured data at both locations. The quantification of correlation between the input data sets is essential to proceed with using it in the soiling model. The data intercomparison is implemented separately for the NMMB model (in subsection 4.2.1) and the CAMS model (in subsection 4.2.2).
After adapting the soiling model to the transport model input data format, it is then parametrized and validated with the aerosol transport model input data. The process of parametrization and validation is implemented according to the previous approach with splitting the PSA data set into train and test set and using a five-fold validation. The results of using aerosol transport model data as input in the soiling model are presented and discussed in section 4.3.

4.1 Extension of particle size bins

In the current version of the soiling model, the particle number concentration in numbers of particles per litre of air n_n in 30 size channels is an input variable. This very detailed information about the particle concentration is obtained by a measurement with the EDM 164 particle counter (details about the device and its measurement uncertainty see subsection 2.4.1) and is an outstanding factor in the soiling model performance accuracy. The output of aerosol transport models has usually less particle size bins, current models use from two up to nine size bins [31].

In the current version of the NMMB Model the atmospheric composition is expressed by three size bins: $PM_{2.5}$, PM_{10}, and PM_{20} in kg/m^3. To obtain more detailed information regarding the particle size distribution within these three comprehensive bins, the average particle size distribution curve measured at PlaSolA from January 2017 to March 2019 is used. With this information, it is possible to convert the three particle size bins artificially into 30 size bins.

The generalization of the site-specific aerosol size distribution is acceptable because the number and the volume distribution curves of atmospheric aerosol particles are found to be the similar typical log-normal distribution function for different locations (see Figure 2.3) [16]. It is nevertheless necessary to create a new particular distribution function of the on-site aerosol particle measurements since the EDM 164's measurement range starts from d_P = 0.25 µm and measures up to coarse particles, which are not presented in the distribution functions found in the literature. The particle number and the particle volume distribution for the location PlaSolA are presented on a double-logarithmic scale in Figure 4.1.

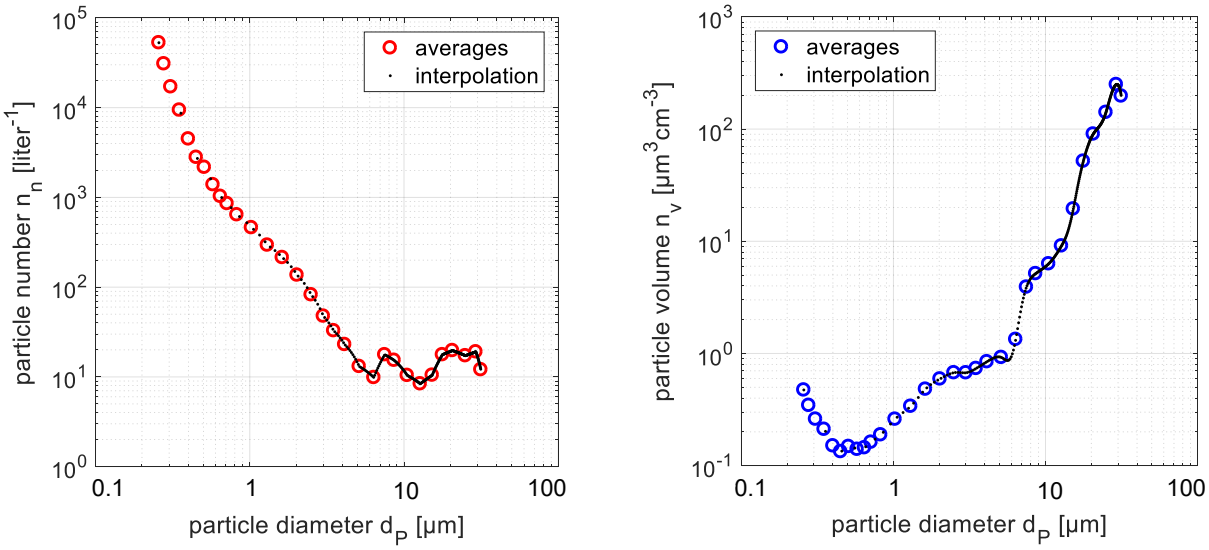

Figure 4.1. Particle number (left) and volume (right) size distribution at PlaSolA from 01/2017 to 03/2019, minutely measurements

With the obtained aerosol volume distribution it is possible to determine weighting factors for each one of the 30 size channels to calculate the particle concentration in these channels from the three particle size bins. The ranges of the three bins within the 30 channels are presented in Figure 4.2.

For the NMMB model, to determine the mass of particles in one of the 30 size channels *i* as a function of the PM values, the following equations are used:

$$for\ 1 \le i \le 15: \quad m_{2.5,i} = PM_{2.5} \cdot w_{2.5,i} \tag{22}$$

$$for\ 16 \le i \le 23: \quad m_{10,i} = (PM_{10} - PM_{2.5}) \cdot w_{10,i} \tag{23}$$

$$for\ 24 \le i \le 30: \quad m_{20,i} = (PM_{20} - PM_{10}) \cdot w_{20,i} \tag{24}$$

The weighting factors $w_{2.5/10/20,i}$ are calculated according to equations 25 to 27, the values are listed in Table A.2 in the annex. The average values for the volumetric particle concentrations are obtained with the volume size distribution curve resulting of two years measurements at PSA (see Figure 4.1); these averages $\overline{n_{v_i}}$ are listed in Table A.1 in the annex.

$$w_{2.5,i} = \frac{\overline{n_{v_i}}}{\sum_{i=1}^{15} \overline{n_{v_i}}} \tag{25}$$

$$w_{10,i} = \frac{\overline{n_{v_i}}}{\sum_{i=16}^{23} \overline{n_{v_i}}} \tag{26}$$

$$w_{20,i} = \frac{\overline{n_{v_i}}}{\sum_{i=24}^{30} \overline{n_{v_i}}} \tag{27}$$

In the CAMS Model, the aerosol particle concentration is provided for 7 different aerosol species: dust, sea salt, hydrophilic organic matter, hydrophobic organic matter, hydrophilic black carbon, hydrophobic black carbon and sulphate. Dust and sea salt are divided each into three size bins with different limits for dust and salt (see Table 2.1). To convert the given aerosol particle concentration into 30 size bins, several weighting factors for dust, salt and the other aerosol species are applied.

The difference between the particle size bin ranges and the according limits for the EDM 164 particle counter measurement and the transport model output (NMMB Model and CAMS Model) is presented in Figure 4.2.

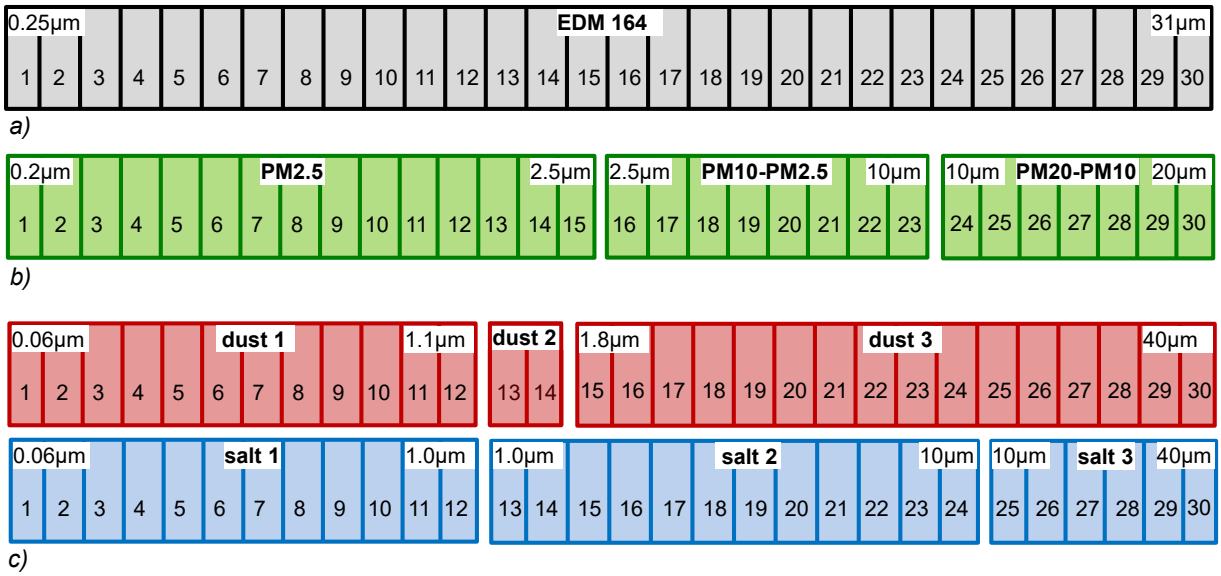

Figure 4.2. Distribution of aerosol particle bins for the output of EDM 164 (a), NMMB Model (b) and CAMS Model (c)

For the CAMS Model the particle concentration conversion is achieved with three weighting factors for each dust and sea salt aerosol particles according to the following equations (values of the weighting factors are listed in the Appendix in Tables A.3, A.4 and A.5):

$$w_{dust1,i} = w_{salt1,i} = \frac{\overline{n_{v_i}}}{\sum_{i=1}^{12} \overline{n_{v_i}}} \tag{28}$$

$$w_{dust2,i} = \frac{\overline{n_{v_i}}}{\sum_{i=13}^{14} \overline{n_{v_i}}} \tag{29}$$

$$w_{dust3,i} = \frac{\overline{n_{v_i}}}{\sum_{i=15}^{30} \overline{n_{v_i}}} \tag{30}$$

$$w_{salt2,i} = \frac{\overline{n_{v_i}}}{\sum_{i=13}^{24} \overline{n_{v_i}}} \tag{31}$$

$$w_{salt3,i} = \frac{\overline{n_{v_i}}}{\sum_{i=25}^{30} \overline{n_{v_i}}} \tag{32}$$

One overall weighting factor w_{total} is applied to the other aerosol species which do not have specified any size boundaries in the CAMS Model; organic matter, black carbon and sulphate:

$$w_{total,i} = \frac{\overline{n_{v_i}}}{\sum_{i=1}^{30} \overline{n_{v_i}}} \tag{33}$$

The particle mass from which the particle number concentration can be calculated with the effective channel diameter and the particle density is obtained similarly to how it is done for the NMMB Model.

In each size channel *i* the total channel particle mass $m_{total,i}$ is calculated according to one of the following equations, depending on the channel number.

$$for\ 1 \leq i \leq 12: \quad m_{total,i} = m_{dust1} \cdot w_{dust1,i} + m_{salt1} \cdot w_{salt1,i} + m_{org+blacarb+sulph} \cdot w_{total,i} \tag{34}$$

$$for\ 13 \leq i \leq 14: \quad m_{total,i} = m_{dust2} \cdot w_{dust2,i} + m_{salt2} \cdot w_{salt2,i} + m_{org+blacarb+sulph} \cdot w_{total,i} \tag{35}$$

$$for\ 15 \leq i \leq 24: \quad m_{total,i} = m_{dust3} \cdot w_{dust3,i} + m_{salt2} \cdot w_{salt2,i} + m_{org+blacarb+sulph} \cdot w_{total,i} \tag{36}$$

$$for\ 25 \leq i \leq 30: \quad m_{total,i} = m_{dust3} \cdot w_{dust3,i} + m_{salt3} \cdot w_{salt3,i} + m_{org+blacarb+sulph} \cdot w_{total,i} \tag{37}$$

In order to calculate the particle number in each channel $n_{P,i}$ the calculated particle mass in channel *i* $m_{P,i}$ (for NMMB $m_{2.5/10/20,i}$ and for CAMS $m_{total,i}$) the effective diameter $d_{eff,i}$ and the particle density ρ_P = 2650 kg/m^3 are used (equation 38). Effective channel diameters are listed in Table A.1 in the annex.

$$n_{P,i} = \frac{V_{totalP,i}}{v_{P,i}} = \frac{m_{P,i}}{\rho_P} \cdot \frac{1}{\pi \cdot \frac{1}{6} \cdot {d_{eff,i}}^3} \tag{38}$$

4.2 Data intercomparison

The data used as input in the soiling model for parametrization and validation is strongly affecting the soiling model performance. Therefore it is crucial to compare the aerosol transport model data sets to the measured reference data set to assess the input data quality. In this chapter firstly the additional statistical evaluation methods are presented. This is required to subsequently analyse the results and to discuss the findings in subsections 4.2.1 (NMMB Model) and 4.2.2 (CAMS Model) concerning the intention of the intercomparison: the substitution of the reference data set with the model data set to use it in the adapted soiling model.

The DLR data set is composed of meteorological parameters measured from January 2017 to March 2019 at PlaSolA in Tabernas and from January 2017 to October 2018 in Missour. This data is referred to as respectively *DLR reference data set* in this chapter. The transport model data sets obtained from meteorological and aerosol transport models are referred to as *model data set*. In an optimal case reference data set and model data set should correlate well with possible small deviations caused by model inaccuracy. To quantify the correlation of two parameters, several statistical criteria are used to compare meteorological values of the measurements (reference: x_i) and the models (y_i). For the evaluation of the data comparison in this chapter, mean values of both datasets, the bias, the standard deviation STD, the root mean square error RMSE and the Pearson correlation coefficient PCC (equation 40) are calculated for each parameter. The mean values are the averages of the investigated parameter over the specific period. The statistical bias expresses the average deviation between the two datasets, where *n* denotes the number of data (equation 21). The general tendency of the model data set to overestimate the reference dataset is indicated by negative

values, underestimation is captured by positive values. The bias should be interpreted cautiously because positive and negative errors cancel out.

The STD is calculated for the difference between the reference and the model data set (equation 39) and measures the spread of the difference around the mean difference. This implies that even with a small STD, the bias can still be high when the variation of the difference is small.

$$STD = \sqrt{\frac{1}{n-1} \cdot \sum_{i=1}^{n} \left([x_i - y_i] - \overline{[x-y]} \right)^2} \tag{39}$$

The RMSE is a criterion describing the deviation of the model data set from the reference data set and is calculated according to equation 18. In contrast to the bias, the RMSE does not cancel out positive and negative errors and since the errors are squared before they are averaged. The RMSE gives a relatively high weight to large errors because of the square operation. For this comparison the RMSE is useful because large errors are particularly undesirable when transport model data should replace reference data as soiling model input. Still, in cases where large outliers occur, the interpretation of the RMSE can become difficult.

While bias, STD and RMSE are negatively-oriented scores (the lower the values, the more accurate the model), the PCC is a positive-oriented value. The PCC is an empirical correlation coefficient, measuring the linear correlation between the reference and the transport model data set. It is calculated according to equation 40. It can take values in the range of -1 to +1, where +1 shows a total positive linear correlation, 0 exhibits no linear correlation and -1 is a total negative linear correlation. It is an important criterion for the data set intercomparison since with a proved linear correlation between a reference and a model parameter this specific parameter can be used in the adapted soiling model with the corresponding conversion factor or offset value [31].

$$PCC = \frac{\sum_{i=1}^{n}(x_i - \overline{x}) \cdot (y_i - \overline{y})}{\sqrt{\sum_{i=1}^{n}(x_i - \overline{x})^2} \cdot \sqrt{\sum_{i=1}^{n}((y_i - \overline{y})^2)}} \tag{40}$$

4.2.1 Intercomparison of NMMB dust model with measurement data

In this subsection, the results of the intercomparison between measured in-situ data and transport model data obtained by the NMMB model are presented and discussed.

The data set from the NMMB model is obtained through spatial interpolation for the locations of the two meteorological stations at PlaSolA and in Missour. Linear interpolation is implemented between four grid cells sized 30 km x 30 km with a weighting of the distance from the exact location to the center of each cell. The available NMMB model values are instantaneous and given every three hours. The internal calculation time of the model is 15 minutes and every six hours the boundary conditions are updated [28]. The data set is referred to as NMMB model data. To ensure a consistent comparison

and to reduce the influence of measured extreme instantaneous values, the DLR measurement data is averaged every three hours over 15 minutes.

In Table 4.1 the statistical evaluation for the analysed parameters is shown. Also for better visualization the different meteorological parameters are plotted over time and scatter plots correlate the modelled with the measured parameters.

Intercomparison shows that the temperatures correlate well with a PCC of 0.60 (PSA) and with a PCC of 0.55 (Missour). The NMMB transport model data underestimates the temperature for PSA (Figure 4.3) and Missour (Figure 4.4) slightly. The seasonal temperature variation is captured well by the transport model as presented in the temperature plots over time. The linear correlation is captured also by the modelled versus the measured temperature in Figure 4.5.

Table 4.1. Comparison of PSA data and Missour data from DLR Meteo Stations and the NMMB Dust model

	parameter	measurement	NMMB modelled	bias	STD	RMSE	PCC
PSA	temperature [°C]	17.35	15.78	1.81	6.88	7.20	0.60
	wind speed [m/s]	3.36	4.78	-1.26	2.87	3.16	0.22
	wind direction [°]	140.14	186.65	-45.67	141.89	149.25	0.24
	relative humidity [%]	55.04	62.87	-7.80	27.05	28.20	0.09
	pressure [hPa]	960.07	947.22	11.99	2.80	12.86	0.88
	PM2.5 [µg/m³]	4.35	2.21	2.08	4.06	4.78	0.26
	PM10 [µg/m³]	8.71	8.75	1.02	16.45	16.49	0.15
	PM20 [µg/m³]	12.91	11.05	2.62	22.17	22.41	0.11
	DLR Soiling [%/day] – NMMB daily total deposition [mg/m²]	-0.33	17.68				- 0.04
	DLR Soiling [%/day] – NMMB daily dry deposition [mg/m²]	-0.33	0.16				- 0.08
	DLR Soiling [%/day] – NMMB daily wet deposition [mg/m²]	-0.33	17.52				- 0.04
MIS	temperature [°C]	18.26	16.15	1.97	8.74	8.97	0.55
	wind speed [m/s]	3.16	3.60	-0.32	2.81	2.83	0.10
	wind direction [°]	154.74	168.86	-14.01	151.25	151.93	0.15
	relative humidity [%]	44.76	58.18	-12.95	31.89	34.59	0.16
	pressure [hPa]	901.34	870.85	28.49	2.21	30.45	0.85
	PM2.5 [µg/m³]	4.10	11.78	-6.23	15.36	16.79	0.35
	PM10 [µg/m³]	10.63	31.97	-15.82	48.43	51.46	0.22
	PM20 [µg/m³]	17.51	36.46	-12.80	58.62	60.29	0.19
	DLR Soiling [%/day] – NMMB daily total deposition [mg/m²]	-0.47	30.33				- 0.09
	DLR Soiling [%/day] – NMMB daily dry deposition [mg/m²]	-0.47	2.15				- 0.05
	DLR Soiling [%/day] – NMMB daily wet deposition [mg/m²]	-0.47	28.18				- 0.09

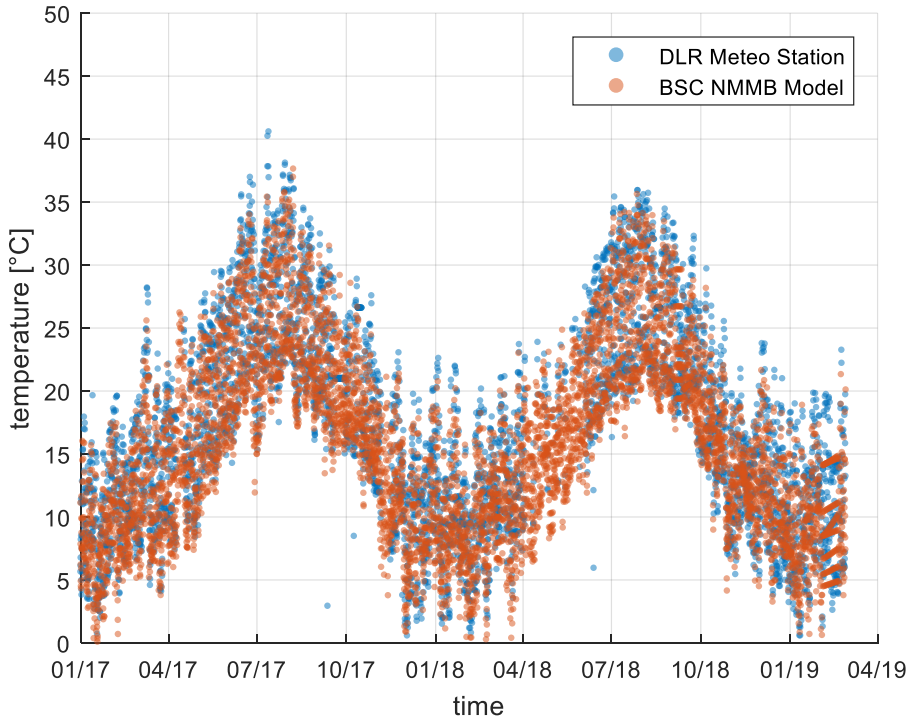

Figure 4.3. Measured and modelled temperature over time at PSA, 01/17 - 03/19

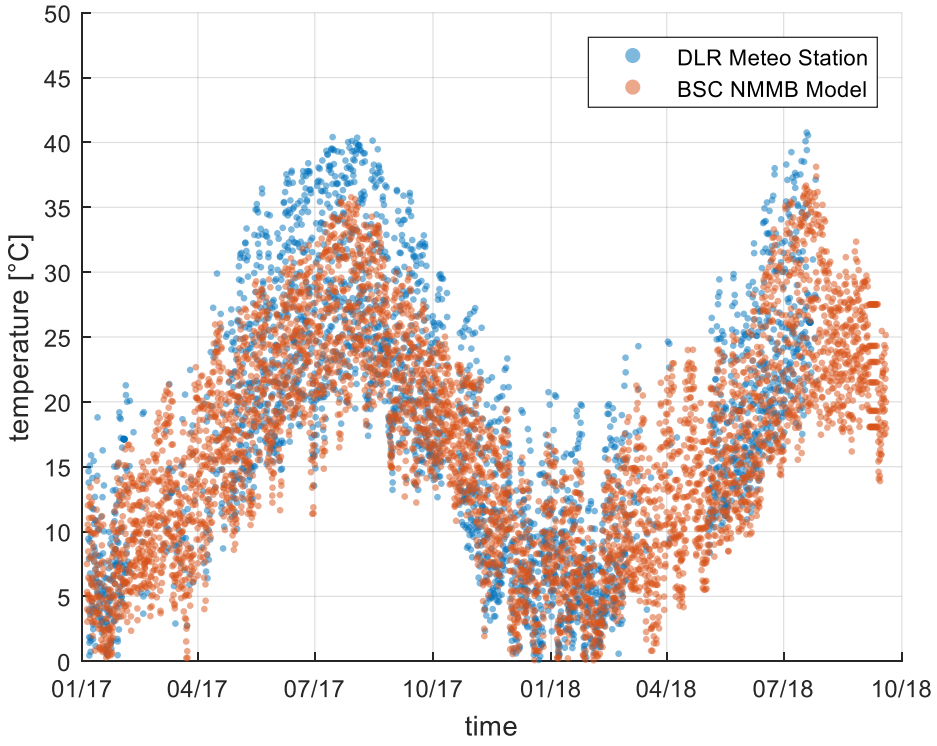

Figure 4.4. Measured and modelled temperature over time in Missour, 01/2017 - 10/2018

The modelled versus measured wind speed is shown in Figure 4.6. A clear linear correlation is not detectable. The NMMB model tends to overestimate the wind speed slightly. The same is valid for the modelled wind direction, plotted in Figure 4.7 over the measured wind direction and in Figure 4.8 over

time. The PCC exhibits an insignificant correlation and the two main wind directions at PlaSolA from South-East and South-West, are not captured well by the NMMB model predictions but instead are slightly shifted. Wind roses of measured and modelled wind direction are shown in Figure 4.9 (PlaSolA) and in Figure 4.10 (Missour).

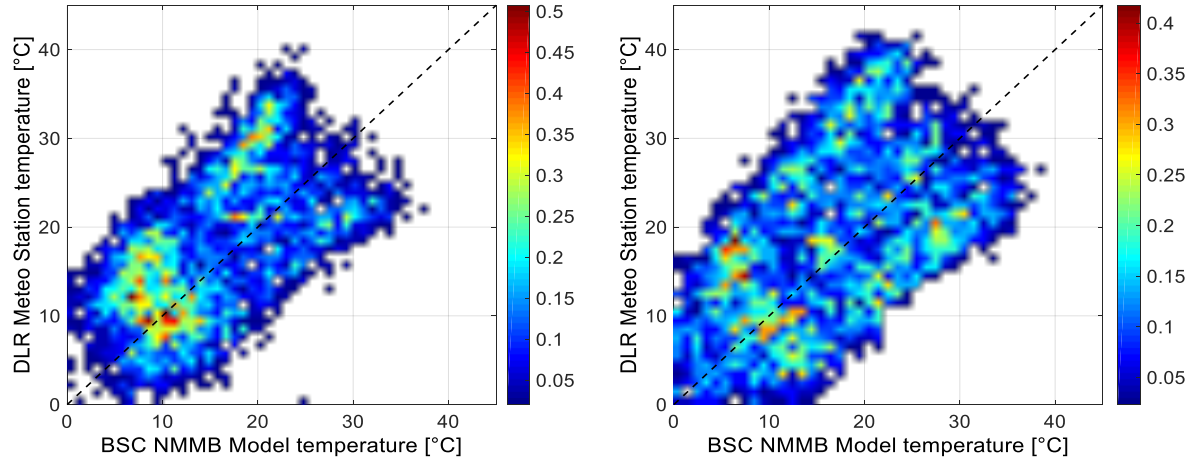

Figure 4.5. Comparison of measured and modelled temperatures at PSA (left) and in Missour (right). The colour bar shows the percentage of data points in one pixel of the total amount of data points.

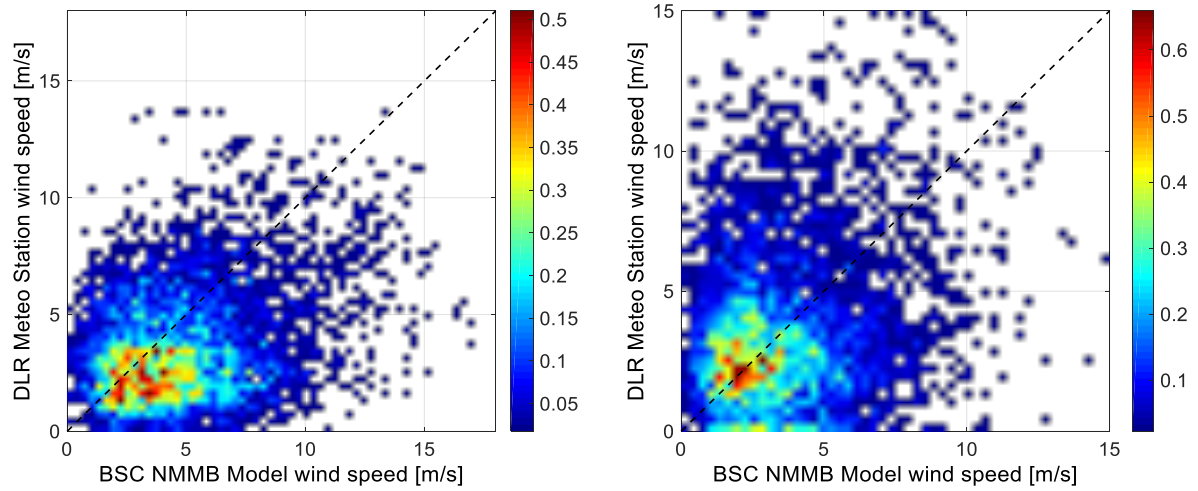

Figure 4.6. Comparison of measured and modelled wind speeds at PSA (left) and in Missour (right)

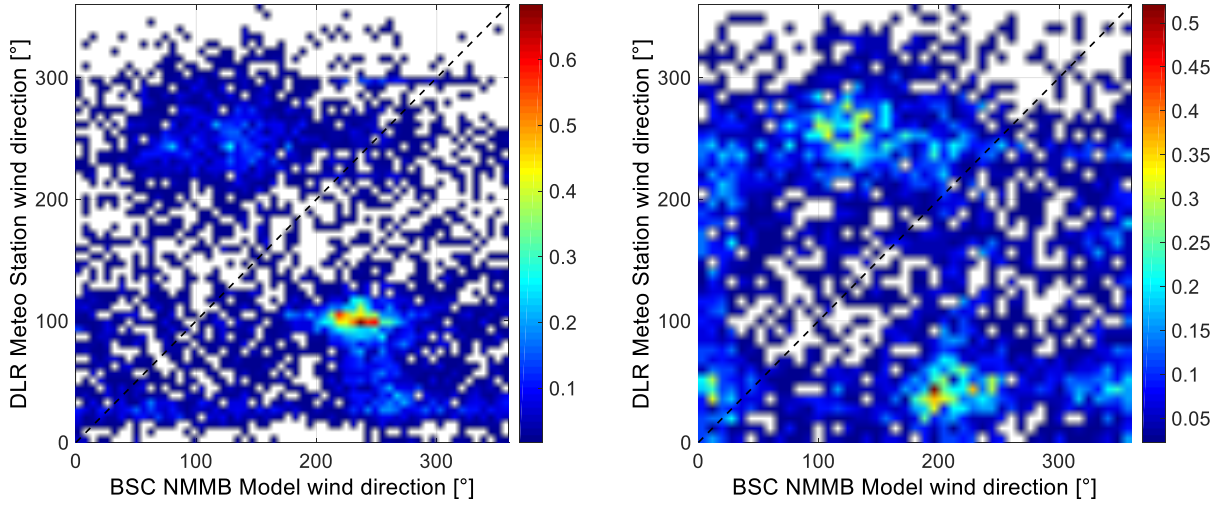

Figure 4.7. Comparison of measured and modelled wind directions at PSA (left) and in Missour (right)

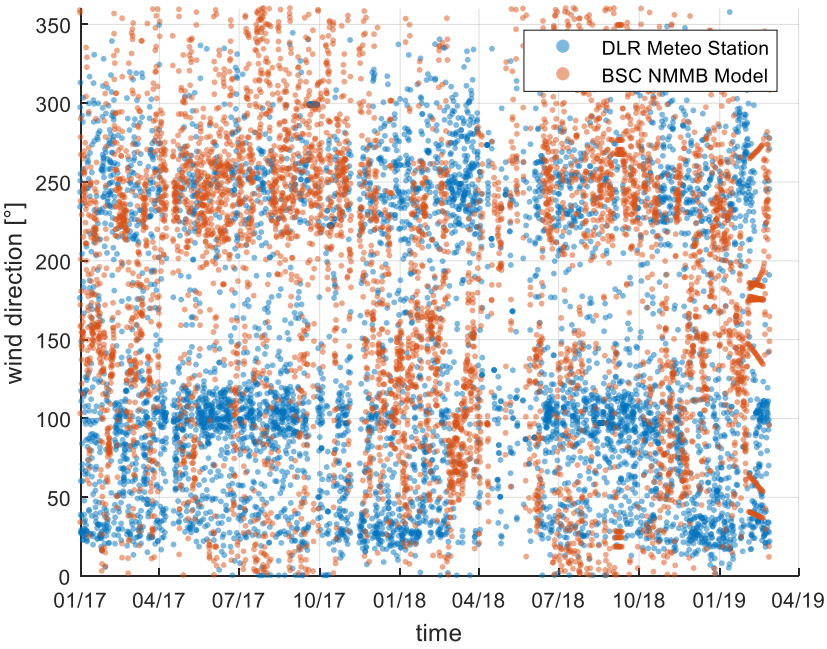

Figure 4.8. Comparison of measured and modelled wind directions over time at PSA, 01/17 - 03/19

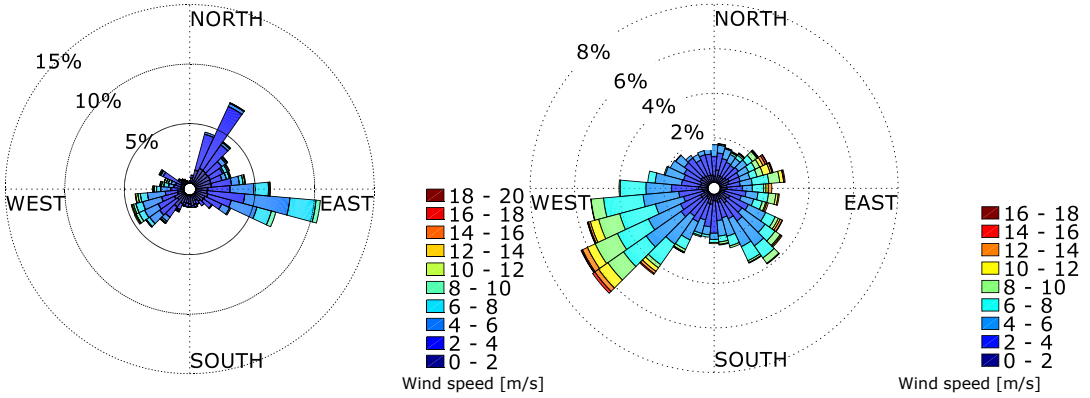

Figure 4.9. Averaged wind roses of measured (left) and modelled wind direction (right) at PSA, 01/17 - 03/19

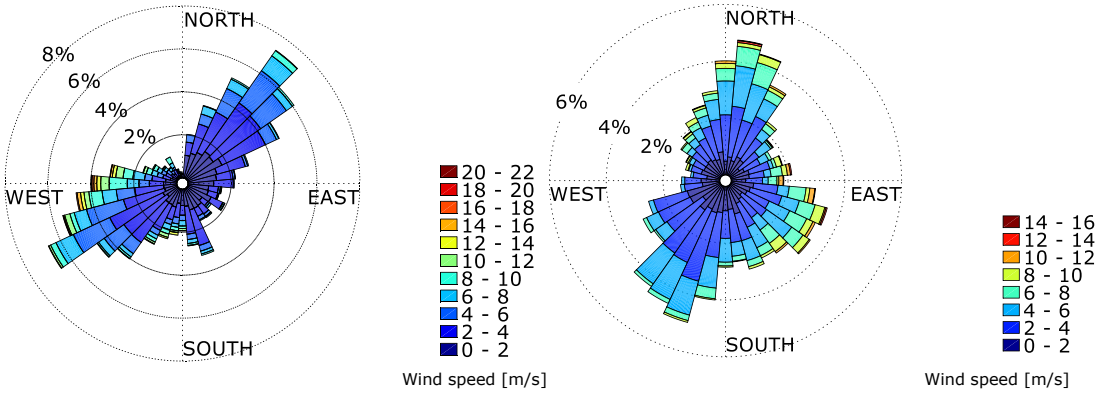

Figure 4.10. Averaged wind roses of measured (left) and modelled wind direction (right) in MIS, 01/17 - 10/18

The mismatch in the modelled and measured wind data both for wind speed and wind direction is distinct. A possible explanation for the discrepancy is the comparably low spatial resolution of the NMMB transport model of 30 km sized grid cells. At both locations, the topographic conditions vary within a few kilometres. The station at PlaSolA (altitude 500 m) is surrounded by mountain chains like the Sierra Alhamilla located within 10 km southwards of PlaSolA, a mountain massif with an altitude of 1200 m. Foothills of Sierra Nevada, mountain chains of around 2000 m, are located in a distance of 10 km towards the north-west of the PlaSolA. The station in Missour is located at an altitude of 1100 m. Mountain chains are not located as close as the mountains surrounding PlaSolA but in less than 30 km distance towards south from the station in Missour foothills of the Haut-Atlas start with altitudes of over 2000 m. Around 10 km towards north-west mountains chains of 1400 m altitude are located. Horizontal linear interpolation of the wind speed and the wind direction over 30 km distances might therefore by inaccurate for the given topographical terrain features which can influence the local wind conditions considerably.

The modelled relative humidity is plotted in Figure 4.11 over the measured relative humidity. The correlation between the NMMB model and DLR measured humidity is less than 16%.

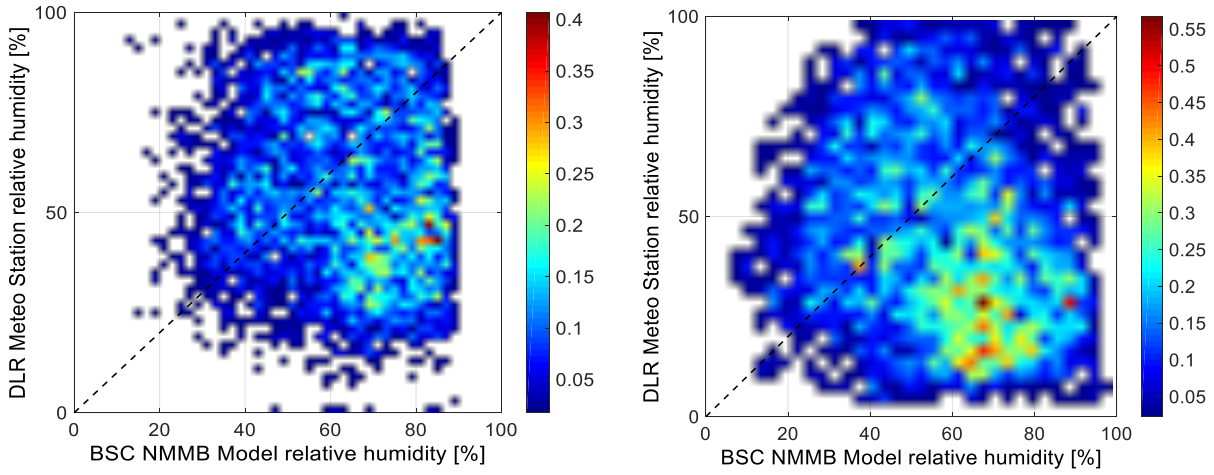

Figure 4.11. Measured and modelled relative humidity at PSA (left) and in Missour (right)

The modelled and measured atmospheric pressure is shown in Figure 4.12 and in Figure 4.13 over time. The correlation between transport model pressure and measured pressure shows PCCs of 0.88 (PlaSolA) and 0.85 (Missour). The linear relation is noticeable in the scattered plots of modelled versus measured pressure in Figure 4.14. The underestimation of the measured pressure is noticeable as a constant offset of around 12 hPa for PlaSolA and around 28 hPa in Missour. The determination of the pressure at the site altitudes works according to the same scheme as the horizontal linear interpolation, it is also implemented vertically. This is why the mountain massifs surrounding both sites closely might be responsible for the offset. Due to the linear correlation of the pressure, its use in the soiling model is possible without difficulties since during parametrization the model fits accordingly and compensates by setting the parameters.

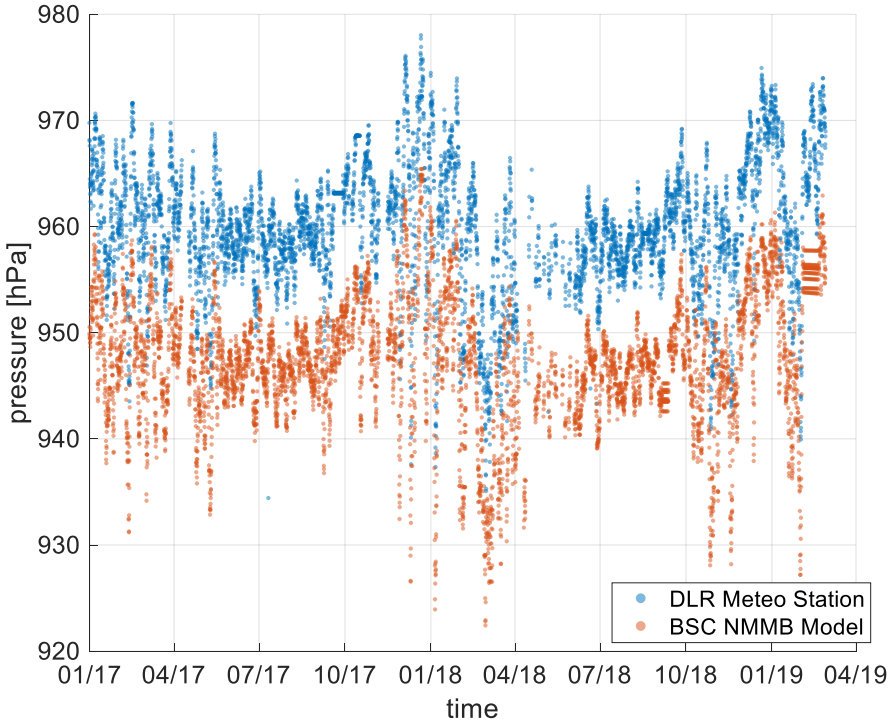

Figure 4.12. Comparison of measured and modelled pressure over time at PSA, 01/17 - 03/19

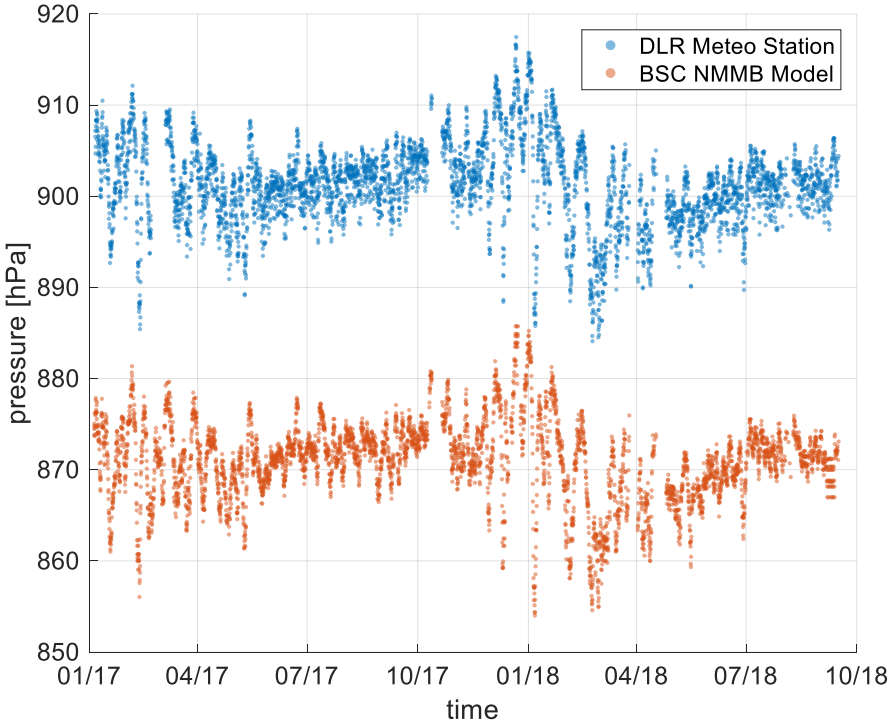

Figure 4.13. Comparison of measured and modelled pressure over time in Missour, 01/17 - 10/18

Aerosol particle concentrations are compared for particulate matter up to particle sizes of 2.5 µm ($PM_{2.5}$ in Figure 4.15), up to 10 µm (PM10 in Figure 4.16), and up to 20 µm diameter (PM_{20} in Figure 4.17). The linear correlation coefficients (PCCs) vary between 0.11 and 0.35, decreasing for

increasing values of PM. At PlaSolA, the transport model underestimates the particle mass concentration, while in Missour higher values than the measured PMs are simulated.

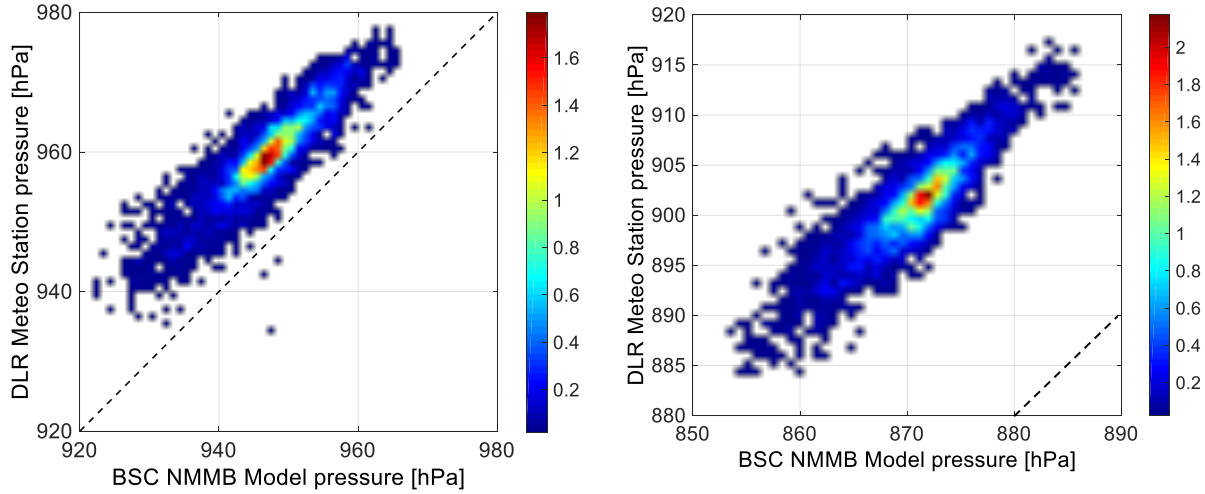

Figure 4.14. Comparison of measured and modelled pressure at PSA (left) and in Missour (right)

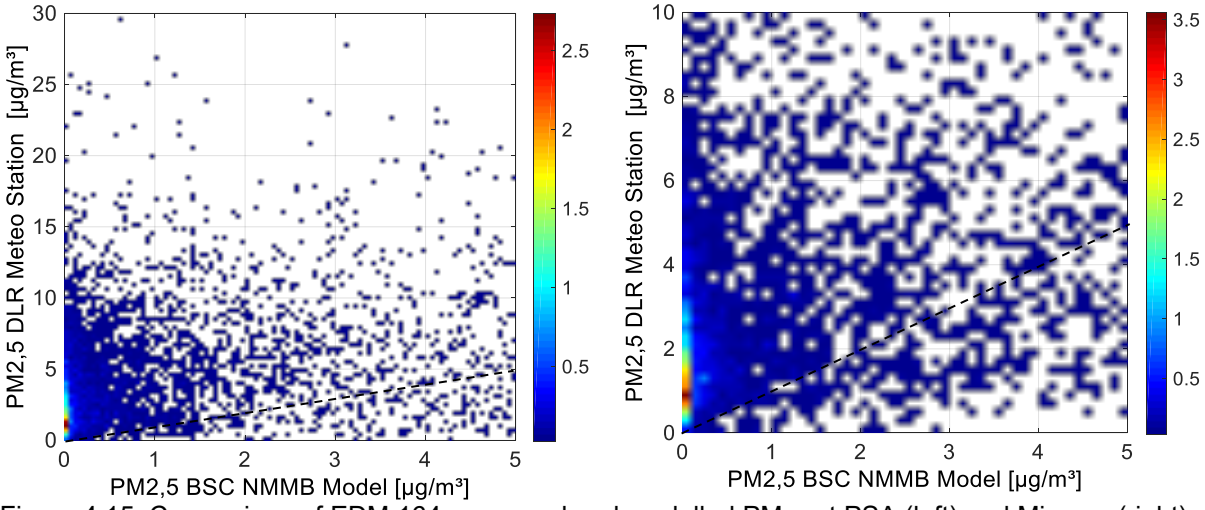

Figure 4.15. Comparison of EDM 164 measured and modelled $PM_{2.5}$ at PSA (left) and Missour (right)

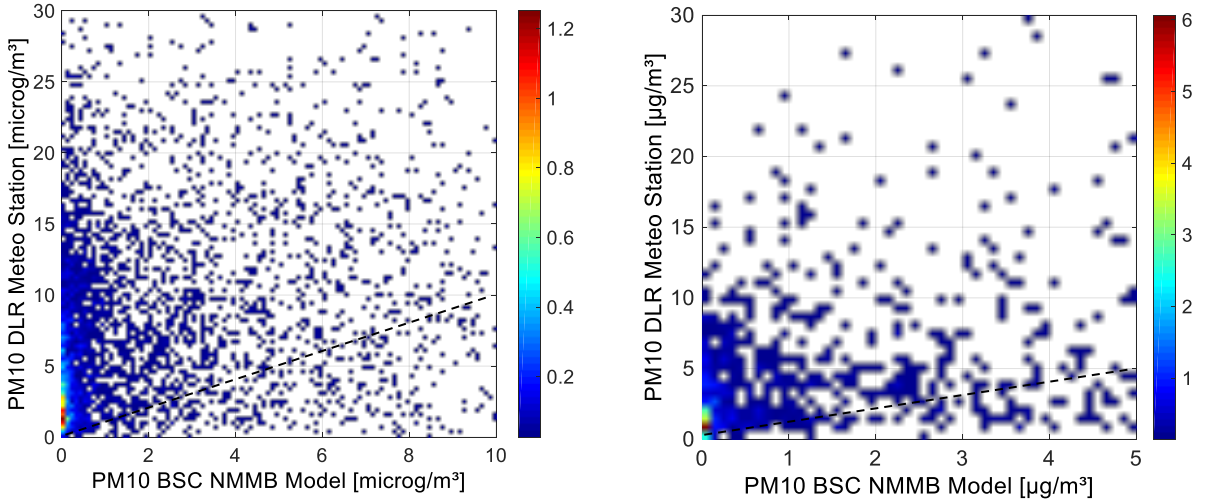

Figure 4.16. Comparison of EDM 164 measured and modelled PM_{10} at PSA (left) and Missour (right)

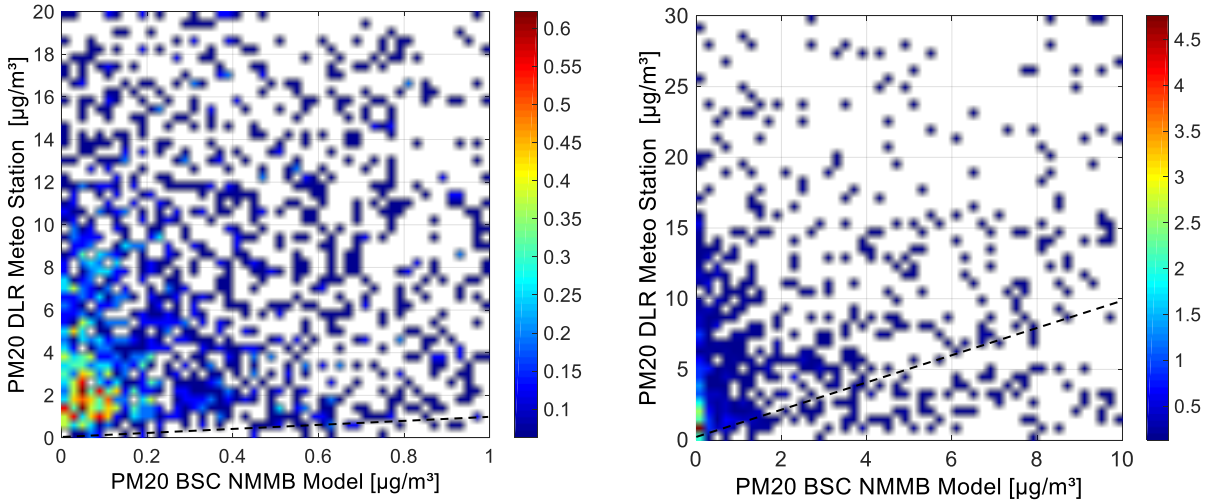

Figure 4.17. Comparison of EDM 164 measured and modelled PM_{20} at PSA (left) and Missour (right)

The NMMB Model only accounts for dust aerosol particles and does not model other aerosol types like sea salt or organic matter, while with the EDM 164 particle counter measurements all aerosol species are counted. This may explain the low correlation of the measured and modelled particle concentrations since sea salt represents a significant part of the aerosol particles at PSA [23].

The correlation between soiling rate and total, dry and wet deposition is also tested for its correlation. The very poor correlation (low PCCs of -0.04 to -0.09) emphasizes the necessity for the soiling model as aerosol deposition model for specifically developed for the application of solar mirrors. Bias, RMSE, and STD are not calculated since they do not have any meaning in this specific comparison due to the different units of the parameters soiling rate and deposition.

It is demonstrated that for some parameters like the temperature and the atmospheric pressure the NMMB transport model can make predictions with an acceptable correlation to the measured values. For other parameters, however, such as wind speed, wind direction, humidity, and particle concentrations, the data does not correlate well with DLR measurements. This may be due to topographical terrain conditions influencing these parameters, situated too closely for the model's spatial resolution to capture their influence. Another factor degrading the correlation between measurement and model is its property of only simulating dust aerosol particles.

4.2.2 Intercomparison of CAMS model with measured data

The CAMS model data obtained by the model reanalysis is compared to measurements recorded at the DLR stations in this section. The CAMS model data is available for the years 2017 and 2018, thus the comparison is implemented for the periods with available DLR measurements for the two years. Statistical evaluation criteria and mean values of the compared and analysed parameters are presented in Table 4.2 followed by graphical presentations of the parameter developments and correlations on the following pages.

Table 4.2. Comparison of PSA data and Missour data from DLR Meteo Stations and the CAMS model, years 2017 and 2018

	parameter	measurements	CAMS modelled	bias	STD	RMSE	PCC
PSA	temperature [°C]	17.59	18.50	-0.92	3.70	3.84	0.89
	wind speed [m/s]	3.34	3.54	-0.10	1.77	1.77	0.47
	wind direction [°]	139.04	144.52	-4.98	99.0	99.12	0.40
	relative humidity [%]	55.17	70.14	-13.77	16.02	22.18	0.63
	pressure [hPa]	960.46	989.54	-26.74	1.01	28.97	0.98
	PM fine [µg/m³]	2.57	8.63	-4.63	4.61	7.47	0.54
	PM medium [µg/m³]	0.85	10.58	-7.36	13.74	16.86	0.06
	PM coarse [µg/m³]	3.45	5.63	-1.58	9.67	9.89	0.00
	DLR Soiling [%] – CAMS total deposition [mg/m²] (daily)	-0.33	2.99				-0.07
	DLR Soiling [%] – CAMS dry deposition [mg/m²] (daily)	-0.33	0.77				0.00
	DLR Soiling [%] – CAMS wet deposition [mg/m²] (daily)	-0.33	2.22				-0.07
MIS	temperature [°C]	18.51	15.93	2.06	3.17	3.88	0.95
	wind speed [m/s]	3.15	2.39	0.77	1.88	2.07	0.32
	wind direction [°]	150.21	164.54	-13.92	145.71	146.57	0.15
	relative humidity [%]	45.07	41.92	3.52	16.35	16.76	0.76
	pressure [hPa]	901.30	840.50	56.40	1.93	60.76	0.88
	PM fine [µg/m³]	1.84	14.44	-6.25	9.93	16.94	0.53
	PM medium [µg/m³]	1.24	18.53	-7.75	20.54	27.04	0.38
	PM coarse [µg/m³]	4.64	23.83	-7.78	38.20	42.25	0.29
	DLR Soiling [%] – CAMS total deposition [mg/m²] (daily)	-0.47	16.36				-0.02
	DLR Soiling [%] – CAMS dry deposition [mg/m²] (daily)	-0.47	14.60				-0.09
	DLR Soiling [%] – CAMS wet deposition [mg/m²] (daily)	-0.47	1.70				-0.08

The temperatures over the time are shown in Figure 4.18 (PlaSolA) and Figure 4.19 (Missour). Modelled and measured temperature correlate well which is also noticeable in the plots of modelled versus measured temperature in Figure 4.20.

The correlation coefficient for the wind speeds of PCC = 0.47 for PSA and PCC = 0.32 for Missour is larger than the correlation with the NMMB Model but the correlating plot for the wind speeds in Figure 4.21 reveals that the relation between modelled and measured wind speed is not linear.

Wind direction correlations are presented in Figure 4.22, the two main wind directions at PlaSolA are captured slightly better as compared to the NMMB model with a PCC of 0.40. The spatial interpolation between grid centres is applied for the grid cell sizes of 80 km in the CAMS model.

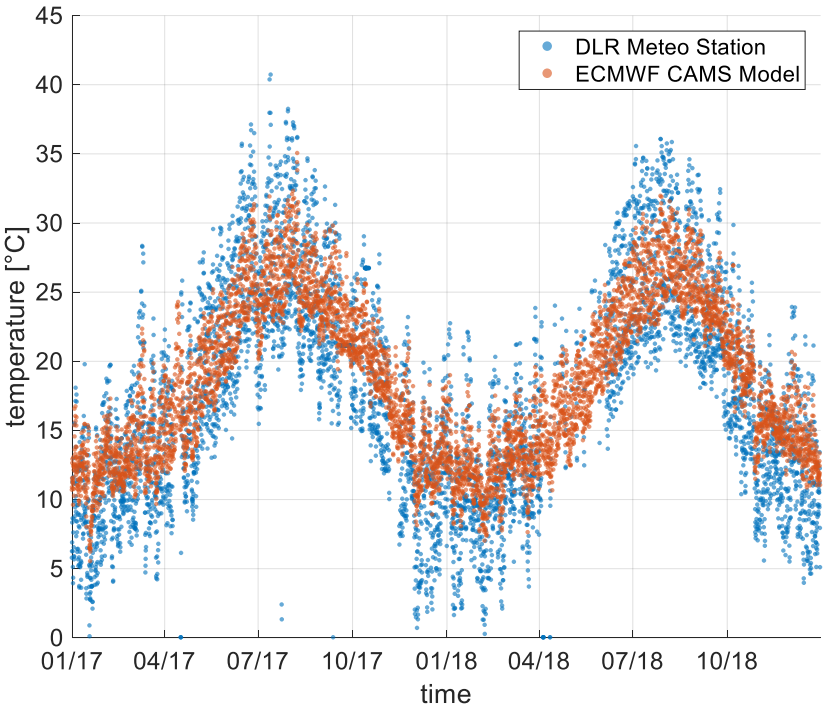

Figure 4.18. Measured and modelled temperature at PSA from January 2017 to December 2018

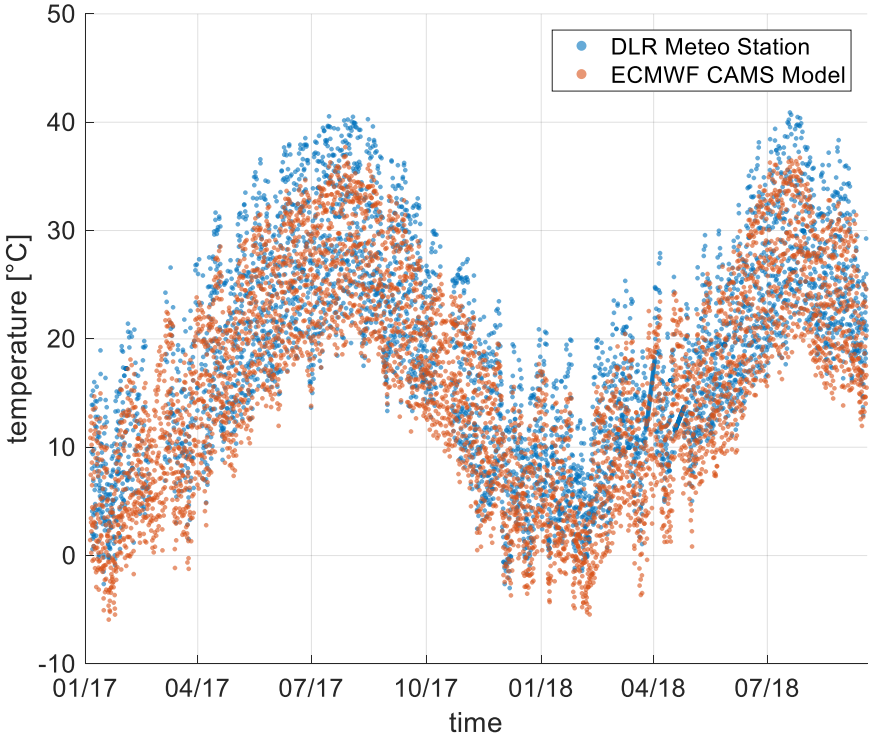

Figure 4.19. Measured and modelled temperature in Missour from January 2017 to September 2018

The CAMS model relative humidity is calculated from temperature, dew temperature, and pressure. Its correlation with the measured relative humidity is shown in Figure 4.23 where an almost linear correlation is recognizable with just a slight underestimation of the humidity at PSA. Correlation coefficients of 0.63 (PSA) and 0.76 (Missour) reflect the linear relation.

The correlation of atmospheric pressure simulated by the CAMS model and of pressure measured at DLR stations is displayed in Figure 4.24. Linear correlations with offsets are recognizable.

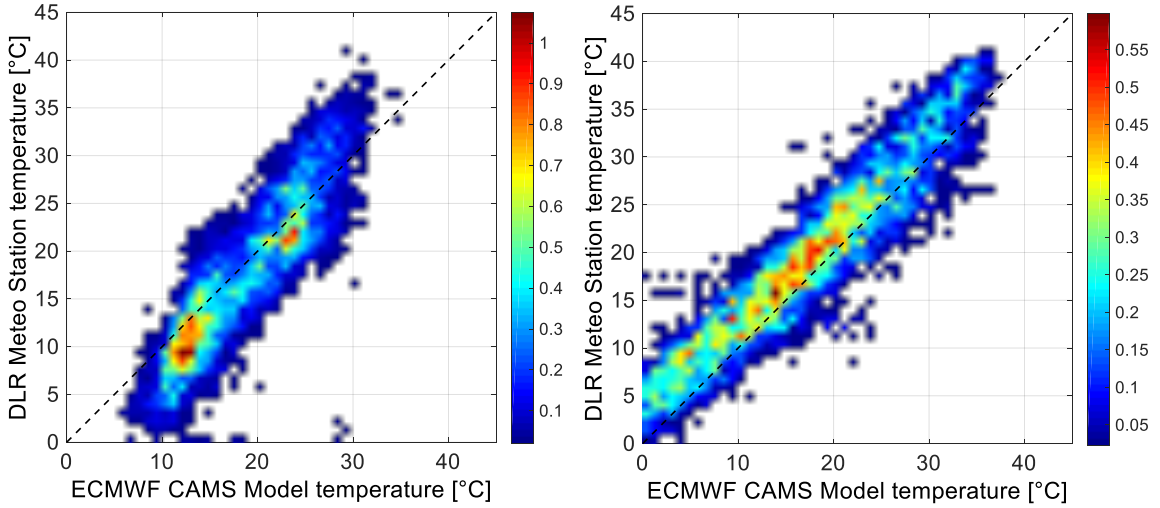

Figure 4.20. Measured and modelled temperature at PSA (left) and in Missour (right)

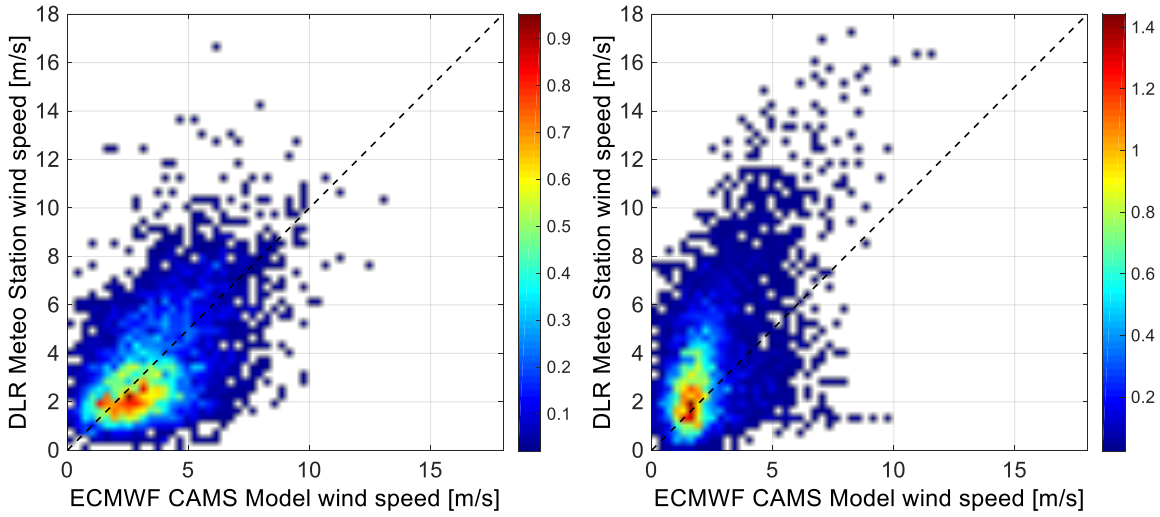

Figure 4.21. Measured and modelled wind speed at PSA (left) and in Missour (right)

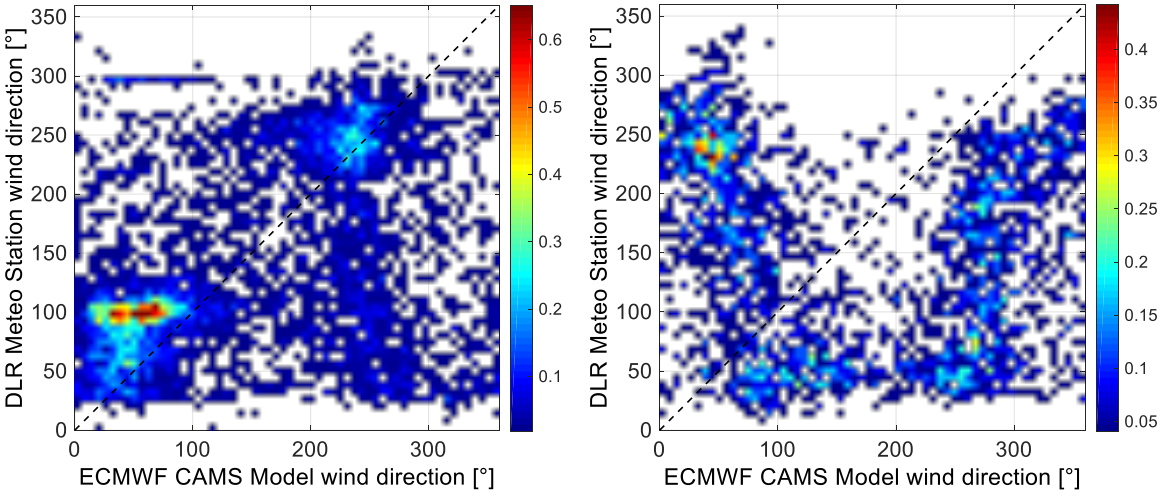

Figure 4.22. Measured and modelled wind direction at PSA (left) and in Missour (right)

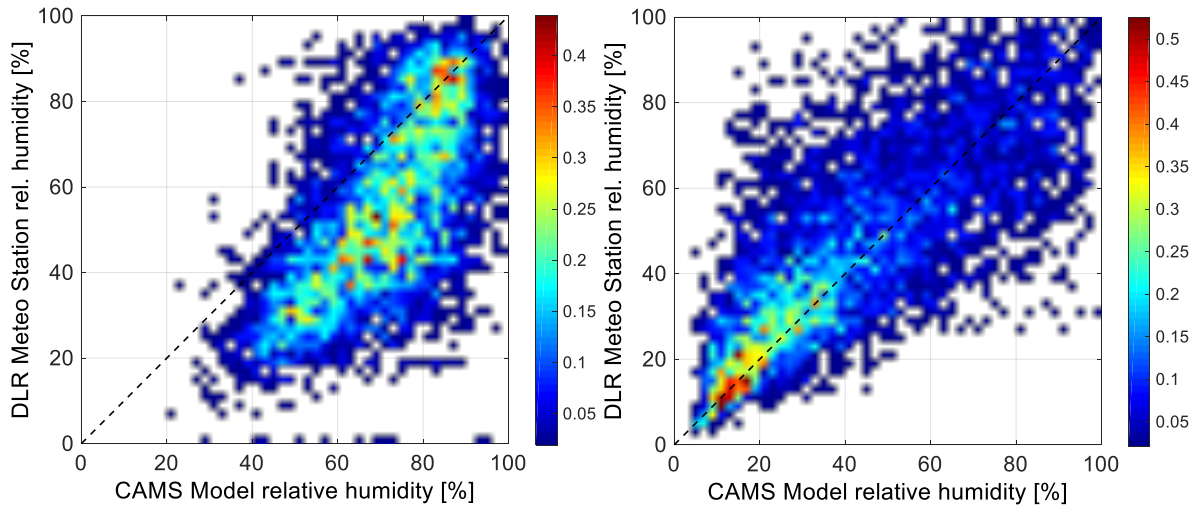

Figure 4.23. Measured and modelled relative humidity at PSA (left) and in Missour (right)

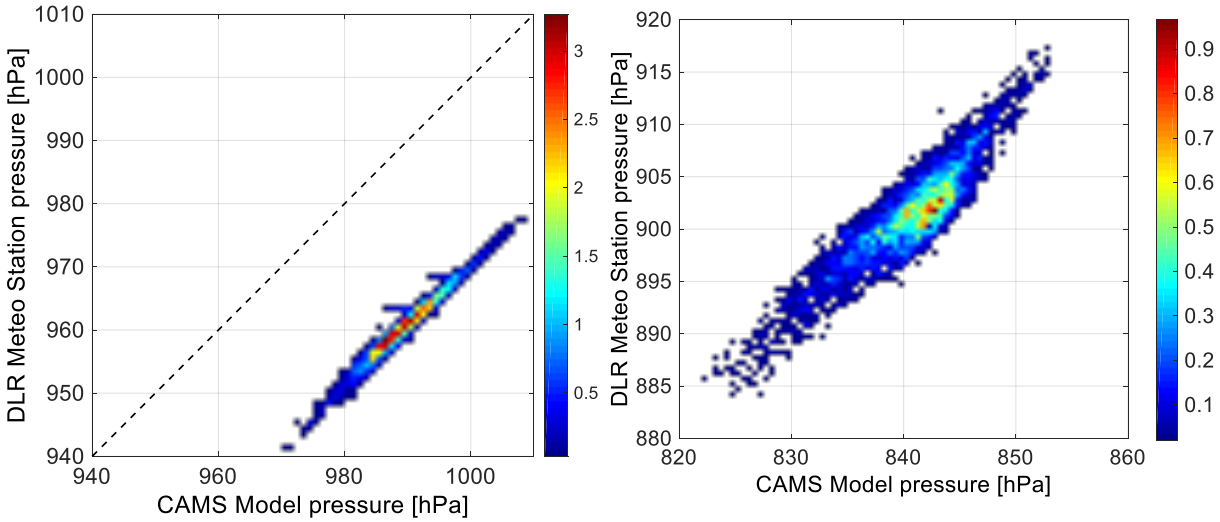

Figure 4.24. Measured and modelled pressure at PSA (left) and in Missour (right)

Aerosol particles are simulated by the CAMS model in 11 aerosol particle species (see Table 2.1) with different bin size limits for each aerosol species. The EDM 164 measurements do not differ between different aerosol species. To compare the particle mass concentrations of transport model and measurement, it is necessary to combine the model aerosol particle estimations for various species into categories of particle size bins. Three bins are created for fine, medium and coarse aerosol particles to classify transport model sea salt and dust aerosol particles. Considering organic matter aerosol particles, most of all particles (85 %) are associated with fine particles with diameters of < 1.5 µm [46]. Black carbon aerosol particles are prevalent mainly as fine particles with diameters < 1 µm [47]. Also sulphate aerosol particles can be considered fine particles in the majority of cases [48]. Therefore in the classification into the three size categories, it is assumed that the aerosol species hydrophilic and hydrophobic organic matter, hydrophilic and hydrophobic black carbon and sulphate are fine. An overview of the categories fine, medium and coarse with associated aerosol species and sizes are presented in Table 2.1.

The share of different aerosol species at PlaSolA obtained by the CAMS model simulation is displayed in Figure 4.25 for the years 2017 and 2018. Almost half of the aerosol particle mass concentration is composed of sea salt aerosol particles, a result of the proximity to the shore (around 30 km distance between PlaSolA and the coastline). Dust aerosol particles constitute nearly a quarter of the total aerosol mass, organic matter aerosol mass is a fifth. This relative importance of sea salt aerosol particles in the total mass mixing ratio was already observed for other transport model simulations and highlights the importance of using a transport model considering salt aerosols [23].

Table 4.3. Bins for the particle concentration comparison; classification into fine, medium and coarse aerosol particles

	fine	**medium**	**coarse**
CAMS	sea salt (0.06 - 1.0)	sea salt (1.0 - 10.0)	sea salt (10.0 - 40.0)
	dust (0.06 - 1.1)	dust (1.1 - 1.8)	dust (1.8 - 40.0)
	hydrophilic organic matter		
	hydrophobic organic matter		
	hydrophilic black carbon		
	hydrophobic black carbon		
	sulphate		
DLR	all species (0.06 - 1.1)	all species (1.1 - 1.8)	all species (1.8 - 20)

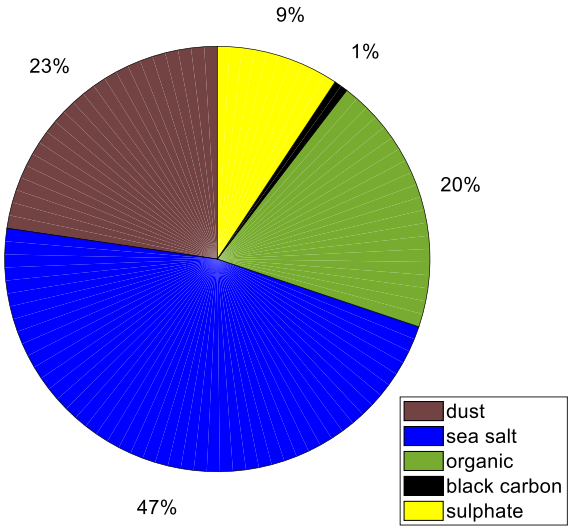

Figure 4.25. CAMS modelled aerosol particle species (average mass concentration shares at PSA during the years 2017 and 2018)

The correlations for the particle mass concentrations are shown in Figure 4.26 for fine, medium and coarse particles. The linear correlation in the category of fine particles is weak but recognizable with a PCC of 0.54 (PlaSolA) and 0.53 (Missour). The particle concentration correlations in Missour follow the same characteristics as the correlations shown for PlaSolA. In all categories, the transport model particle mass concentration overestimates the measured particle concentrations.

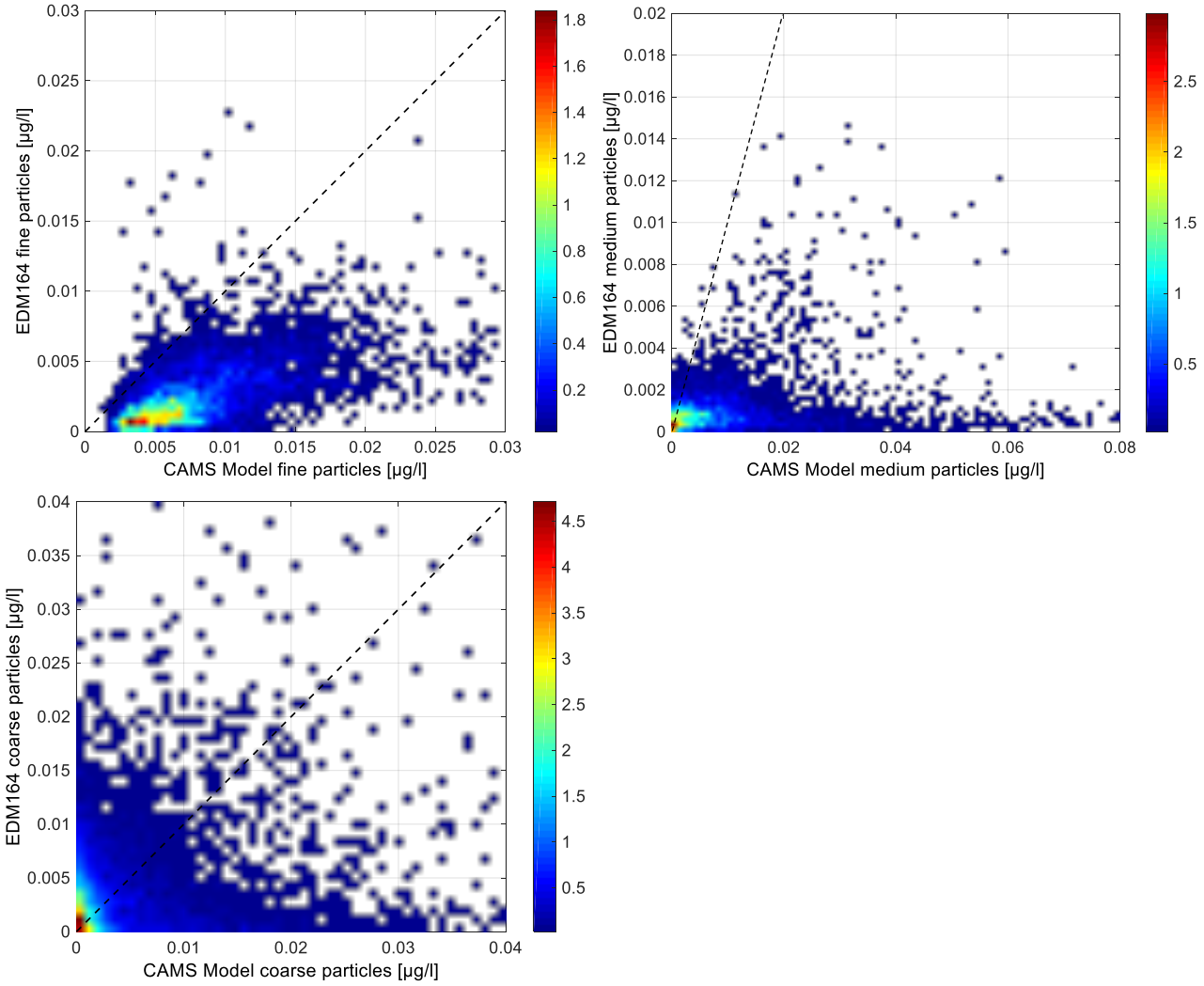

Figure 4.26. Measured and modelled particle mass concentration at PSA, 2017 - 2018

Overall the data provided by the CAMS transport model correlates better with DLR measurements than the data obtained with the NMMB transport model as it is shown in the corresponding intercomparisons. Temperature, pressure and relative humidity correlate almost linearly in the CAMS transport model data. Modelled wind speed and wind direction are in the same range as the recorded values but the linear relation between model and measurement for these parameters is not distinct which might be the result of the spatial model resolution (80 km in CAMS, 30 km in NMMB). The topographical properties at the sites, as mountain chains surrounding the PlaSolA and the mountainous region in Missour, complicate the estimation of wind characteristics with spatial interpolation between grid points.

For the physical deposition mechanisms, the wind characteristics are important parameters. This is why it might be interesting to consult other sources of wind data to obtain more accurate information. Wind maps, wind speed and direction forecasts used for the wind energy industry have spatial resolutions of 2 km that is interpolated to a finer scale. Still, even the best available sources state that the model-derived estimates for wind speeds may not represent the true wind resource at any given location because terrain features, vegetation, buildings, and atmospheric effects may cause the wind speed to differ from the estimates [49].

4.3 Validation results and discussion

The transport model data sets are analysed and compared to the measured data sets. The next step is to use the transport model data as input in the soiling model to determine the soiling rate at the locations. The presentation and discussion of the results are implemented in this section.

The statistical evaluation of the soiling model performance is presented in Table 4.4. Original input data, DLR measurements with one-minute resolution and 30 particle size channels, is taken as a reference performance benchmark to which the performance with transport model data input is compared. Four different cases for transport model input are defined by the two different transport models which are tested (NMMB and CAMS) with each two different particle bin modes. The first tested mode is the three-bin mode which is the originally provided transport model bin number. Secondly the 30-bin mode as result of the artificially created 30 particle size bins is tested (methodology as explained in section 4.1).

The RMSE mean values (red central mark), medians (red line) and variation (50 % of values are inside the blue box, upper and lower quartile limited by grey margin lines) within the five-fold validation are shown for the different input data configurations in Figure 4.27. The variation in the results for the PSA test set is large for each k in the k-fold validation from 1 to 5 since the set is replaced completely whereas validation on the Missour set varies less because the data set remains constant over the five-fold validation, only the parameter set changes. For the performance of the soiling model on the PSA test set with transport model input data (NMMB 3/30, CAMS 3/30) a slight degradation can be observed, but a general trend is not conveyable because of the spreading in the validation process.

Table 4.4. Statistical evaluation scores for the soiling model performance with transport model input, averages, and STDs of the five-fold validation

		RMSE [%/day]	STD_{RMSE} [%/day]	MAD [%/day]	STD_{MAD} [%/day]	bias [%/day]	STD_{bias} [%/day]
PSA Train	**original**	0.547	0.074	0.329	0.051	-0.106	0.058
	NMMB 3 bins	0.593	0.060	0.311	0.042	-0.227	0.045
	NMMB 30 bins	0.600	0.055	0.311	0.042	-0.248	0.026
	CAMS 3 bins	0.566	0.077	0.288	0.050	-0.220	0.061
	CAMS 30 bins	0.605	0.061	0.318	0.042	-0.224	0.046
PSA Test	**original**	0.527	0.298	0.348	0.188	-0.142	0.292
	NMMB 3 bins	0.583	0.284	0.352	0.191	-0.247	0.251
	NMMB 30 bins	0.594	0.312	0.364	0.213	-0.288	0.285
	CAMS 3 bins	0.590	0.348	0.358	0.282	-0.185	0.153
	CAMS 30 bins	0.563	0.301	0.342	0.197	-0.245	0.216
Missour	**original**	0.667	0.011	0.421	0.013	-0.319	0.022
	NMMB 3 bins	1.130	0.117	0.604	0.038	-0.043	0.078
	NMMB 30 bins	0.878	0.178	0.530	0.058	-0.210	0.174
	CAMS 3 bins	0.687	0.004	0.460	0.006	-0.459	0.006
	CAMS 30 bins	0.565	0.002	0.380	0.003	-0.221	0.032

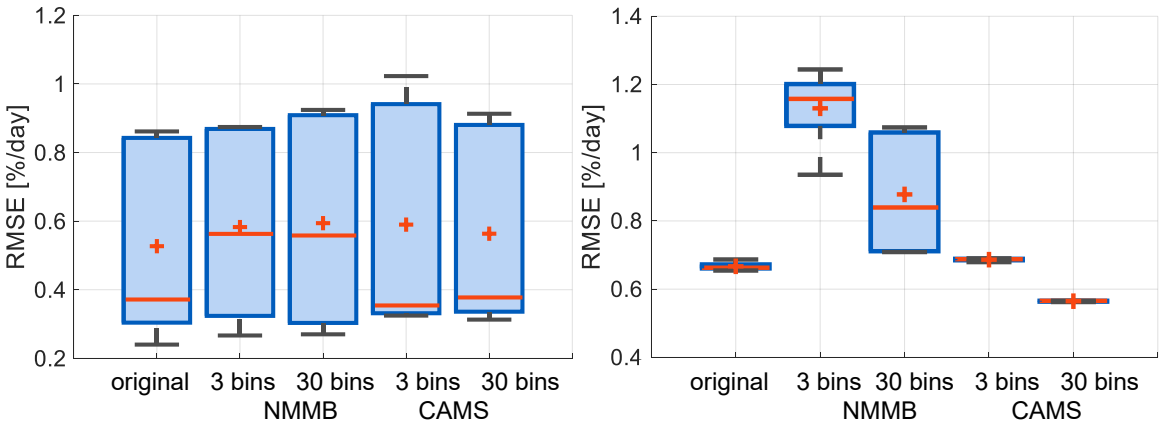

Figure 4.27. RMSE values for 5-fold validation on PSA test set (left) and Missour set (right)

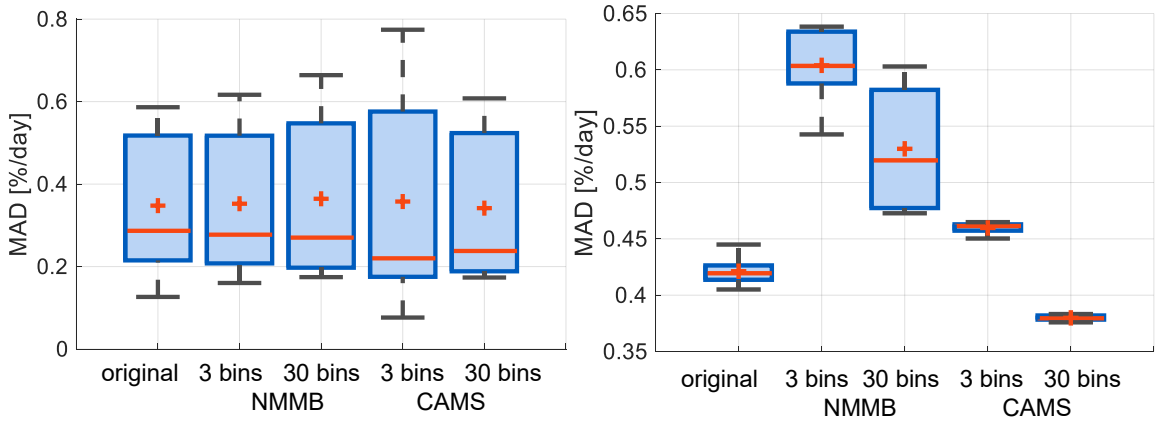

Figure 4.28. MAD values for 5-fold validation on PSA test set (left) and Missour set (right)

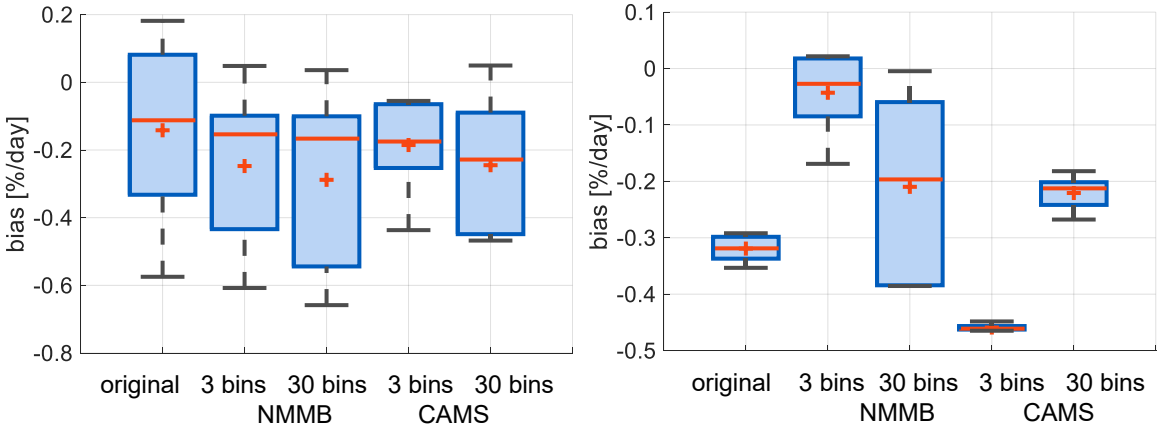

Figure 4.29. Bias values for 5-fold validation on PSA test set (left) and Missour set (right)

For the Missour set, the use of NMMB transport model data results in an increased RMSE. Using the NMMB data input with 3 particle bins increases the RMSE by 50 %. The use of NMMB data with 30 size bins leads to a less increased RMSE. Also for using CAMS transport model input data the 30 particle size bin configuration results in a better soiling model performance than using 3 particle size bins, characterized by an RMSE of about 17 % less.

The absolute deviation between modelled and measured soiling rates for different input data, presented as MAD in Figure 4.28, reveals a similar behaviour. Using NMMB transport model data results in a larger absolute soiling model error while using 30 instead of 3 size bins mitigates the performance degradation and results in a slightly reduced MAD (Missour). A general tendency of the soiling model to underestimate the soiling rate, characterized by a negative bias, is present for original input data and continues if transport model data input is used.

Modelled versus observed soiling rates are shown in Figure 4.30 for PlaSolA. Comparing the modelled soiling rates with NMMB and with CAMS input data to the soiling rates generated with original input data, it is noticeable that CAMS soiling rates are closer to the blue original soiling rate marker points for both 3 and 30 particle size bins. The presentation for Missour in Figure 4.31 shows an underperformance for the CAMS 3 input data and a substantial improvement for using the 30 artificially generated particle size bins. This improvement for switching from 3 to 30 particle bins is also recognizable but not as obvious for NMMB data input.

Histograms in Figure 4.32 show the incidences of modelled soiling rates in bins of 0.05 %/day at PlaSolA. With original input data (minutely with 30 particle bins) the modelled soiling rate ranges between 0.05 %/day and 0.75 %/day. Most of the modelled soiling rates (16 %) are around 0.2 %/day. With the use of transport model input data, the trend moves towards modelling smaller soiling rates and the range of modelled soiling rates shrinks to 0 - 0.6 %/day (NMMB) and to 0 - 0.4 %/day (CAMS).

For Missour, the corresponding histogram plots for modelled soiling rates are shown in Figure 4.33. The same trend towards lower soiling rate predictions can be observed for using transport model input data. The share of very low soiling rates around 0 - 0.1 %/day increases from originally 20 % to 30 % (NMMB) or 55 % and 100 %, the latter value being the most extreme case for the CAMS transport model in the 3 size bins configuration.

The soiling model robustness analysis in subsection 3.3.1 showed that the model performance does not decrease when using original input data converted into 3 particle bins according to CAMS configurations. The reason for the extreme underestimation of the soiling rate thus can rather be justified by the quality of the particle concentration transport model data itself as it is identified in the intercomparison (see 4.2.2). To some extent the lower time resolution of the transport model might be responsible too.

Regarding the four different options for using transport model data as soiling model input while considering the results of the soiling model analysis and the data intercomparison, using the CAMS transport model in the extended 30 particle size bins configuration is the best option. The obtained results are closest to the soiling model performance which can be achieved with original input data. Using NMMB transport model data results in a slightly decreased soiling model performance, characterized by a higher RMSE and higher absolute deviation. The reason for the inferior performance is not the lacking ability of the soiling model to deal with lower temporal resolution or fewer particle size bins as it emerged from the soiling model sensitivity analysis in 3.3. The cause for

the decreased soiling model performance is the low correlation of the data generated by the NMMB transport model as it is discussed in 4.2.1. When using NMMB data, the 30-bin mode also leads to improved performance as compared to the NMMB 3 performance.

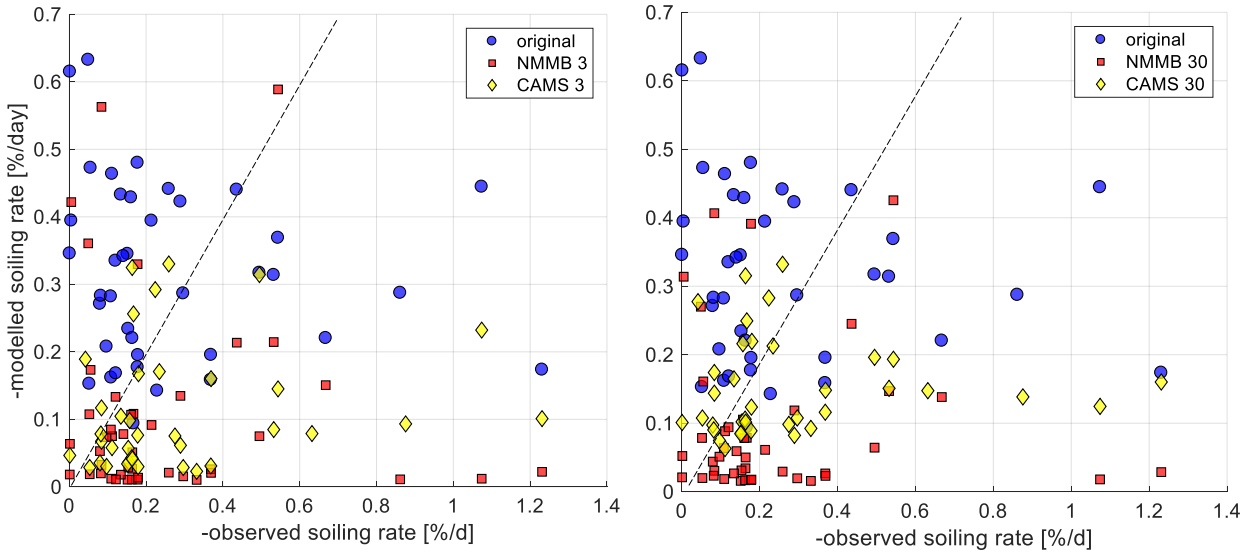

Figure 4.30. Modelled versus measured soiling rate for original DLR input data and transport model input data with 3 bin and 30 bin particle size resolution at PSA, k = 3 (57 days with soiling rate)

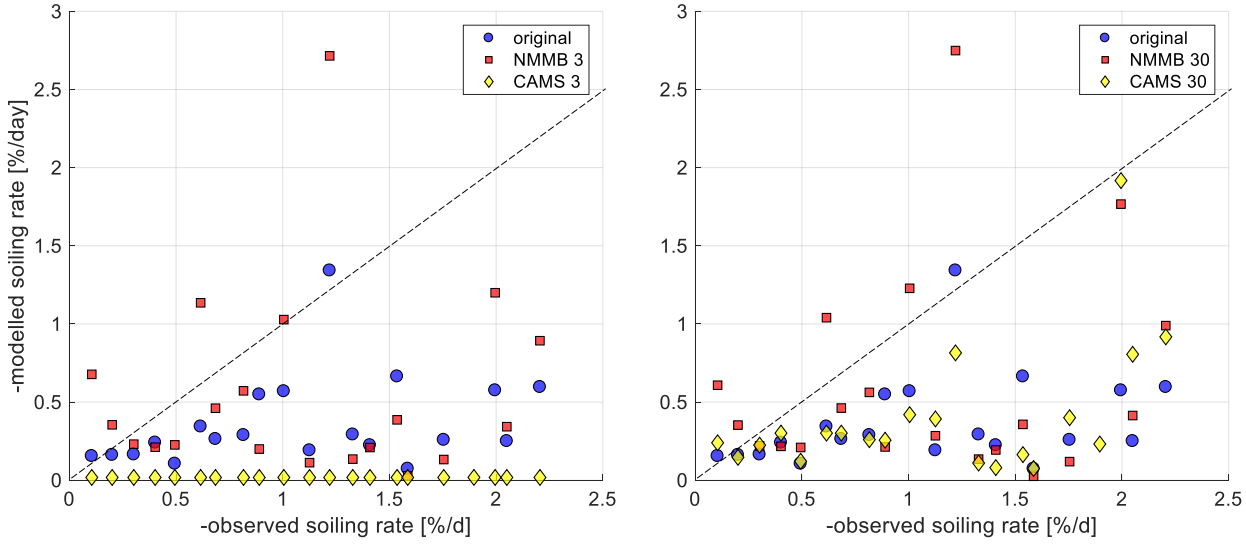

Figure 4.31. Modelled versus measured soiling rate for original DLR input data and transport model input data with 3 bin and 30 bin particle size resolution in MIS, k = 1 (310 days with soiling rate)

This shows that the artificial generation of particle size bins based on the particle size distribution curve of PlaSolA has the potential to solve the problem of the generally low number of size bins provided by aerosol transport models. Applying this method to the CAMS transport model data allows utilizing the full potential of the data. The weaker overall performance of the NMMB model data can be enhanced by it.

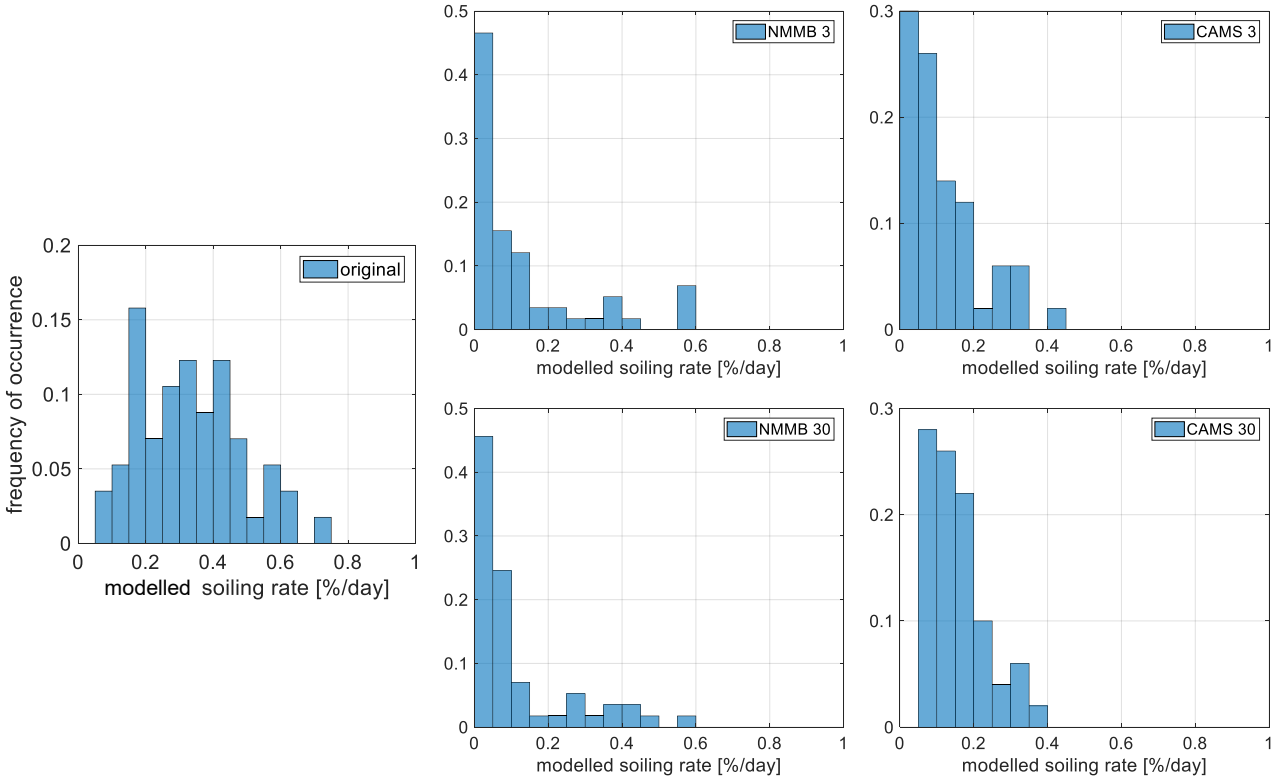

Figure 4.32. Histograms of modelled soiling rates for original soiling model configuration and transport model input data, PSA, k = 3

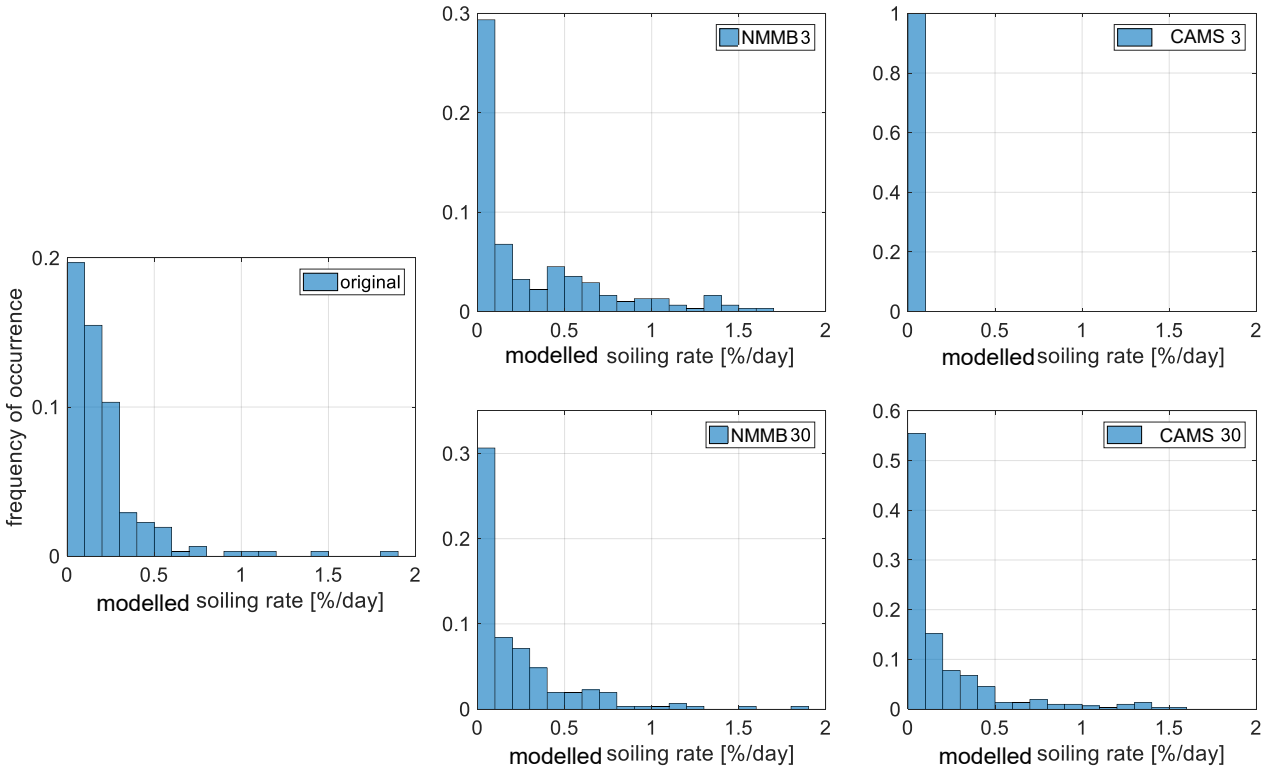

Figure 4.33. Histograms of modelled soiling rates for original soiling model configuration and transport model input data, Missour, k = 5

5 Application of the soiling model to photovoltaics

The soiling model is a simulation tool which is specifically developed for the calculation of soiling rates of CSP mirrors. Particles adhered to the surface of glazing materials – solar reflectors in CSP and transmitting glasses in PV – have a different effect on the performance of each technology (as explained in section 2.1). Still, the deposition mechanisms of aerosol particles work in the same way for both technologies. The relation between projected particle surface coverage and cleanliness is implemented by fitting according to the measured soiling rates (see Figure 2.9), thus with the measured PV soiling rate it is possible to find a linear PV specific relation between the coverage of the PV module's surface and its cleanliness and soiling rate. This is why the soiling model is supposed to apply to PV technology which is tested and validated in this chapter.

The measurements of the PV soiling rate are obtained by comparing the short current circuit of the soiled to the reference PV module as described in subsection 2.4.1. The PV soiling measurement station is located at PlaSolA next to the TraCS device and the meteorological measurements. Cleanliness measurements of the PV modules and the TraCS mirror are shown in Figure 5.1 where the qualitative difference of both technologies is noticeable in the steeper decline of the TraCS cleanliness development curve. PV soiling rates of 240 days ranging from April 2018 to February 2019 are used in the soiling model parametrization and validation which is implemented with five-fold cross validation. The average observed PV soiling rate in the period is -0.071 %/day.

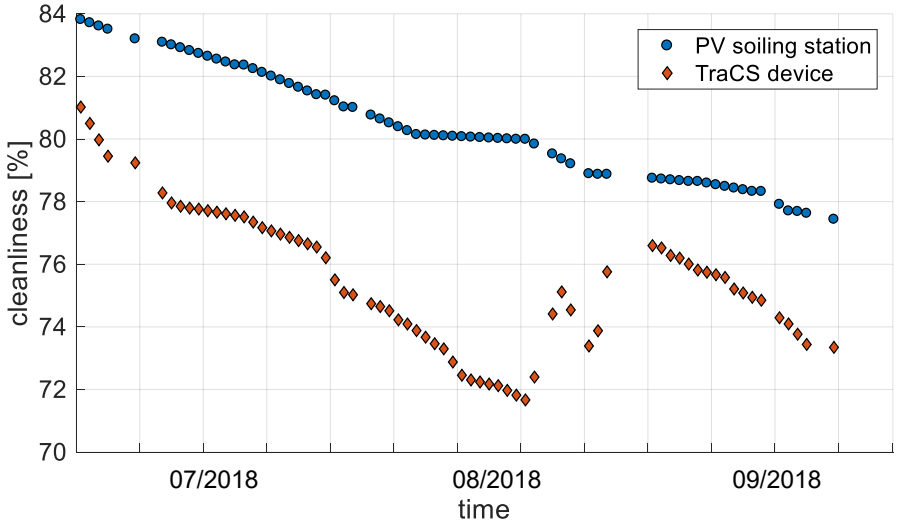

Figure 5.1. Development of cleanliness of PV modules and TraCS mirror at PSA from 07/2018 to 09/2018

The statistical evaluation for the soiling model applied to PV soiling is shown in Table 5.1. The mean RMSE value of the PSA test set is 0.094 %/day which is a relatively large error considering the average PV soiling rate. With an MAD of 0.064 %/day and a bias of -0.042 %/day, the soiling model continues to underestimate the measured soiling rates for the application to PV, as it is already stated

for its application to CSP solar mirrors in section 4.3. Variation of statistical evaluation criteria within the five-fold validation process is shown in Figure 5.2 for the PSA test set.

Table 5.1. Statistical evaluation scores for the soiling model performance applied to photovoltaics with means and STDs for the five-fold validation

data set	RMSE [%/day]	STD_{RMSE} [%/day]	MAD [%/day]	STD_{MAD} [%/day]	bias [%/day]	STD_{bias} [%/day]
PSA train	0.0978	0.0136	0.0584	0.0058	-0.0368	0.0090
PSA test	0.0939	0.0510	0.0638	0.0276	-0.0417	0.0349

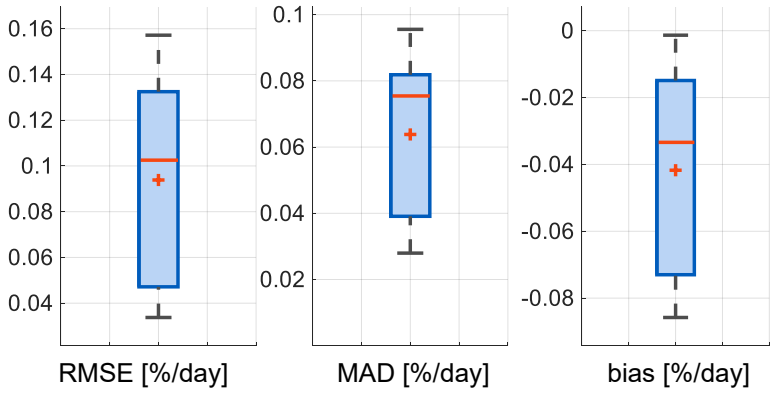

Figure 5.2. Boxplots for statistical values RMSE, MAD and bias with mean (red central mark), median (red line) and variation around the mean for the five-fold validation results of the PSA test set

In Figure 5.3 the modelled PV soiling rates are plotted versus the measured soiling rates of the PV module. Exemplarily four results of the k-fold cross-validation (with k = 5) are presented to show the variation that occurs within the validation process. The test set data is switched chronologically in each step of the validation so that in total 5 different sets of 48 daily soiling rates are used to validate the soiling model. Depending on the selected set, the measured soiling rates vary: in the test set for k = 2 measured PV soiling rates range from 0 %/day to 0.2 %/day, for k = 4 measured daily soiling rates range up to 0.08 %/day.

The modelled soiling rates are generally in the same range as the measured soiling rates, thus it can be conducted that the soiling model can predict the quantitatively lower soiling rates that occur in PV soiling. The discrepancy between modelled and observed soiling rates occur for example when the same soiling rate values are measured multiple times, as for k = 4 the observed soiling rates 0 %/day, 0.018 %/day, 0.052 %/day, and 0.057 %/day. These accumulated observations originate from the post-measuring data processing of the PV soiling rate, which includes manual fitting of the raw cleanliness curves (process explained in 2.4.2). For PV, the cleanliness curve decline is very even and flat so the manual curve fitting is implemented over many days with a linear fit, resulting in a constant soiling rate. The soiling model does not simulate the soiling rates as constant. The observed PV soiling rate distribution is shown in the left histogram in Figure 5.4; the right histogram displays the

distribution of all modelled PV soiling rates, showing the trend of the soiling model for underestimating the PV soiling rate.

The soiling model can be used to predict soiling rates for PV modules with a model performance that is similar to its application on the CSP soiling rate modelling.

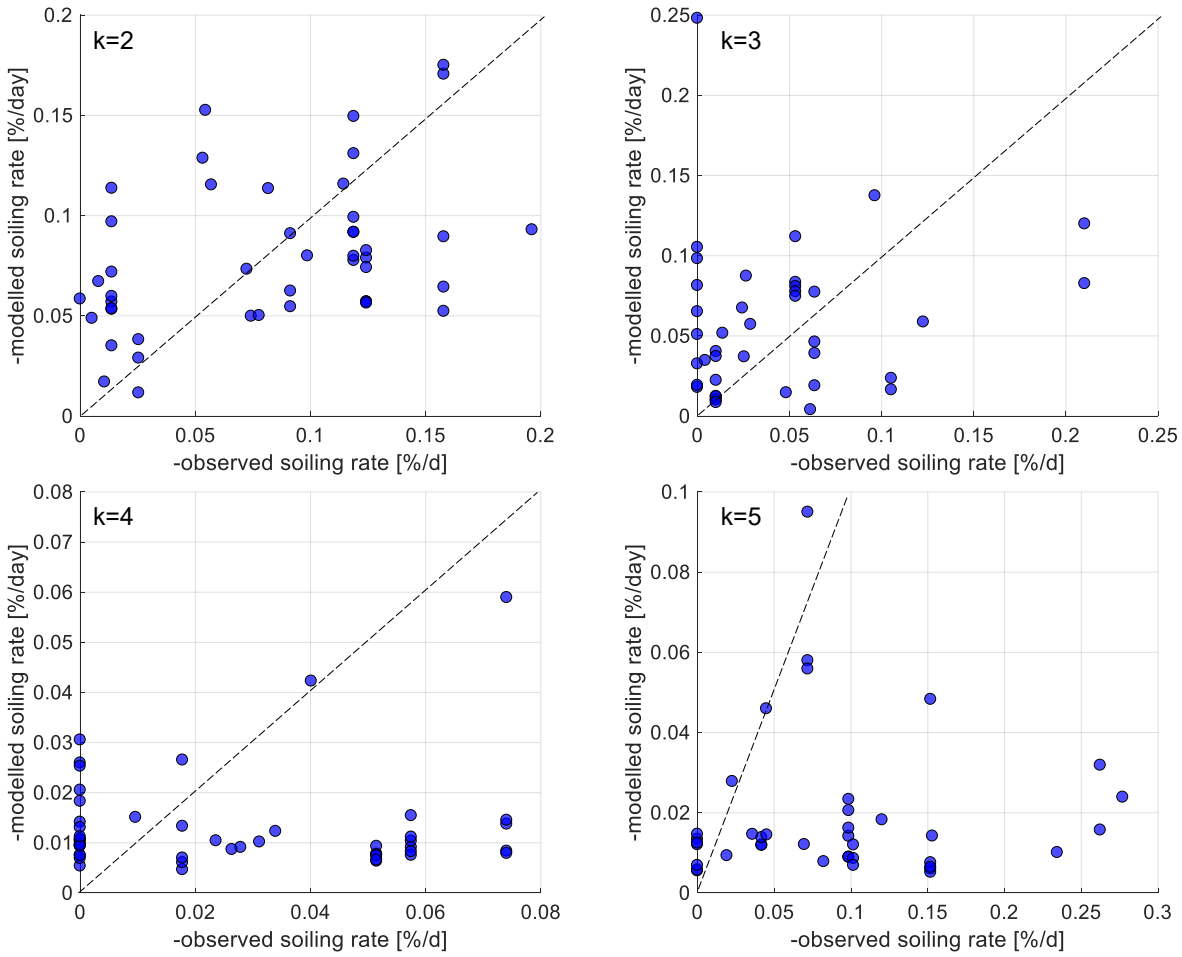

Figure 5.3. Measured versus modelled soiling rate of the PV module at PSA, 04/2018 to 02/2019 for the PSA test set with five-fold cross-validation, results for k = 2…5 (48 days with soiling rates)

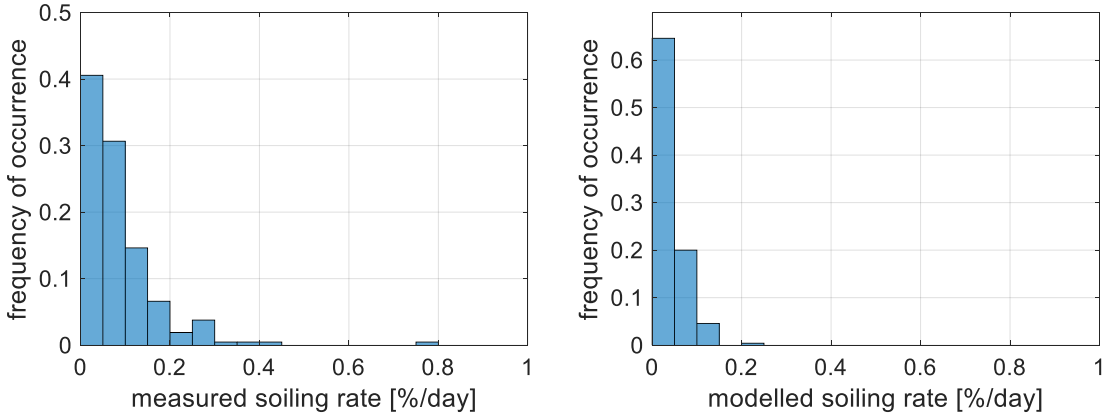

Figure 5.4. Occurrence distribution of measured and modelled PV soiling rates for all available observations (240 days with soiling rates)

6 Conclusion and outlook

The main goal of this thesis is the extension of the soiling model application to various locations by validating the use of aerosol transport model data as soiling model input. Several steps are implemented to follow a gradual process, each providing important results for the final interpretation and future related projects.
The state of the art research shows that there are several alternative approaches to model soiling rates based on combining and interpolating ground measurements to soiling maps and by using GIS and a soiling potential model. The approach to use a soiling model with input data obtained by numerical transport models is a novel approach realized in this master thesis.

The soiling model sensitivity analysis for the soiling model behaviour with adapted in-situ measurement data showed the influence of temporal and particle size input parameter resolution on the soiling model performance. Generally, the occurrence frequency of extreme values for meteorological and aerosol parameters is reduced for averaging over increasing time intervals. While averaging DLR measurements over hourly and 3-hourly time intervals has little impact on the soiling model performance, daily averaging can lead to inaccurately modelled soiling rates. With increasing time intervals, modelling of extreme soiling rates is reduced. Changing the number of particle size bins from 30 to 3 bins or 8 bins leads to a similar range of modelled soiling rates as the original particle size distribution, with exception of the NMMB 3 modification which underestimates the soiling rate considerably.

The comparison of aerosol transport model data to ground measurement data at Plataforma Solar de Almería (Spain) and in Missour (Morocco) shows different results for each investigated model. The NMMB model by BSC makes predictions which correlate well with the measured values for some parameters like the temperature and the atmospheric pressure. For other parameters, however, such as wind speed, wind direction, humidity and particle concentrations ($PM_{2.5}$, PM_{10}, and PM_{20}), the simulated data does not correlate well with DLR measurements. This may be due to topographical terrain conditions influencing these parameters because they are situated too closely for the model's spatial resolution (grid cell sizes of about 30 km) to capture their influence. Another factor degrading the correlation between measurement of $PM_{2.5}$, PM_{10}, and PM_{20} and NMMB modelled particle concentrations might be its property of only simulating dust aerosol particles. With the change from 3 to 8 particle size bins the correlation might improve in the future. The data provided by the CAMS transport model correlates better with DLR measurements. Temperature, pressure and relative humidity correlate almost linearly. Modelled wind speed and wind direction are in the same range as the recorded values but the linear relation between model and measurement for these parameters is not distinct which might again be the result of the spatial model resolution (even less with 80 km grid cells). Topographical properties at the sites, as mountain chains surrounding the PlaSolA and the mountainous region in Missour, complicate the estimation of wind characteristics with spatial interpolation between grid points. This represents a problem for using this data in the soiling model because especially the wind is important to calculate the deposition velocity of aerosol particles and to model the soiling rate (see Figure 2.8) [21].

The performance of the soiling model for the PSA test set with transport model input data slightly decreases, but a general trend is not conveyable because of the variation in the validation results. For the Missour set, using NMMB 3 transport model data results in an about 50 % increased RMSE. The use of NMMB data with 30 size bins leads to a less increased RMSE. Also for using CAMS transport model input data the 30 particle size bin configuration results in a better soiling model performance than using 3 particle size bins. Modelled soiling rates for Missour with CAMS 3 input data underestimate the observed soiling rate but a substantial improvement can be achieved for using the 30 artificially generated particle size bins. A general tendency of the soiling model to underestimate the soiling rate, characterized by a negative bias, is present for original input data and continues if transport model data input is used.

Among the four different options for using transport model data as soiling model input, using the CAMS transport model in the extended 30 particle size bins configuration achieves the best results. The obtained modelled soiling rates are closest to the soiling model performance which can be achieved with original measurement input data.
Using NMMB transport model data results in a slightly decreased soiling model performance with a larger RMSE. The weak correlation of the data generated by the NMMB transport model compared to the ground measurement data is currently a challenge for using this data to model soiling rates. When using NMMB data, the 30-bin mode also leads to improved performance as compared to the NMMB 3 performance. This shows that the novel method for artificial generation of particle size bins based on the particle size distribution curve of PlaSolA has the potential to solve the problem of the generally low number of size bins provided by aerosol transport models. Applying this method to the CAMS transport model data allows utilizing its full potential and enhances the weaker overall performance of the NMMB model data.

The application of the soiling model to PV shows that the soiling model is able to model the quantitatively lower soiling rates that occur in PV soiling. This is especially interesting because PV and CSP continue to coexist and complement each other increasingly in the form of hybrid plants, incorporating the advantages of both technologies. The soiling model can be used to model soiling rates for PV modules with a model performance that is similar to its application on the CSP soiling rate modelling. The discrepancy between modelled and observed soiling rates occur for example when the same soiling rate value is measured multiple times, originating from the post-measuring data processing of the PV soiling rate, which includes manual fitting of the raw cleanliness curves.

The results of this master thesis show that it is generally possible to use transport model data in combination with a soiling model to predict soiling losses. In the future, the utilized transport models should be assessed with regard to which aerosol types their output includes. If more aerosol species are provided within the aerosol transport model output, like in the CAMS model, the soiling model performance is better.
With additional information of eight instead of three particle size bins in the NMMB model a further improvement is probable, especially when the generation of 30 artificial size bins is adapted following the principle introduced in this work.

Regarding the low model-observation correlations of wind characteristics, consulting other sources of wind data as wind maps, wind speed and direction forecasts used by the wind energy industry might be useful to obtain more accurate information.

The next important step is the further improvement of the soiling model. Then, ways to create a soiling map and soiling forecasts based on using aerosol transport model data as input can be pursued. Future research approaches should include methods for processing the large data volume and for automatization at an early stage. The here proven validation of using numerical aerosol transport models – considering also to their performance – as input for the empirical soiling model opens up the possibilities of compiling soiling maps covering comprehensive areas and enables forecasting of soiling rates for exact locations without taking ground measurements.

References

[1] "United Nations Decade for deserts and the fight against desertification," United Nations, [Online]. Available: https://www.un.org/en/events/desertification_decade/whynow.shtml. [Accessed 22 July 2019].

[2] "Electricity Statistics," International Energy Agency, [Online]. Available: https://www.iea.org/statistics/electricity/. [Accessed 20 July 2019].

[3] "Solar Energy," International Energy Agency, 2017. [Online]. Available: https://www.iea.org/topics/renewables/solar/. [Accessed 20 July 2019].

[4] H. Hashem, "CSP research group cut water use by 70 % in desert efficiency drive," New Energy Update by FCBI Energy Ltd., 26 July 2017. [Online]. Available: http://newenergyupdate.com/csp-today/csp-research-groups-cut-water-use-70-desert-efficiency-drive. [Accessed 22 July 2019].

[5] F. Wolfertstetter, S. Wilbert, J. Dersch, S. Dieckmann, R. Pitz-Paal and A. Ghennioui, "Integration of Soiling-Rate Measurements and Cleaning Strategies in Yield Analysis of Parabolic Trough Plants," *Journal of Solar Energy Engineering,* vol. 140, pp. 041008 1-10, 2018.

[6] H. Truong Ba, M. Cholette, R. B. P. Wang and L. Ma, "Optimal Condition-Based Cleaning of Solar Power Collectors," *Solar Energy,* vol. 157, pp. 762-777, 2017.

[7] G. Dünnwald, "Modelling the soiling rate in concentrated solar power plants," RWTH Aachen University, Almería, 2017.

[8] V. Quaschning, Understanding Renewable Energy Systems, New York: Routledge, 2016.

[9] J. A. Duffie and W. A. Beckman, Solar Engineering of Thermal Processes, New Jersey: John Wiley & Sons, 2013.

[10] F. Wolfertstetter, *Effects of Soiling on Concentrating Solar Power Plants,* RWTH Aachen University: Dissertation, 2016.

[11] R. Wagner, T. Ajtai, K. Kandler, K. Lieke and C. Linke, "Complex refractive indices of Saharan dust samples at visible and near UV wavelengths: a laboratory study," *Atmospheric Chemistry and Physics,* vol. 12, pp. 2491-2512, 2012.

[12] P. Bellmann, "Investigation of soiling on mirror and glass samples with regards to power losses in CSP and PV technologies," Technical University Dresden, 2017.

[13] P. Kulkarni, P. A. Baron and K. Willeke, Aerosol Measurement: Principles, Techniques and Applications, John Wiley & Sons, 2011.

[14] O. Boucher, D. Randall, C. Bretherton, G. Feingold and e. al., "Clouds and Aerosols. In: Climate Change 2013: The Physical Science Basis. Contribution of Working Group I to the Fifth Assessment Report of the IPCC," Intergovernmental Panel on Climate Change, Cambridge University Press, 2013.

[15] J. H. Seinfeld and S. N. Pandis, Atmospheric Chemistry and Physics: From Air Pollution to Climate Change, Hoboken, New Jersey: John Wiley & Sons, 2016.

[16] N. Mahowald, S. Albani, J. F. Kok, S. Engelstaeder, R. Scanza, D. S. Ward and M. G. Flanner, "The size distribution of desert dust aerosols and its impact on the Earth system," *Aeolian*

Research, vol. 15, pp. 53-71, 2014.

[17] I. Tegen, P. Hollrig, M. Chin and I. Fung, "Contribution of different aerosol species to the global aerosol extinction optical thickness: Estimates from model results," *Journal of Geophysical Research,* vol. 102, pp. 23,895-23,915, 1997.

[18] Y. Ben-Ami, I. Koren and Y. Rudich, "Transport of Saharan dust from the Bodélé Depression to the Amazon Basin: a case study," *Atmospheric Chemistry and Physics,* 2010.

[19] F. Wagner, D. Bortoli, S. Pereira, B. Heinold and I. Tegen, "Properties of dust aerosol particles transported to Portugal from the Sahara desert," *Tellus B: Chemical and Physical Meteorology,* vol. 61B, pp. 197-306, 2009.

[20] J. Stuut and M. Prins, "The significance of particle size of long-range transported mineral dust," *Past Global Changes Magazine,* vol. 2, p. 70 f., 2014.

[21] F. Wolfertstetter, C. Sansom, P. King, S. Wilbert and A. Fernandez García, "Water Saving for Solar Concentrated Power: Soiling and condensation model applied to CSP solar field," DLR, 2018.

[22] "GRIMM Aerosol Technik Portable Laser Aerosolspectrometer and Dust Monitor Model 1.108/1.109," 2010. [Online]. Available: https://www.wmo-gaw-wcc-aerosol-physics.org/files/opc-grimm-model--1.108-and-1.109.pdf. [Accessed 3 May 2019].

[23] N. M. Hanrieder, *Determination of Atmospheric Extinction for Solar Tower Plants,* RWTH Aachen University: Dissertation, 2016.

[24] "Thies Wind Anemometer Technical Specifications," Thies Clima, [Online]. Available: https://www.thiesclima.com/de/Produkte/Wind-First-Class/. [Accessed 25 July 2019].

[25] "Technical Specifications of the 110PV Temperature Sensor," Campbell Scientific, [Online]. Available: https://www.campbellsci.de/110pv. [Accessed 25 July 2019].

[26] J. Hendricks, V. Aquila and M. Righi, "Global Atmospheric Aerosol Modeling," NASA Goddard Space Flight Center, Greenbelt, MD, United States, 2012.

[27] "Barcelona Dust Forecast Center," Agencia Estatal de Meteorología (AEMET) - BSC, [Online]. Available: https://dust.aemet.es/forecast. [Accessed 26 July 2019].

[28] BSC, "BSC Dust Daily Forecast - Model Description NMMB/BSC-Dust," [Online]. Available: https://www.bsc.es/projects/earthscience/visor/bases_datos/image_viewer/docs/NMMB_BSC_model_description.pdf. [Accessed 13 July 2019].

[29] C. Pérez, K. Haustein, Z. Janjic and O. Jorba, "Atmospheric dust modeling from meso to global scales with the online NMMB/BSC-Dust model - Part 1: Model description, annual simulations and evaluation," *Atmospheric Chemistry and Physics,* pp. 13001-13027, 2011.

[30] "Particulate Matter (PM) Pollution," United States Environmental Protection Agency, [Online]. Available: https://www.epa.gov/pm-pollution/particulate-matter-pm-basics. [Accessed 25 July 2019].

[31] E. Terradellas, S. Basart, F. Benincasa and M. Baldasano, "Model-Intercomparison and Evaluation of Dust Forecasts," Regional Center for Northern Africa, Middle East and Europe of the WMO SDS-WAS, Barcelona, 2018.

[32] F. Benincasa, "Model evaluation metrics - Annual scores," WMO Sand and Dust Storm Warning Advisory and Assessment System, 27 November 2014. [Online]. Available:

https://sds-was.aemet.es/forecast-products/forecast-evaluation/model-evaluation-metrics/model-evaluation-metrics-annual?date=201801-201812. [Accessed 13 July 2019].

[33] "AERONET - Aerosol Robotic Network," NASA Goddard Space Flight Center, 23 July 2019. [Online]. Available: https://aeronet.gsfc.nasa.gov/. [Accessed 26 July 2019].

[34] A. Bozzo, S. Remy, A. Benedetti, J. Flemming and P. Bechtold, "Implementation of a CAMS-based aerosol climatology in the IFS," European Center for Medium-Range Weather Forecasts, Reading, England, 2017.

[35] A. Benedetti, J. Morcrette, O. Boucher and A. Dethof, "Aerosol analysis and forecast in the ECMWF Integrated Forecast System: Data assimilation," European Centre for Medium-Range Weather Forecasts, Reading, England, 2008.

[36] A. Benedetti, J. Morcrette, O. Boucher and A. Dethof, "Aerosol analysis and forecast in the European Center for Medium-Range Weather Forecasts Integrated Forecast System: 2. Data assimilation," *Journal of Geophysical research,* vol. 114, p. D13205, 2009.

[37] L. Micheli, M. Deceglie and M. Muller, "Mapping Photovoltaic Soiling Using Spatial Interpolation Techniques," *IEEE Journal of Photovoltaics,* 2018.

[38] "NCPRE - SERIIUS Site Rates of the World," Indian Institute of Technology Bombay, 8 August 2018. [Online]. Available: http://www.ncpre.iitb.ac.in/ncpre/pages/SERIIUS_Soiling_rate_of_the_World.html. [Accessed 22 July 2019].

[39] C. Kost, S. Shammugam, V. Jülch, H. Nguyen and T. Schlegl, "Levelized cost of electricity - Renewable energy technologies," Fraunhofer Institute for Solar Energy Systems ISE, Freiburg, 2018.

[40] L. Micheli and M. Muller, "An investigation of the key parameters for predicting PV soiling losses," *Progress in Photovoltaics: Research and Applications,* vol. 25, pp. 291-307, 2017.

[41] H. Capdevila, V. Naidoo and M. Graeber, "Soiling forecast and measurements for large PV power generation projects in desert environments," in *IEEE 43rd Photovoltaic Specialists Conference (PVSC)*, Portland, 2016.

[42] "Photovoltaic Module Soiling Map," National Center for Photovoltaics (NCPV) - National Renewable Energy Laboratory (NREL), [Online]. Available: https://www.nrel.gov/pv/soiling.html. [Accessed 25 July 2019].

[43] J. John, "Photovoltaic Modules and Development of a Novel Cleaning System," Indian Institute of Technology, Bombay, 2015.

[44] J. Herrmann, K. Slamova, R. Glaser and M. Köhl, "Modeling the soiling of glazing materials in arid regions with geographic information systems (GIS)," in *International Conference on Solar Heating and Cooling for Buildings and Industry*, Freiburg, 2013.

[45] C. Pérez, S. Nickovic, J. Baldasano and E. Özsoy, "Interactive dust-radiation modeling: A step to improve weather forecasts," *Journal of Geophysical Research Atmospheres,* vol. 111, 2006.

[46] I. G. Kavouras und E. G. Stephanou, „Particle Size distribution of organic primary and secondary aerosol constituents in urban, background marine, and forest atmosphere,“ *Journal of Geophysical Research,* Bd. 107, Nr. D8, pp. AAC 7-1-AAC 7-12, 2002.

[47] J. Viidanoja, K. Veli-Matti and R. Hillamo, "Measuring the Size Distribution of Atmospheric

Organic and Black Carbon Using Impactor Sampling Coupled with Thermal Carbon Analysis: Method Development and Uncertainties," *Aerosol Science & Technology,* vol. 36, pp. 607-616, 2002.

[48] X. Ma and K. von Salzen, "Dynamics of the sulphate aerosol size distribution on a global scale," *Journal of Geophysical Research,* vol. 111, p. D08206, 2006.

[49] WINDExchange U.S. Department of Energy, "U.S. Average Annual Wind Speed at 30 Meters," National Renewable Energy Laboratory, 21 Feb 2012. [Online]. Available: https://windexchange.energy.gov/maps-data?utf8=%E2%9C%93&search=resolution. [Accessed 20 Jun 2019].

[50] F. Li, A. M. Vogelmann and V. Ramanathan, "Saharan Dust Aerosol Radiative Forcing Measured from Space," *Journal of Climate,* vol. 17, pp. 2558-2571, 2004.

Appendix A

Table A.1. EDM 164 size channel specification and weighting factors for particle mass calculation, volume concentration for PSA 01/2017-03/2019

Size channel *i*	Lower diameter [µm]	Upper diameter [µm]	Medium (effective) diameter $d_{eff,i}$ [µm]	Average volume concentration $\overline{n_{v_i}}$ [µm³/l]	w_i
1	0.25	0.265	0.2575	0.472981898815407	0.117404887857779
2	0.265	0.29	0.2775	0.344874139476445	0.0856056220580277
3	0.29	0.325	0.3075	0.260014623224756	0.0645415559401757
4	0.325	0.375	0.35	0.211116181005497	0.0524038480499786
5	0.375	0.425	0.4	0.150395509170261	0.0373315933076314
6	0.425	0.475	0.45	0.133534880575796	0.0331464009899072
7	0.475	0.54	0.5075	0.148346773535233	0.0368230504266394
8	0.54	0.615	0.5775	0.139978350612128	0.0347458171175122
9	0.615	0.675	0.645	0.144551807250292	0.0358810532968899
10	0.675	0.75	0.7125	0.161954009000854	0.0402006764159144
11	0.75	0.9	0.825	0.188454630822952	0.0467787347749703
12	0.9	1.15	1.025	0.259755663380464	0.0644772762044079
13	1.15	1.45	1.3	0.338654003046983	0.0840616424220414
14	1.45	1.8	1.625	0.480898616172844	0.119369997549882
15	1.8	2.25	2.025	0.593127818521662	0.147227843588243
16	2.25	2.75	2.5	0.673978591066314	0.0473161415606072
17	2.75	3.25	3	0.673236676380149	0.0472640560184523
18	3.25	3.75	3.5	0.735374156981651	0.0516263694024851
19	3.75	4.5	4.125	0.844579018777223	0.0592930115901113
20	4.5	5.75	5.125	0.922539039362139	0.0647661340586272
21	5.75	7	6.375	1.33607082066479	0.0937978103808225
22	7	8	7.5	3.90620838076474	0.274232314140835
23	8	9.25	8.625	5.15217120455388	0.361704162848059
24	9.25	11.75	10.5	6.30330994210374	0.0111037639527127
25	11.75	13.75	12.75	9.10367376302240	0.0160368196226390
26	13.75	16.75	15.25	19.4380266763352	0.0342415749666474
27	16.75	18.75	17.75	51.8127670319506	0.0912721633782872
28	18.75	22.5	20.625	90.3777167338643	0.159207280367849
29	22.5	27.5	25	141.003354216351	0.248388223987056
30	27.5	31	29.25	249.634417111708	0.439750173724808

Table A.2. NMMB/BSC Dust model weighting factors $w_{2.5,i}$, $w_{10,i}$, $w_{20,i}$ for particle size bin extension to 30 size channels

weighting factor	channel i	value
$w_{2.5}$	1	0.117404888
	2	0.085605622
	3	0.064541556
	4	0.052403848
	5	0.037331593
	6	0.033146401
	7	0.03682305
	8	0.034745817
	9	0.035881053
	10	0.040200676
	11	0.046778735
	12	0.064477276
	13	0.084061642
	14	0.119369998
	15	0.147227844
w_{10}	16	0.047316142
	17	0.047264056
	18	0.051626369
	19	0.059293012
	20	0.064766134
	21	0.09379781
	22	0.274232314
	23	0.361704163
w_{20}	24	0.011103764
	25	0.01603682
	26	0.034241575
	27	0.091272163
	28	0.15920728
	29	0.248388224
	30	0.439750174

Table A.3. CAMS model weighting factors $w_{dust1,i}$, $w_{dust2,i}$, $w_{dust3,i}$ for particle size bin extension to 30 size channels, aerosol particle type: dust

weighting factor	channel i	value
w_{dust1}	1	0.180806349
	2	0.131834715
	3	0.099395547
	4	0.080703185
	5	0.057491551
	6	0.051046254
	7	0.056708383
	8	0.053509393
	9	0.055257684
	10	0.061910008
	11	0.072040376
	12	0.072040376
w_{dust2}	13	0.413218133
	14	0.586781867
w_{dust3}	15	0.001018227
	16	0.001157024
	17	0.00115575
	18	0.001262422
	19	0.001449895
	20	0.001583729
	21	0.002293642
	22	0.006705816
	23	0.008844769
	24	0.010820937
	25	0.015628341
	26	0.033369398
	27	0.088947345
	28	0.155152068
	29	0.24206146
	30	0.428549177

Table A.4. CAMS model weighting factors $w_{salt1,i}$, $w_{salt2,i}$, $w_{salt3,i}$ for particle size bin extension to 30 size channels, aerosol particle type: sea salt

weighting factor	channel i	value
w_{salt1}	1	0.180806349
	2	0.131834715
	3	0.099395547
	4	0.080703185
	5	0.057491551
	6	0.051046254
	7	0.056708383
	8	0.053509393
	9	0.055257684
	10	0.061910008
	11	0.072040376
	12	0.072040376
w_{salt2}	13	0.015421299
	14	0.021898696
	15	0.027009281
	16	0.030690985
	17	0.030657201
	18	0.033486757
	19	0.038459623
	20	0.042009691
	21	0.060840701
	22	0.177877141
	23	0.234614591
	24	0.287034034
w_{salt3}	25	0.016216888
	26	0.034626055
	27	0.092297008
	28	0.16099493
	29	0.251177237
	30	0.444687883

Table A.5. CAMS model weighting factors $w_{total,i}$ for particle size bin extension to 30 size channels, aerosol particle types: organic matter, black carbon, sulphate

weighting factors	channel i	value
w_{total}	1	0.000807
	2	0.000589
	3	0.000444
	4	0.00036
	5	0.000257
	6	0.000228
	7	0.000253
	8	0.000239
	9	0.000247
	10	0.000276
	11	0.000322
	12	0.000443
	13	0.000578
	14	0.000821
	15	0.001012
	16	0.00115
	17	0.001149
	18	0.001255
	19	0.001441
	20	0.001574
	21	0.00228
	22	0.006666
	23	0.008793
	24	0.010757
	25	0.015537
	26	0.033174
	27	0.088426
	28	0.154242
	29	0.240642
	30	0.426037

A.6 PM weighting curves (source: [21])

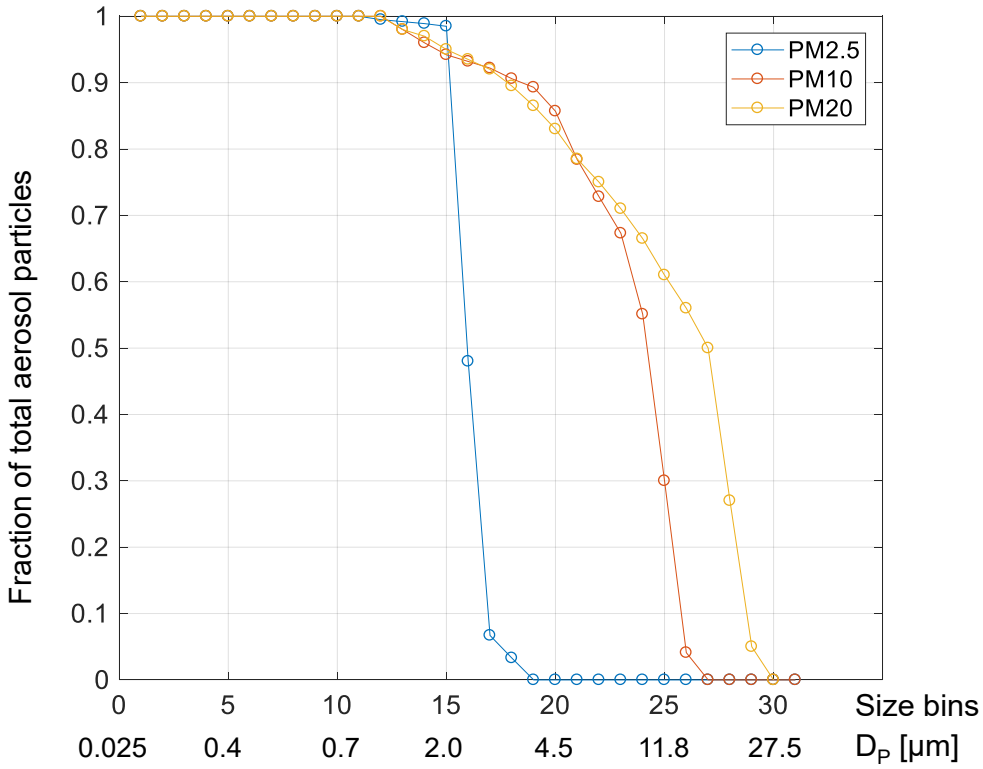

Appendix B

B.1 MAD and bias range for five-fold cross-validation with adapted DLR input data (see chapter 3.3) for PSA (left) and Missour (right) – different particle bin distributions

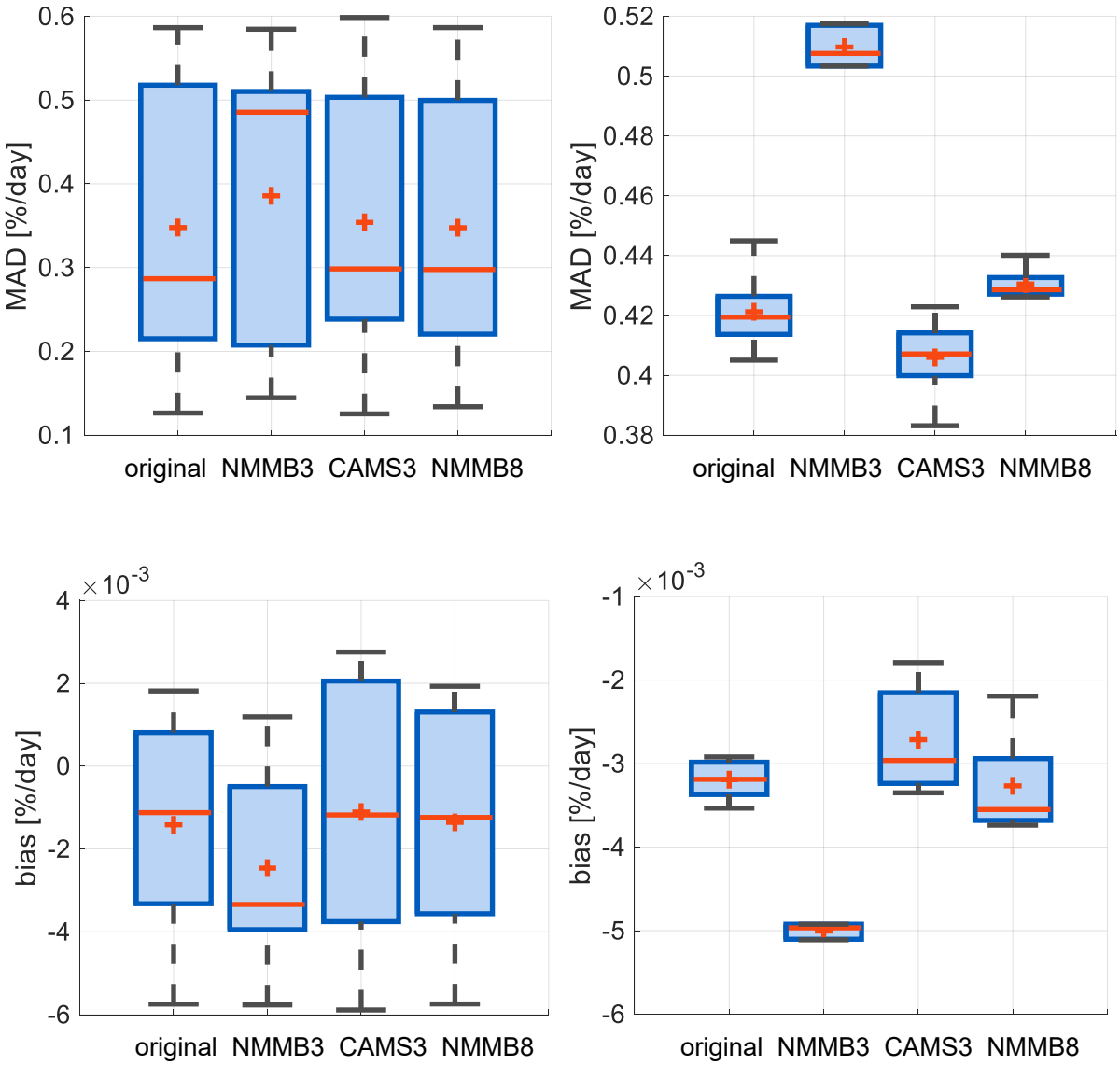

B.2 MAD and bias range for five-fold cross-validation with adapted DLR input data (see chapter 3.3) for PSA (left) and Missour (right) – different time resolution